DONATO DI VITO

MECHANICAL MODELING AND EXPERIMENTAL CHARACTERIZATION OF FILLED ELASTOMERS THROUGH GENERALIZED BIAXIAL TESTING

UNIVERSITÀ DEGLI STUDI DI NAPOLI 'FEDERICO II'

DEPARTMENT OF CHEMICAL, MATERIALS AND PRODUCTION ENGINEERING

PHD COURSE IN INDUSTRIAL PRODUCT AND PROCESS ENGINEERING

MECHANICAL MODELING AND EXPERIMENTAL CHARACTERIZATION OF FILLED ELASTOMERS THROUGH GENERALIZED BIAXIAL TESTING

SUPERVISOR
Prof. Massimiliano Fraldi

ADVISOR
Dr. Konrad Schneider

PHD COORDINATOR
Prof. Giuseppe Mensitieri

PHD CANDIDATE
Donato Di Vito

CYCLE XXIX

Donato Di Vito: *Mechanical modeling and experimental characterization of filled elastomers through generalized biaxial testing*,, PhD course in Industrial product and process engineering, Cycle XXIX.

ABSTRACT

Elastomer mechanical characterization and modeling are subjects that attract the scientific community since more than 50 years ago. However, despite the ample literature and the related scientific and industrial activity in this field, many different phenomena are not yet consolidated.

With this Thesis, then, the Author wants to try to fill in some of the gaps while trying to use a '*hybrid*' approach, for what concerns modeling and multi-axial characterization of filled elastomers by trying to use forefront techniques like Digital Image Correlation (DIC) —that allows to extrapolate local and quantitative information concerning surface deformation field of objects, hence also stress and strain concentration regions— together with mechanical testing machines able to perform non-standard biaxial tests, in static and dynamic loading conditions. With this purpose, a significant part of the research activities focused on the use and the partial redesign of some components of the BiaxTester, a planar biaxial testing device used to perform mechanical testing on polymeric materials. This machine, developed by Coesfeld Gmbh., is actually under testing phase at the Leibniz-Institut für Polymerforschung e.V. , Dresden (IPFDD, Germany). For this reason, the research activities have been partially performed at this research center, under the joint supervision of Prof. Massimiliano Fraldi of the University of Naples 'Federico II', Dr. Konrad Schneider of the Leibniz-Institut für Polymerforschung and of Bridgestone TCE (Rome).

The PhD Thesis is then divided in two different sections: the first is composed by a brief introduction on elastomers and on active reinforcing fillers, together with some background about mechanical properties of filled rubbers and about the evolution of modeling of this kind of materials. Afterwards, some remarks of

Continuum Mechanics in a nonlinear framework are included, with the purpose of underlining some of the aspects that will be encountered through the Thesis.

The second part of the Thesis is instead based on the different research activities developed during the PhD: in Chapter 2 there is a first introduction to biaxial testing and about the aforementioned BiaxTester, followed by a section regarding the sample and clamping system optimization and the comparison of the results obtained by using the optimized shape with some more conventional tests. In this section, the need to redesign the measurement process and control of the boundary conditions is shown to be fundamental in order to obtain reliable results in terms of stress-strain curves; the results obtained gave then the opportunity to choose the optimal configuration terms of homogeneity of deformations, with the aim of performing different types of tests on such materials. Successively, a novel approach to characterize mechanical behavior of elastomers through by imposing a planar biaxial loading state that follows certain paths of deformation, showing that different phenomena, such as relaxation and connected dissipative phenomena characteristic of the tires are not negligible in the case —as in this one— of loads in complex combinations. With this objective, it is shown how, by imposing displacements of the different clamps in two orthogonal directions (the two directions in which it is possible to impose deformations on these samples) different resulting forces will be registered, even in limit cases in which such complex loading combinations are reduced to equibiaxial loading. Moreover, it is shown how these phenomena are gradually more pronounced when increasing the reinforcement fraction and for bigger 'distances' of the biaxial path from the one imposed in the two orthogonal directions during the test.

Chapter 3 focuses instead on the description of the Mullins effect in filled rubbers: for this reason, some basic knowledge about pseudoelasticity theory is given, in order to then focus on a model able to describe different phenomena found in filled elastomers, such as stress softening, hysteresis and residual strain after loading application. This is done by following some other approaches found in literature, and by revising some parts of the Dorfmann-Ogden model, based on internal

variables which, together with the hyperelastic modeling, allows to describe the aforementioned phenomena.

On the basis of the previously obtained results, the last Chapter of the Thesis is focused on the crack propagation characterization in filled elastomers; this problem is of great interest for the scientific community, especially for what concern the elastomer behavior. This is due to the crucial importance of generalizing the concepts of stress intensification and of crack growth in complex loading conditions, with the objective of foresee and extend the fatigue life of filled elastomers undergoing cyclic solicitations also in case of complex geometries, such as car tires. Within this framework, the BiaxTester can be an interesting instrument thanks to its flexibility of applicable conditions; this will be shown in this work by comparing crack propagation data obtained through conventional testing setup and through the BiaxTester.

CONTENTS

LIST OF FIGURES

LIST OF TABLES

Part I

INTRODUCTION

In this Section, a brief introduction on elastomers and reinforcement is given, together with some background about mechanical properties of filled rubbers. After so, some remarks of Continuum Mechanics in a nonlinear framework are included.

1

INTRODUCTION ON ELASTOMERS AND CONTINUUM MECHANICS

1.1 A BRIEF INTRODUCTION ON FILLED ELASTOMERS

1.1.1 *Elastomers*

Elastomeric materials are widely used in various industrial fields, such as automotive, aerospace or even structural engineering, thanks to their peculiar properties. In fact, such materials are able to undergo large deformations and present a highly non linear stress-strain response, because of their structure. Elastomers are constituted of long polymeric chains, cross-linked together in different points in order to constitute a *polymeric network*. This kind of structure allows the material to be elastically stretched to a high degree of deformation without breaking.
Natural rubber, one of the most famous elastomers used today, is harvested from the *Hévéa Brasilien* tree, and its properties were known also by Aztecs and Maya. It has a milky color and was generally used as an adhesive, thanks to its stickiness. However, many synthetic elastomers are used nowadays, like Styrene Butadiene Rubber (SBR), Nitrile Butadiene Rubber (NBR) or Ethylene Propylene Diene Monomer (EPDM), as well as Butadiene Rubber (BR). Moreover, the different polymers can be used together to obtain particular properties of the final product, such as better mechanical properties, more stickiness or a better resistance to abrasion.
In order to form a polymeric network, polymer hans need to react and create physi-

cal and chemical entanglements. This is done through the addition of sulfur, which completely changes the properties of such polymeric chains. The process, called *vulcanization* was discovered by Charles Goodyear in 1839 [112].
As will be explained in the next section, elastomers are generally filled with reinforcing material, because of their poor mechanical properties; the use of Carbon Black and Silica is in fact quite common in order to attain material properties more suited for their particular framework of application.

1.1.2 *The filler contribution on reinforcement of elastomers*

In order to reduce costs and enhance processing efficiency of such materials, rubbers are generally filled with different classes of aggregates. These fillers play also a significant role in enhancing the mechanical properties of such materials, giving final products with properties that are higher also by one or two orders of magnitude.
Carbon black and amorphous silica are the most used fillers in tire industry, and are generally used as a fine powder with a mean particle size of about 10-100 nm (in particular, fillers with high surface area to volume ratio are preferred because of the higher degree of interaction with the polymer chains). In particular, these two fillers are able to enhance the mechanical properties of rubber through interaction with the polymeric network of the elastomer, and for this reason are classified as *active* fillers.
The structure of such reinforcing fillers has been extensively studied through the years, thanks to microscopy techniques such as high-resolution electron microscopy. In particular, fillers known as carbon black are made up of complex arrangements of spherical entities whose diameter ranges from 10 to 90 nm, as depicted in Figure 1. The elementary black particles, known as *colloidal black*, are morphologically similar to spheres made up of broken quasi-graphitic layers, whose stacking generate a rough surface (as can be seen in the works of Donnet et al. [25],[26]), that further enhance the filler-rubber interactions. The resultant three-dimensional objects are referred as *structures* or *aggregates*. These struc-

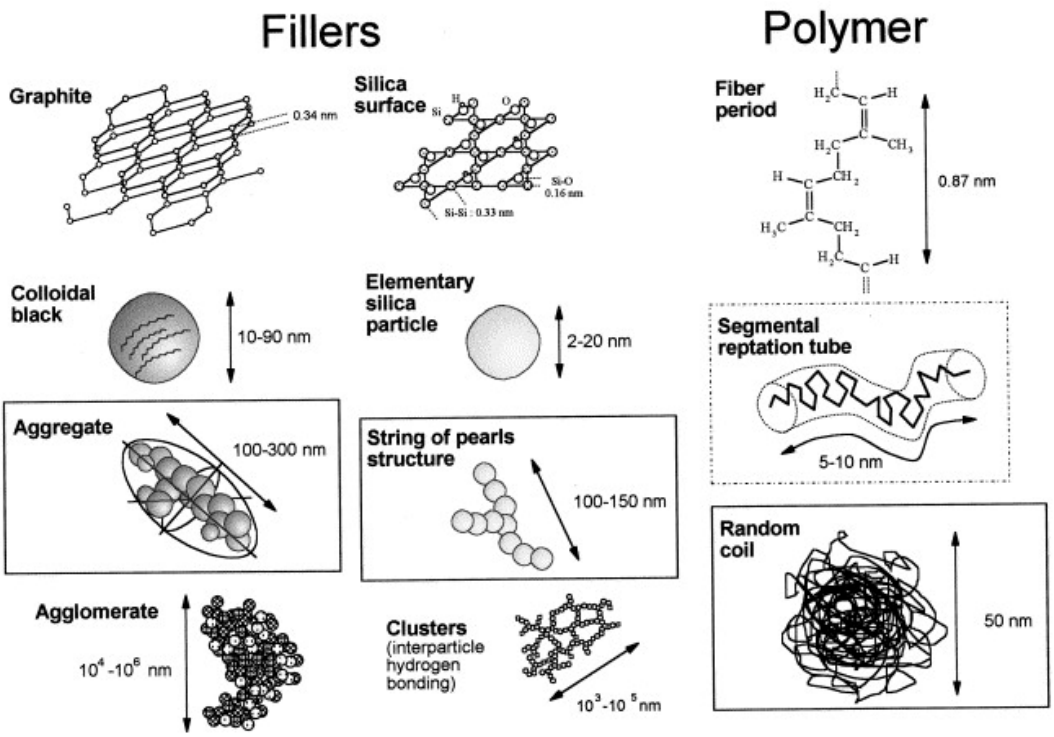

Figure 1: Hierarchical structure of reinforcing fillers for elastomers [71]

tures can be spheroidal, ellipsoidal, linear or branched depending on the process used for the production. Aggregates, moreover, generally assemble together to form bigger assemblies called *agglomerates*; during the process of preparing a compound, great attention is paid on the production of filled elastomers with the minimum amount possible of agglomerates, due to their function of failure initiation sites.

Amorphous silica structures generally exhibit a similar complex geometry, although with some differences on the agglomerates. In fact, the basic constituents of silica aggregates are spherical particles (called *silica pearls*); however, silica aggregates tend to form clusters due to the hydrogen bonding that keeps together these kinds of particles. The links between silica elementary particles are constituted by chemical bonds and the aggregates have dimensions in the 50–500 nm range. As for carbon black, silica aggregates cannot be broken during mixing

but are likely to form agglomerates which in turn gives relatively loose clusters through hydrogen bonding because of the specific surface chemistry of silica.

The high specific surface area, plays an important role in the polymer-filler

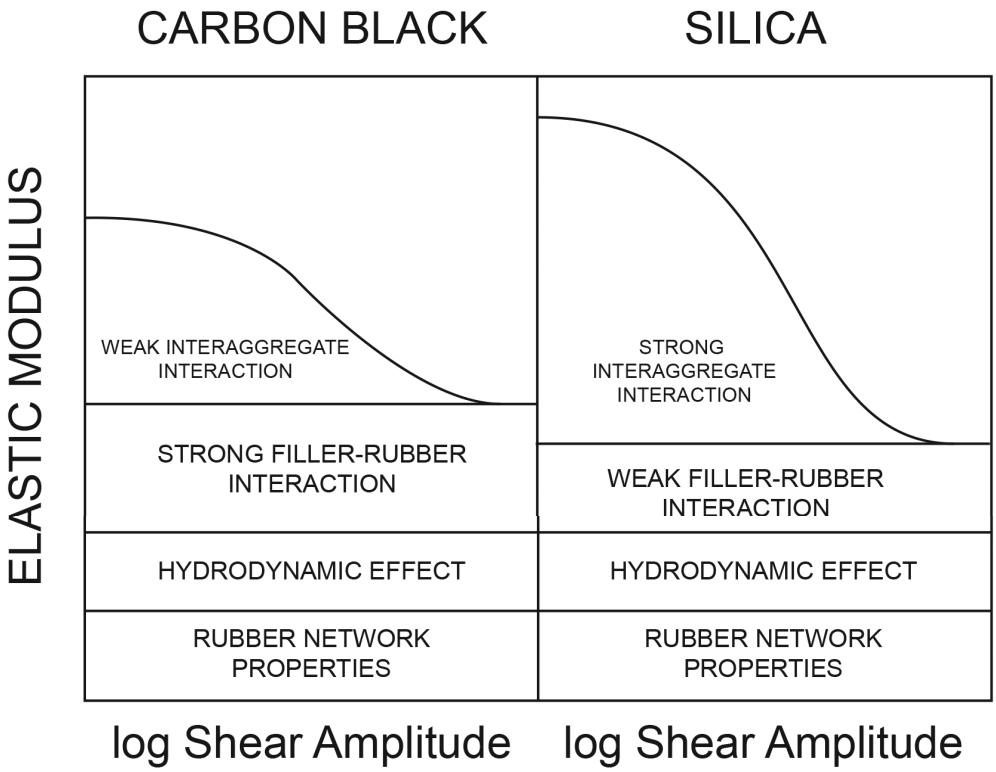

Figure 2: Payne concept of reinforcement and differences in interactions between carbon black and amorphous silica. While interaction between carbon black aggregates is lower, reinforcement of rubber with silica aggregates results in lower filler-rubber interactions [26].

interaction, which results in enhancement of the mechanical properties. Moreover, the aggregates themselves interact with each other through the polymer chains, creating substantially rigid regions in the elastomer network able to further enhance the properties of the compound. However, the two aforementioned processes of reinforcement are generally in contrast, meaning that higher filler-filler interactions normally lead to lower rubber-filler interactions, because of the different nature of the two molecules. For example, carbon black particles,

which are constituted by aggregates of graphite, lead to higher rubber-filler interactions because of the stronger affinity with the macromolecules constituting the rubber network, while amorphous silica, due to the presence its different structure, lead to a stronger inter-aggregate interaction, at the expenses of the interaction between the silica particles and the polymer chains. In the case of silica, this effect leads also to higher degree of difficulties in the processing of the mixture of rubber and filler, because the silica particles tend to cluster in higher particles, dramatically lowering the effective surface area and the the mechanical properties, together with the generation of defects which are generally common in poorly-mixed compounds. The entity of the different interactions in compounds filled with carbon black and silica are shown schematically in Figure 2.

1.1.3 *Mechanical properties of filled elastomers*

As specified before, the use of fillers in rubbers greatly enhance their mechanical properties. These particles, which at first glance can be assumed to be spherical, can be in fact considered as similar to rigid particles in some sort of fluid constituted by the elastomer network. Starting from the dilute estimate proposed by Einstein in 1906 [28], it is possible to consider that the viscosity increase in a Newtonian fluid where spherical particles have been dispersed is

$$\eta = \eta_0 \left(1 + 2.5\phi\right) \tag{1}$$

where η_0 and η are respectively the viscosity of the pure fluid and of the suspension. In the same way, as proposed by Guth and Gold [42], for very low volume fractions of filler and for small deformations, it is possible to consider that the increase in Young modulus (or many other properties, such as thermal conductivity

and dielectric constant) of a filled rubber can be related to the one of the same unfilled rubber by the formula

$$E = E_0 \left(1 + 2.5\phi\right) \tag{2}$$

which is based on the concept that, for low filler volume fractions, colloidal carbon black hardly assembles in bigger aggregates. The equation (2) is part of a broader theory, where a particular property p of a suspension can be related to the property of the main component p_0 and to a power series of the concentration of the fillers (in this case considered as spherical),

$$E = E_0 \left(1 + \sum_{i=1}^{N} \alpha_i \phi^i\right) \tag{3}$$

where N is an integer. For $N = 2$, and for the case of spherical fillers, the equation (3) becomes

$$E = E_0 \left(1 + 2.5\phi + 14.1\phi^2\right) \tag{4}$$

Equation (4) stays valid up to quite high values of filler concentration, and as reported in [42] can be used in order to predict the increase in mechanical properties of filled rubber up to $\phi = 0.15$; however, higher filler concentrations (up to $\phi = 0.3$) it must be considered that colloidal carbon black can combine in carbon black chains and agglomerates. In this case, the increment in stiffness of the filled rubber is much faster, and by considering that the elementary fillers of the aforementioned suspension are *rod-like filler particles*, equation (3) can be specialized with different parameters and, in general, a slightly different form:

$$E = E_0 \left(1 + 0.67 f\phi + 1.62 f^2\phi^2\right), \qquad f = \frac{l}{\langle w \rangle} \tag{5}$$

where f is the shape factor of the aggregates (equal to the major length over the mean width), assuming that $f \gg 1$.

Although very simple, the approach adopted from Guth and Gold has been shown

to be enough accurate, at least in first approximation; one clear example has been reported in one of the works published by Guth [42] and represented in Figure 3, where for convenience $E_{sp} = E/E_0$ is shown. Many phenomena are not taken into account in this kind of model; for example, two important aspects such as surface energy of the fillers and void volume created by the aggregates are not included. These types of particles, in fact, can also aggregate into irregular structures that are characterized by a large amount of void volume (within the pervaded space), in which rubber macromolecules can be *occluded*, increasing then the effective volume fraction of rigid particles, which can cause a deviation from the previously described laws.

However, other than increasing the elastic mechanical properties and improving

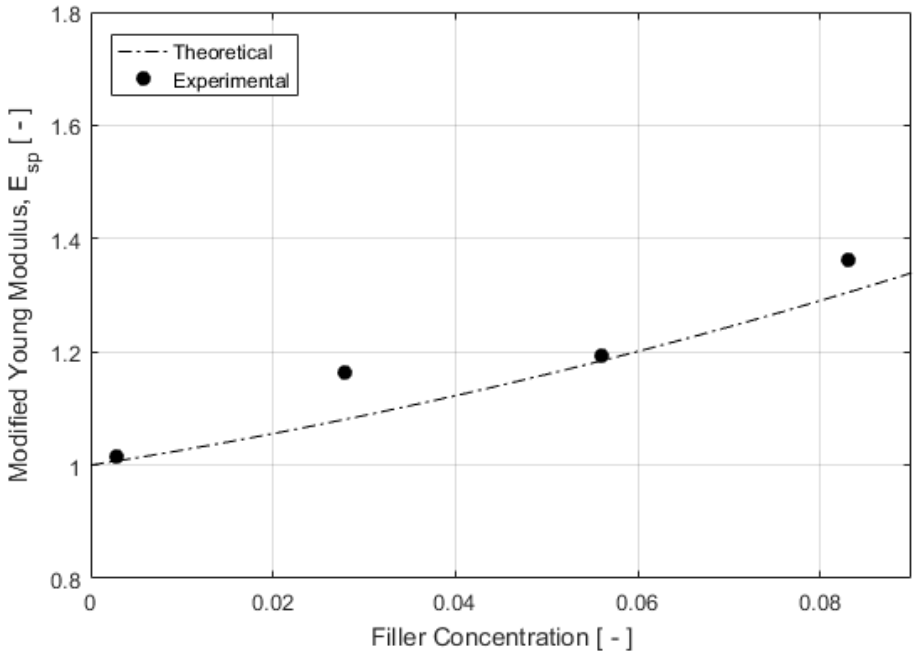

Figure 3: Theoretical outcomes of the Guth and Gold model prediction vs. experimental results for a styrene-butadiene rubber filled with carbon black, as seen in [42]. The deviation from the theoretical curve of the fourth circle is on the upper side of the curve, because of the different reinforcement mechanism (at that volume fraction, the colloidal carbon black starts to combine in carbon black chains).

processability of the rubbers, fillers have also many other kinds of peculiar effects, mainly concerning inelastic behavior, thus altering the mechanical behavior of rubbers in many ways. Two effects are directly related to the presence and the amount of fillers, namely the Payne and the Mullins effects. The former, also known as Fletcher-Gent effect, has been discovered by Fletcher and Gent in 1954 [30] and further studied by Payne [96], and mostly regards rubber dynamic behavior. In fact, when filled rubber is cyclically strained, the recorded modulus falls as the amplitude of strain increases, as can be seen in Figure 4, where it can be seen also that, for sufficiently high cyclic strain amplitude, the Young modulus falls at the level of unfilled rubber for any amount of filler; moreover, it was found that mechanical property enhancement and fall of the Young modulus are both exponentially increased by increasing filler loading, as seen in the work from Payne and Whittaker [97]. Also, although partial recovery occurs almost immediately on returning to small deformation amplitudes, complete recovery takes months, unless the sample is heated to accelerate the recovery.
In first analysis, Payne effect has been connected to the carbon black network breakage, as can be seen also in Figure 2, where there are also the different contributions to mechanical properties have been listed in the case of silica and carbon black reinforcement [96].
The second phenomenon anticipated before, known as Mullins effect or stress softening, concern instead rubber mechanical behavior in quasi-static loading; it was discovered by Bouasse and Carrière [13] in 1903 and successively studied by Mullins [83] [84]. As shown in Figure 5, in fact, it is possible to see a change (a reduction) of the mechanical properties upon cyclic loading up to the same strain value. Many different considerations can be made about this phenomenon:

- Most of the softening, seen as a lower resulting stress for the same applied strain, appears after the first load;
- Softening generally affects mechanical behavior for stretches lower or equal to the maximum stretch applied;

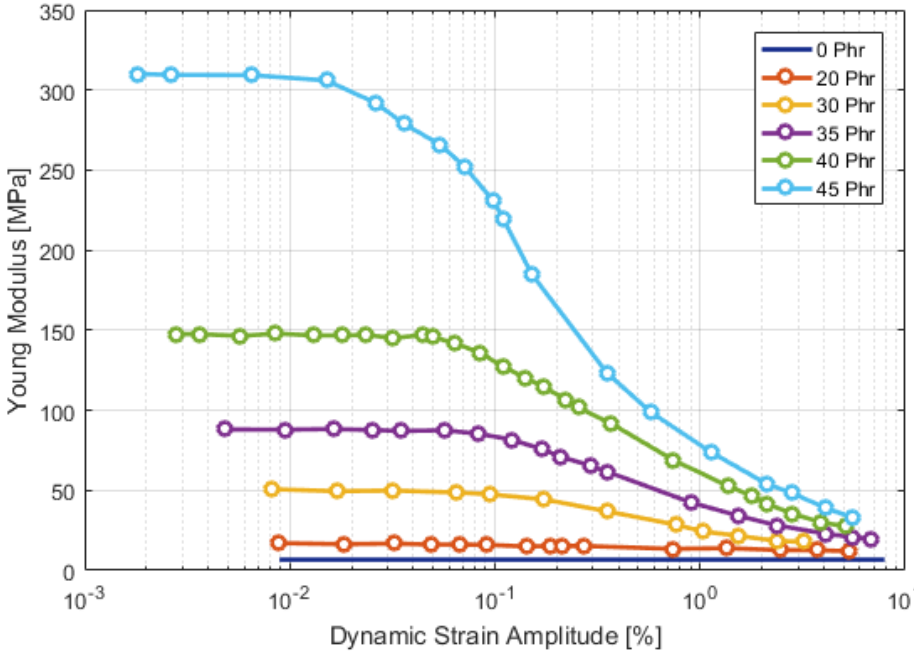

Figure 4: Experimental results performed by Payne [96].

- Softening increases progressively with the increasing maximum stretch;
- After a few cycles (generally in a number between 5 and 20, depending on rubber and filler used), the material response can be considered stable, aside from a fatigue effect;
- When the stretch exceeds the maximum previously applied stretch, the material stress–strain response returns almost at the same level as on the virgin stress-strain behavior, after some transition around the point of maximum stretch applied previously.

Some more aspects connected to the Mullins effect can be also observed in Figure 5, such as:

- *Residual strain* — this is not necessarily connected to the Mullins effect, but upon loading, unloading and reloading it can be noticed that there is a certain

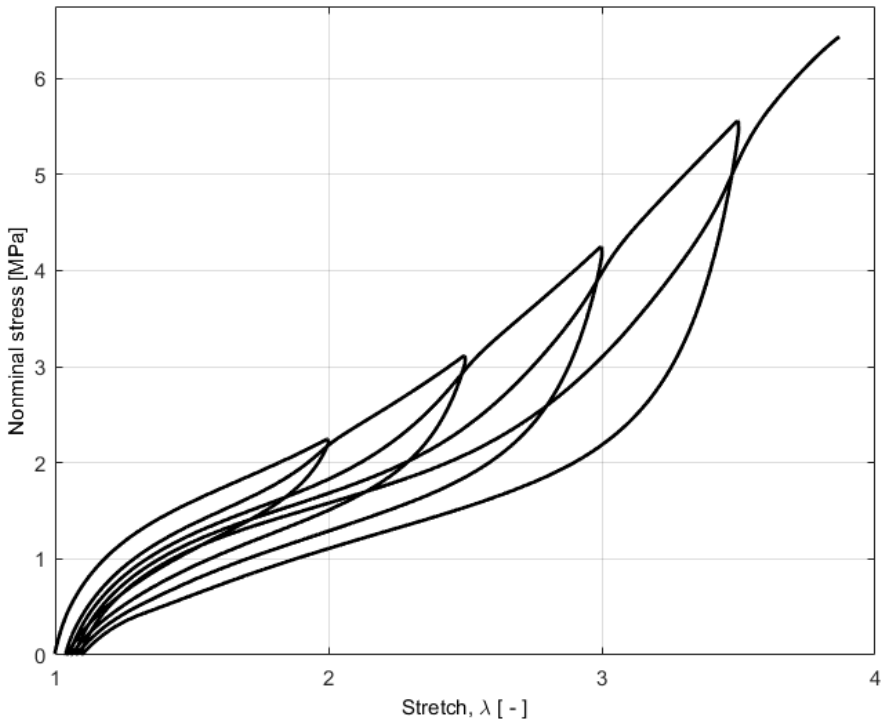

Figure 5: Experimental results for a loading-unloading test with increasing maximum strain on Natural Rubber (NR) with 50 phr of Carbon Black (CB).

amount of permanent set of the sample. Moreover, it seems that this permanent set depends on the maximum strain reached, and not on the amount of cycles, if the amount of permanent set generated by sample fatigue is not taken into account;

- *Hysteresis* — upon loading-unloading cycles, there seems to be a rate-independent hysteresis, which seems to not depend upon anything but positive or negative deformation rate.

These two effects can be further noticed also in Figure 6, where the results from cyclic tests at slow speed are shown: four different samples have been subjected to loading-unloading cycles with transverse speeds of 50, 30, 15 and 7.5 mm/min,

each for 25 cycles. The results show basically no dependence of the strain rate on the hysteresis and residual strain.

Several attempts have been made in order to correctly describe and model

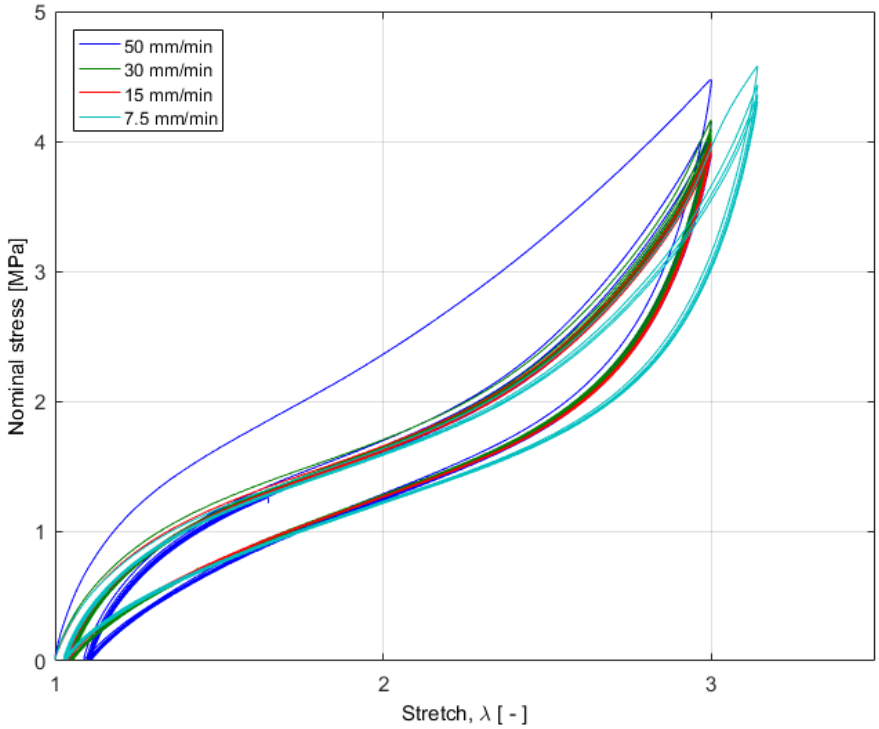

Figure 6: Experimental results for loading-unloading tests with different transverse speeds on Natural Rubber (NR) with 50 phr of Carbon Black (CB). It can be noted that, although on the sample tested at 50mm/min the residual strain is slightly higher, there is a high level of correspondence between the hysteresis cycles and residual strains of the samples tested at different speeds. Moreover, the last test (7.5 mm/min) is conducted to a slightly higher displacement in order to highlight the constancy of the hysteresis cycle also for slightly different maximum displacement.

the mechanical behavior of filled rubber, both through phenomenological and physically justified models, especially in the last two decades. For example, the works from Lion [72] and from Bergström and Boyce [9] have been pioneering works on the subject, by introducing a damage variable able to adequately

describe the softening, while the works from Ogden and different collaborators [70] [92] [27] introduced and developed such models in the framework of Pseudoelasticity. Lastly, the work from zz et al. [73] seems promising also in terms of the introduction of physically valid variables able to correctly describe such behavior. However, this aspect will be further investigated in Chapter 3.

1.2 REMARKS ON CONTINUUM MECHANICS

Elastomeric materials are characterized by a complex behavior, especially regarding their response to external mechanical solicitations. For this reason, they are generally included in the so-called *nonlinear elastic materials*. Mechanical modeling and experimental testing of such materials should be always accompanied by specific notions regarding the nonlinear framework of Continuum mechanics, due to the importance of this framework in all the aspects of the experimental investigations concerning elastomers.
This section tries to give some remarks about the Continuum Mechanics framework, but it is by no means an exhaustive dissertation on the topic. For further information and reading material concerning the topics covered, the works from Cowin and Doty [22], Holzapfel [50], Ogden[91] and Ogden and Fu [99] the are warmly suggested.

1.2.1 *Motion and Deformation of Continua*

Let us consider a continuum body $\mathcal{B}$, defined as a contiguous set of material points, called particles. The body $\mathcal{B}$ is considered to be embedded in a reference frame $\mathbb{R}$, consisting of an origin O and of an orthogonal vector basis, $\mathbf{e}_i = \{\mathbf{e}_1, \mathbf{e}_2, \mathbf{e}_3\}$. The position of a body particle P with respect to $\mathbb{R}$ at a reference time t_0 is defined by its position vector $\mathbf{X}(P)$; its motion vector is then the locus of points determined

by the change of the aforementioned position vector, $\mathbf{x}(\mathbf{X}, t)$. The regions occupied by the body at a certain time t, denoted by Ω_t, are called *configurations*. The configuration of a deformable body, as the one taken into account, evolves over time, and is determined uniquely at any time. It is then conventional to set a timeline, together with a starting time, $t_i = 0$, which is then denoted as initial time. The configuration Ω_{t_i} is consequently called *initial conigurations*, while the *reference configuration* is consequently defined as Ω_{t_0} (however, it is general practice to let the initial and reference configurations coincide; this proposition holds also in this work); in the same way it is possible to define further configurations, such as the *current* or *deformed configuration* at the time $t > 0$. In general, for a certain time t_k the region Ω_{t_k} defined the domain of the position vector $\mathbf{x} = \mathbf{x}(\mathbf{X}, t_k)$, for every material point of the body $\mathcal{B}$.

It is also possible, through the the position vectors at different times, to define a one-to-one correspondence between the particle $P \in \mathcal{B}$ and the position $\mathbf{X} \in \Omega_{t_0}$, namely $\mathbf{X} = \kappa_0(P, t)$; a similar correspondence can be found between the particle $P \in \mathcal{B}$ and and the position $\mathbf{x} \in \Omega_t$, which is $\mathbf{x} = \kappa(P, t)$. Consequently, it is possible to define an invertible correspondence between the material point $\mathbf{X} \in \Omega_{t_0}$ and $\mathbf{x} \in \Omega_t$ as

$$\begin{aligned} \mathbf{x} &= \chi(\mathbf{X}, t) \\ \mathbf{X} &= \chi^{-1}(\mathbf{x}, t) \end{aligned} \tag{6}$$

It is evident how motion can be expressed in different ways: on one side it is in fact possible to characterize motion with respect to the material coordinates, together with the time t, in order to describe the evolution of the particle position as it moves (the observer moves solidarily with the body particle), using a *Lagrangian* (or *material*) approach. When instead choosing to characterize motion with respect to the spatial coordinates (thus, by fixing the observer on a region point), the approach is called *Eulerian* or *spatial*.

The change of relative distance between different points of a body $\mathcal{B}$ is directly connected to deformation itself; for this reason, motion of the different particles in a body $\mathcal{B}$ can be directly connected to deformation. By considering coincidence between the reference and the current configuration, it is possible to introduce a

displacement field, which creates a link between the body particles position in its reference configuration $\mathbf{X}$ and the body particle position in the current (deformed) configuration, $\mathbf{x}$.

$$\mathbf{x} = \mathbf{X} + \mathbf{u}\left(\mathbf{X}, t\right) \tag{7}$$

The displacement field defined in equation 7 can be decomposed into a sum of a translational, rotational, and deformational motion. In order to focus on the behavior of *deformable* bodies, it is necessary to consider a mathematical entity able to exclude the first two aliquots connected to motion. The translational component of motion can be excluded by considering the deformation gradient, $\mathbf{F}$, defined as

$$\mathbf{F} = \left[\nabla_{\mathbf{X}} \otimes \chi\left(\mathbf{X}, t\right)\right]^{\mathsf{T}} \forall \mathbf{X} \in \Omega_{t_0} \tag{8}$$

Here, the symbol ∇ indicates the gradient operator, while its subscript indicates that it is applied through the material coordinate system. The operator $\otimes$ is the standard tensor product between two vectors, defined as $\left[\mathbf{a} \otimes \mathbf{b}\right] = a_i b_j$. The spatial inverse deformation gradient tensor is is defined as

$$\mathbf{F}^{-1} = \left[\nabla \otimes \chi^{-1}\left(\mathbf{x}, t\right)\right]^{\mathsf{T}} \mathbf{x} \in \Omega_t \tag{9}$$

where no subscript under the *nabla* operator indicates that the gradient is applied with respect to the current configuration. The definitions of the deformation gradient $\mathbf{F}$ and of its inverse $\mathbf{F}^{-1}$ come directly from differentiation of equations in 6, with respect to the material and the spatial coordinate system. However, by defining the deformation gradient through equation 7, a different (but obviously equivalent) definition of $\mathbf{F}$ can be highlighted:

$$\mathbf{F} = \mathbf{I} + \mathbf{u}\left(\mathbf{X}, t\right) \otimes \nabla_{\mathbf{X}} \tag{10}$$

The deformation gradient is a crucial quantity in continuum mechanics, and contemporaneously is the first definable measure of deformation. It represents a linear operator which generates a vector $\mathrm{d}\,\mathbf{x}$ from the vector $\mathrm{d}\,\mathbf{X}$.

Its elements are called *stretches*, and represent the relative change in length between a spatial and a material line element.
The determinant of the deformation gradient tensor, indicated as J, is the Jacobian of the transformation from $\mathbf{x}$ to $\mathbf{X}$, and thus defines the change in volume of the body upon deformation

$$J \equiv Det\mathbf{F} \tag{11}$$

In order to maintain the finiteness of the considered body during deformation, it is necessary that J assumes a finite value for every admissible deformation, which means $0 < J < \infty$. In fact the relation in equation 11 can be rewritten as $dv = J\,dV$, where no one of the two infinitesimal volumes can vanish.
When $J > 1$ or $J < 1$, the considered body element is respectively subjected to volumetric expansion or contraction, while when $J = 1$ the body undergoes an isochoric deformation.
It is now worth to observe that generic infinitesimal area element $\mathrm{d}\,\mathbf{a} = \mathrm{d}\,a\mathbf{n}$, defined through a surface $\mathrm{d}\,a$ and its normal unit vector $\mathbf{n}$, may be obtained by the cross product of two line elements. By employing this concept, an infinitesimal volume can be written as $\mathrm{d}\,v = \mathrm{d}\,\mathbf{a} \cdot \mathrm{d}\,\mathbf{x}$, and in the same way, $\mathrm{d}\,V = \mathrm{d}\,\mathbf{A} \cdot \mathrm{d}\,\mathbf{X}$. At this point, by using the Jacobian defined in equation 11, together with the deformation gradient $\mathbf{F}$, it is possible to write

$$\mathrm{d}\,v = \mathrm{d}\,\mathbf{a} \cdot \mathrm{d}\,\mathbf{x} = J\,\mathrm{d}\,V \Rightarrow \tag{12}$$

$$\Rightarrow \mathrm{d}\,\mathbf{a} \cdot \mathbf{F}\,\mathrm{d}\,\mathbf{X} = J\,\mathrm{d}\,\mathbf{A} \cdot \mathrm{d}\,\mathbf{X} \Rightarrow \tag{13}$$

$$\left[\mathrm{d}\,\mathbf{a} - J\mathbf{F}^{-\mathsf{T}}\,\mathrm{d}\,\mathbf{A}\right] \cdot \mathrm{d}\,\mathbf{X} = 0 \tag{14}$$

and, since $\mathrm{d}\,\mathbf{X}$ cannot vanish, the part in square parentheses must be equal to zero. The relation

$$\mathrm{d}\,\mathbf{a} = J\mathbf{F}^{-\mathsf{T}}\,\mathrm{d}\,\mathbf{A} \tag{15}$$

is also known as *Nanson formula*, and maps an infinitesimal material area $\mathrm{d}\,\mathbf{A}$ into a spatial area $\mathrm{d}\,\mathbf{a}$.
As introduced before, the deformation gradient allows to exclude the translational

rigid motions of an object. However, it can be further decomposed into two tensors, one related to pure rotation and another to pure deformation. This decomposition, defined as *polar decomposition*, can be written as

$$\mathbf{F} = \mathbf{R}\mathbf{U} = \mathbf{V}\mathbf{R} \tag{16}$$

Here, $\mathbf{R} \in Orth^{+}$ is a unique rotation tensor (with the property that $\mathbf{R}^{\intercal}\mathbf{R} = \mathbf{R}\mathbf{R}^{\intercal} = \mathbf{I}$), while $\mathbf{U}$ is the right stretch tensr and $\mathbf{V}$ is the left stretch tensor. The two stretch tensors, both positive definite and symmetric (i.e. $\mathbf{U} = \mathbf{U}^{\intercal}$ and $\mathbf{V} = \mathbf{V}^{\intercal}$) and represent a pure deformation. Moreover, they can be diagonalized, and their spectral decomposition is given by

$$\mathbf{U} = \lambda_1 \mathbf{N}_1 \otimes \mathbf{N}_1 + \lambda_2 \mathbf{N}_2 \otimes \mathbf{N}_2 + \lambda_3 \mathbf{N}_3 \otimes \mathbf{N}_3 \tag{17}$$

$$\mathbf{V} = \lambda_1 \mathbf{n}_1 \otimes \mathbf{n}_1 + \lambda_2 \mathbf{n}_2 \otimes \mathbf{n}_2 + \lambda_3 \mathbf{n}_3 \otimes \mathbf{n}_3 \tag{18}$$

where λ_1, λ_2 and λ_3 are the eigenvalues of $\mathbf{U}$ and $\mathbf{V}$, also called principal stretches, while $\mathbf{N}_k$ and $\mathbf{n}_k$ are the correspondent eigenvectors in material and current configuration. Comparison of equations 17 and 16 shows also that $\mathbf{n}_i = \mathbf{R}\mathbf{N}_i$, due to the uniqueness of the spectral decomposition. As seen also through the polar decomposition of $\mathbf{F}$, the deformation gradient tensor, although containing all the useful information needed to describe the deformation behavior of a body, is not a suitable deformation measure due to the presence of rotation. For this reason it is necessary to define other measures, based only on its purely deformation part, as the *left* and *right Cauchy-Green tensors*, respectively $\mathbf{C}$ and $\mathbf{b}$. These two tensors are defined as

$$\mathbf{C} = \mathbf{F}^{\intercal}\mathbf{F} = \mathbf{U}^{\intercal}\mathbf{R}^{\intercal}\mathbf{R}\mathbf{U} = \mathbf{U}^2 \tag{19}$$

$$\mathbf{b} = \mathbf{F}\mathbf{F}^{\intercal} = \mathbf{V}\mathbf{R}\mathbf{R}^{\intercal}\mathbf{V}^{\intercal} = \mathbf{V}^2 \tag{20}$$

$\mathbf{C}$ and $\mathbf{b}$ are respectively a Lagrangian and an Eulerian strain tensor. Moreover, thanks to their definition, they do not take into account for rigid body rotations. However, these two tensors are not the only adoptable deformation measures.

Through the years, in fact, several deformation measures have been adopted by various authors, such as the *Green-Lagrange strain tensor* or the *Euler-Almansi strain tensor*, respectively defined as

$$\mathbf{E} = \frac{1}{2}\left(\mathbf{C} - \mathbf{I}\right) \tag{21}$$

$$\mathbf{e} = \frac{1}{2}\left(\mathbf{I} - \mathbf{b}^{-1}\right) \tag{22}$$

These two deformation tensors derive from the same concept applied through different descriptions. In fact, by considering deformation of a length $\mathrm{d}\,\mathbf{X}$ into a length $\mathrm{d}\,\mathbf{x}$, it is possible to calculate the change as $\mathrm{d}\,\mathbf{x}^2 - \mathrm{d}\,\mathbf{X}^2$. In Lagrangian description, it is possible to write

$$\mathrm{d}\,\mathbf{x}^2 = \mathbf{F}\cdot\mathrm{d}\,\mathbf{X}\cdot\mathbf{F}\cdot\mathrm{d}\,\mathbf{X} = \mathrm{d}\,\mathbf{X}\cdot\mathbf{F}^{\intercal}\mathbf{F}\cdot\mathrm{d}\,\mathbf{X} \tag{23}$$

Then, the change defined before can be written as

$$\mathrm{d}\,\mathbf{x}^2 - \mathrm{d}\,\mathbf{X}^2 = \mathrm{d}\,\mathbf{X}\cdot\left(\mathbf{C} - \mathbf{I}\right)\cdot\mathrm{d}\,\mathbf{X} \tag{24}$$

where the quantity in the parentheses is equal to twice the Green-Lagrange strain tensor. In Eulerian description, it is instead possible to write

$$\mathrm{d}\,\mathbf{X}^2 = \mathbf{F}^{-1}\cdot\mathrm{d}\,\mathbf{X}\cdot\mathbf{F}^{-1}\cdot\mathrm{d}\,\mathbf{X} = \mathrm{d}\,\mathbf{X}\cdot\mathbf{F}^{-\intercal}\mathbf{F}^{-1}\cdot\mathrm{d}\,\mathbf{X} \tag{25}$$

Consequently, it is possible to write the change in length as

$$\mathrm{d}\,\mathbf{x}^2 - \mathrm{d}\,\mathbf{X}^2 = \mathrm{d}\,\mathbf{x}\cdot\left(\mathbf{I} - \mathbf{b}^{-1}\right)\cdot\mathrm{d}\,\mathbf{x} \tag{26}$$

where the quantity between the parentheses is this time equal to twice the Euler-Almansi strain tensor.

In 1961, B.R. Seth was the first to show that the previously cited strain measure are

specialized forms of a more general strain measure. In 1968, R. Hill [47] showed that the aforementioned more general strain measure family could be defined as

$$\mathbf{E}_m = \begin{cases} \frac{1}{2m}\left(\mathbf{U}^{2m} - \mathbf{I}\right) & m \neq 0 \\ \ln \mathbf{U} & m = 0 \end{cases} \tag{27}$$

This relation is valid for every real m; for example, $m = 1$ gives the Green-Lagrange strain tensor, as defined in equation 21_1, while $m = -1$ gives the Euler-Almansi strain tensor defined in equation 21_2. Other notable strain measures are, for example, the one obtained for $m = 1/2$, which is generally referred to as engineering strain. For $m = 0$, instead, we have the *Hencky strain*, also known as *logarithmic strain tensor*, which is defined through the logarithm of the eigenvalues of $\mathbf{U}$ and $\mathbf{V}$ as

$$\mathbf{H} = \ln \mathbf{U} = \ln \lambda_i \mathbf{N}_i \otimes \mathbf{N}_i \tag{28}$$

$$\mathbf{h} = \ln \mathbf{V} = \ln \lambda_i \mathbf{n}_i \otimes \mathbf{n}_i \tag{29}$$

It is worth to notice that the logarithm of a tensor exists only if the tensor itself is diagonal; for this reason, the Hencky strain tensors (in Eulerian and Lagrangian reference system) are defined only through the principal reference system (i.e. the three directions identified through the spectral decomposition of the respective tensors). One of the major advantages arising from the use of this particular strain measure derives directly from the logarithm properties, and is based on the additive decomposition of the applied deformation history. In fact, by considering a deformation of a fiber, say λ, as the result of the combination of two stretches (in this case $\lambda_1 = l/l_1$ and $\lambda_0 = l_1/l_0$, where l_1 can be considered as an intermediate length of the fiber in its change of length from l_0 to l), it is possible to write that $\lambda = \lambda_0 \lambda_1$ while the correspondent Hencky (true strain) is defined as

$$\epsilon = \ln \frac{l}{l_0} = \ln \frac{l}{l_1}\frac{l_1}{l_0} = \ln \lambda_1 + \ln \lambda_0 \tag{30}$$

This property becomes very useful when there re different effects applied on the considered body (e.g. thermal and mechanical stimuli applied), and becomes fundamental in biomechanical modeling, where the presence of different deformation stimuli and constraints is not a rare event.

1.2.2 *Stress Measures*

Upon deformation, different kinds of interactions among neighboring parts of a body arise. A way to express such interactions is to introduce the concept of stress, which, for a deformable body, is the resulting field of internal reactive forces acting between infinitesimal surfaces within the body.
By focusing the attention on a deformable body $\mathcal{B}$ which occupies an arbitrary region Ω_t with a boundary $\partial\Omega_t$ at a time t, it is at first necessary to define *external forces* as forces acting on parts of the boundary, and as *internal forces* the ones within the interior part of the domain, in a distributed way (such as gravity).
Now, let the body (to which are applied a set of external and internal forces $\mathbf{f}$) be cut by a plane passing through a given point $\mathbf{x} \in \Omega_t$; this plane, which can be indicated as π, cuts the body in two parts. By considering interaction of the two portions, it is possible to realize that forces are transmitted across the plane surface.
The infinitesimal resultant force acting on a surface element of area $\mathrm{d}\,a$ will then be $\mathrm{d}\,f$ so that, in the point P the Cauchy surface traction can be defined as

$$\mathbf{t}(\mathbf{x}, t) = \frac{\mathrm{d}\,f}{\mathrm{d}\,a} \tag{31}$$

The traction vector in equation 31 persists on all surfaces passing through the point P that have the same normal vector $\mathbf{n}$. It is possible at this point to recall

the Cauchy stress theorem, which asserts that there exist a second-order tensor $\boldsymbol{\sigma}(\mathbf{x}, t)$ so that the traction vector $\mathbf{t}$ is a linear function of $\mathbf{n}$, so that

$$\mathbf{t}(\mathbf{x}, t, \mathbf{n}) = \boldsymbol{\sigma}(\mathbf{x}, t)\mathbf{n} \tag{32}$$

Through equilibrium of the angular momentum it also is possible to show also that the second-order tensor $\boldsymbol{\sigma}(\mathbf{x}, t)$, generally called *Cauchy stress tensor*, is symmetric. It is defined through the Eulerian description, and can be represented as

$$\boldsymbol{\sigma}(\mathbf{x}, t) = \sigma_{ij}\mathbf{n}_i \otimes \mathbf{n}_j \tag{33}$$

By multiplying the Cauchy stress tensor by the Jacobian J it is possible to obtain the *Kirchhoff stress tensor*, $\boldsymbol{\tau}$

$$\boldsymbol{\tau} = J\boldsymbol{\sigma} \tag{34}$$

Instead, by following the same treatise as for the Cauchy stress tensor through an Eulerian description, it is possible to obtain the first Piola-Kirchhoff stress tensor by doing so through a Lagrangian description

$$\mathbf{P} = P_{ij}\mathbf{n}_i \otimes \mathbf{N}_j \tag{35}$$

It is important to notice also that the first Piola-Kirchhoff stress tensor is not symmetric. The second Piola-Kirchhoff stress tensor, instead, is symmetric and defined as

$$\mathbf{S} = \mathbf{F}^{-1}\mathbf{P} \tag{36}$$

1.2.3 *Constitutive Equations for Hyperelastic Materials*

All the concepts introduced before are essential to characterize different aspects of kinematics and stress response, and hold for any continuum body. In order to specify how interaction in the material and its deformation behavior, it is necessary to specify, through appropriate constitutive laws, how is it possible to mathematically

approximate the real material response under specific loading condition.
For a Cauchy-elastic material (for which the stress field depends only on the state of temperature and deformation at the current time t) it is possible to define a constitutive equation as a law that relates the Cauchy stress tensor $\boldsymbol{\sigma}(\mathbf{x}, t)$ for each $x = \chi(\mathbf{X}, t)$ with the deformation gradient $\mathbf{F} = \mathbf{F}(\mathbf{X}, t)$. this concept can be mathematically expressed as

$$\boldsymbol{\sigma}(\mathbf{x}, t) = \mathfrak{g}\left(\mathbf{F}\left(\mathbf{X}, t\right), \mathbf{X}\right) \tag{37}$$

where $\mathfrak{g}$ can be considered as the constitutive equation associated with the Cauchy stress tensor $\boldsymbol{\sigma}$. The dependence with the position $\mathbf{X}$ of the constitutive equation $\mathfrak{g}$ is due to the fact that no restrictions have been applied on the material yet, and thus $\mathfrak{g}$ can be considered as a function varying with the position; materials that have this feature are generally called *heterogeneous*. Materials for which the Cauchy stress tensor and the density ρ_0 are independent from $\mathbf{X}$ are instead called *homogeneous*, and the next part of this section will be focused on them. For homogeneous materials, the relation in 37 can be written as

$$\boldsymbol{\sigma}(\mathbf{x}, t) = \mathfrak{g}\left(\mathbf{F}\right) \tag{38}$$

Mathematically, the constitutive law $\mathfrak{g}$ is a tensor-valued unction of one tensor variable $\mathbf{F}$, and is generally referred to as *stress relation*.
At this point it is necessary to introduce the *principle of material frame indifference*, which states that constitutive equations must be objective with respect to any change of the observer. It is fundamental in this framework, because it imposes certain restrictions on the previously defined response function $\mathfrak{g}$ that are fundamental for the design of constitutive equations consisted with the presented theory. In particular, any change of the observer is defined as a change of frame from $\mathbb{R} = \{O, \mathbf{e}_k\}$ to $\hat{\mathbb{R}} = \left\{\hat{O}, \hat{\mathbf{e}}_k\right\}$, as defined by

$$\hat{\mathbf{x}} = \mathbf{c}(t) + \mathbf{Q}(t)\mathbf{x} \tag{39}$$

where $\mathbf{c}(t)$ is the position vector defining O from $\hat{O}$ and $\mathbf{Q}(t)$ is a proper orthogonal rigid body rotation of $\mathbb{R}$ relative to $\hat{\mathbb{R}}$. We shall also suppose that the reference configurations of the two observers is the same, and that the time scale is also the same, so that $\hat{t} = t$.

Under the frame change described in 39, the deformation gradient $\mathbf{F}$ transforms into $\hat{\mathbf{F}} = \mathbf{QF}$, and the right and left Cauchy-Green deformation tensors transform into

$$\hat{\mathbf{C}} = \mathbf{C} \quad \hat{\mathbf{b}} = \mathbf{QbQ}^{\mathsf{T}} \tag{40}$$

where $\mathbf{C} = \hat{\mathbf{C}}$ because of the use of the same reference configuration. Also, the rigid body motion defined in equation 39 maps the region Ω_t to a new region $\hat{\Omega}_t$, and the stress relation of equation 38 to the relation $\hat{\sigma}(\mathbf{x}, t) = \mathfrak{g}\left(\hat{\mathbf{F}}\right)$, where we postulate that the constitutive relation is postulated to be indifferent from the observer.

By considering that, for any proper orthogonal rigid body rotation $\mathbf{Q}$ the deformation gradient $\mathbf{F}$ maps to $\hat{F} = \mathbf{QF}$ and that $\hat{\sigma} = \mathbf{Q}\sigma\mathbf{Q}^{\mathsf{T}}$, it is possible to write that

$$\hat{\sigma} = \mathfrak{g}\left(\hat{\mathbf{F}}\right) = \mathfrak{g}\left(\mathbf{QF}\right) \quad \hat{\sigma} = \mathbf{Q}\sigma\mathbf{Q}^{\mathsf{T}} = \mathbf{Q}\mathfrak{g}\left(\mathbf{F}\right)\mathbf{Q}^{\mathsf{T}} \tag{41}$$

By combining the two equations, the following restriction for $\mathfrak{g}$ is obtained

$$\mathbf{Q}\mathfrak{g}\left(\mathbf{F}\right)\mathbf{Q}^{\mathsf{T}} = \mathfrak{g}\left(\mathbf{QF}\right) \tag{42}$$

By then employing the right polar decomposition of $\mathbf{F}$ of equation 16, it is possible to write $\mathbf{Q}\mathfrak{g}\left(\mathbf{F}\right)\mathbf{Q}^{\mathsf{T}} = \mathfrak{g}\left(\mathbf{QRU}\right)$, where $\mathbf{R}$ is the orthogonal rotation tensor. By then assuming that $\mathbf{Q} = \mathbf{R}^{\mathsf{T}}$ and by using the orthogonality condition for $\mathbf{R}$, a reduced form of equation 42 is obtained

$$\mathfrak{g}\left(\mathbf{F}\right) = \mathbf{R}\mathfrak{g}\left(\mathbf{U}\right)\mathbf{R}^{\mathsf{T}} \tag{43}$$

The associated stress relation is then

$$\sigma = \mathbf{R}\mathfrak{g}\left(\mathbf{U}\right)\mathbf{R}^{\mathsf{T}} \tag{44}$$

Equation 44 shows that the properties of an elastic material are independent from the rotational part of $\mathbf{F} = \mathbf{RU}$ if the constitutive relation is independent from the observer.

A *hyperelastic material*, also known in literature as a *Green-elastic material*, postulates the existence of a Helmholtz free energy density function Ψ defined per unit volume of the body. When, in particular, the free energy function can be defined as dependent on the strain state of the material independently from its strain history (i.e. $\Psi = \Psi(\mathbf{F})$), Ψ is generally called *strain energy function*, or just *strain energy*. For this kind of materials, it is postulated the existence of response functions $\mathfrak{g}$ and$\mathfrak{G}$ of the form

$$\mathbf{P} = \mathfrak{G}(\mathbf{F}) = \frac{\partial \Psi(\mathbf{F})}{\partial \mathbf{F}} \quad \boldsymbol{\sigma} = \mathfrak{g}(\mathbf{F}) = J^{-1} \frac{\partial \Psi(\mathbf{F})}{\partial \mathbf{F}} \mathbf{F}^{\intercal} \tag{45}$$

These response functions define, in a Lagrangian or an Eulerian reference system, the relation between deformation of the material and stress response. The derivative of *Psi* with respect to $\mathbf{F}$ denotes the gradient of Ψ, which is a second order tensor, introduced in equation 35 as the first Piola-Kirchhoff stress tensor. It is general practice to consider that the strain energy function Ψ vanishes in the reference configuration (this condition is generally known as the *normalization condition*) and, from physical observations, it comes that it increases with deformation, attaining then its global minimum for $\mathbf{F} = \mathbf{I}$. We can express these conditions by writing

$$\Psi = \Psi(\mathbf{I}) = 0 \tag{46}$$

$$\Psi = \Psi(\mathbf{F}) \geq 0 \tag{47}$$

Another important restriction applied on the constitutive equations for hyperelastic materials is based on one of their properties, which is called isotropy. This property is based on the idea that the material response is the same in all directions. This is mostly true when dealing with rubber, unless high-strain phenomena occur, like for example strain induced crystallization, which induces anisotropy (the

material properties become function also of the material orientation).
Consequently, it is generally asserted that a material is isotropic relative to the reference configuration if the values of the strain energy $\Psi(\mathbf{F})$ and $\Psi(\mathbf{F}^*)$, where $\mathbf{F}^*$ is defined to be the deformation gradient after any rigid motion of the system, are the same for all orthogonal tensors $\mathbf{Q}$ such that $\mathbf{F}^* = \mathbf{F}\mathbf{Q}^\intercal$, which means that

$$\Psi(\mathbf{F}) = \Psi(\mathbf{F}^*) = \Psi(\mathbf{F}\mathbf{Q}^\intercal) \tag{48}$$

Material isotropy allows to express constitutive laws of hyperelastic materials through the principal invariants of its argument, thanks to the *representation theorem for invariants*.
It is quite common in fact, to find strain energy functions expressed as a set of independent strain invariants of the symmetric Cauchy-Green strain tensors $\mathbf{C}$ and $\mathbf{b}$,

$$\Psi = \Psi\left(I_1(\mathbf{C}), I_2(\mathbf{C}), I_3(\mathbf{C})\right) = \Psi\left(I_1(\mathbf{b}), I_2(\mathbf{b}), I_3(\mathbf{b})\right) \tag{49}$$

where the invariants are defined as

$$I_1(\mathbf{b}) = \operatorname{tr}\mathbf{b} = \lambda_1^2 + \lambda_2^2 + \lambda_3^2 \tag{50}$$

$$I_2(\mathbf{b}) = \frac{1}{2}\left[(\operatorname{tr}\mathbf{b})^2 - \operatorname{tr}(\mathbf{b})^2\right] = \lambda_1^2\lambda_2^2 + \lambda_2^2\lambda_3^2 + \lambda_1^2\lambda_2^3 \tag{51}$$

$$I_3(\mathbf{b}) = \det\mathbf{b} = J^2 = \lambda_1^2\lambda_2^2\lambda_3^2 \tag{52}$$

Another convenient way to express constitutive laws is through the principal stretches. This can be done if the strain energy function Ψ is invariant with rotations; in that case, it is possible to write

$$\Psi = \Psi\left(\mathbf{C}\right) = \Psi\left(\lambda_1, \lambda_2, \lambda_3\right) \tag{53}$$

In this case the normalization condition takes the form $\Psi(1,1,1) = 0$.
Another important assumption about elastomeric materials is their incompressibility. Materials that keep their volume constant through deformation are characterized by the incompressibility constraint, $J = 1$; such materials can be referred to

as *constrained*, due to the procedure that needs to be adopted in order to find their correspondent strain field upon deformation.
For this kind of materials, the strain energy function can be assumed to be

$$\Psi = \Psi(\mathbf{F}) - p(J-1) \tag{54}$$

where the scalar p serves as an indeterminate Lagrange multiplier, and can be identified as a hydrostatic pressure. The scalar p, in general, can be determined through the boundary conditions or from the equilibrium equations, and represents a workless reaction to the kinematic constraint on the deformation field.
Isotropic behavior of elastomers have been thoroughly investigated by many authors under different approaches as will be shown later in this section. However, a satisfactory reproduction of the *complete behavior* of rubber materials (where "complete behavior" is intended as the material response under different loading conditions). Moreover, many authors tried to highlight different aspects of rubber elasticity, focusing then more on the elegance of the approach or on the physical justification of the model.
These aspects led through the years to a multitude of hyperelastic models, which vary in mathematical complexity, number of parameters and physical interpretation of the different parameters, in addition to achievable level of model efficiency in terms of difference between the experimental data and the fitted curves. Hyperelastic models can be divided in groups, based on the approach adopted for their development. The most common classification among different models divides them into three categories, as also shown in the work from Marckmann and Verron [77]:

- *Phenomenological models*, which are issued from mathematical developments of their strain energy function; some examples are the Ogden [90] model and the Mooney-Rivlin class of models [107, 108];

- *Physically-based models*, which are based on both physics of polymer chains network and statistical methods, and are focused more on the physical justification of the different material parameters used, such as the extended tube models from Heinrich and Kaliske [60].

In the next sections (1.2.3.1 and 1.2.3.2) a fast overview of the principal models for the two categories will be given, in order to give some remarks and to highlight the differences among the models.

1.2.3.1 *Phenomenological models*

As anticipated, phenomenological hyperelastic models are mostly focused on mathematical simplicity and in adequate description of the material behavior under finite strains in different loading conditions. Here will be briefly described the *Mooney-Rivlin based models*, the *Gent model* and the *Ogden model*.

MOONEY-RIVLIN MODELS Mooney [82], through observations, noted a dependence of the hyperelastic constitutive behavior upon the first and second invariants of the left Cauchy-Green strain tensors. Rivlin [107, 108] further extended this model to a polynomial series dependent upon the two invariants, defining the strain energy function of this class of models as

$$\Psi = \sum_{i=0,j=0}^{N} C_{ij} \left(I_1 - 3\right)^i \left(I_2 - 3\right)^j \tag{55}$$

Here, the parameters are C_{ij}, and $C_{00} = 0$. This model is mostly used up to the first or second order, and generally not to values higher than 200% in strain. However, expansion of this model to higher orders can give grat accuracy, at the cost of a multitude of parameters.

GENT MODEL In order to take into account for finite chain extensibility, Gent [40] considered that the first invariant should be limited by a maximum value, denoted as I_m, and proposed the following strain energy function

$$\Psi = -\frac{E}{6} \left(I_m - 3\right) \ln \left[1 - \frac{I_1 - 3}{I_m - 3}\right] \tag{56}$$

Here the parameters are E and I_m. This model gives good fitting results, thanks to the parameter I_m; however, the low number of parameters may also lead, in some cases, to a good mechanical characterization only upon some loading conditions.

OGDEN MODEL Ogden [90], in 1972, proposed to derive the strain energy function Ψ through the strain invariants defined by $I(\alpha) = \left(\lambda_1^\alpha + \lambda_2^\alpha + \lambda_3^\alpha - 3\right)/\alpha$, writing then the strain energy function as

$$\Psi = \sum_{n=1}^{N} \frac{\mu_n}{\alpha_n} \left(\lambda_1^\alpha + \lambda_2^\alpha + \lambda_3^\alpha - 3\right) \tag{57}$$

The parameters of the Ogden model are μ_i and α_i, with i going from 1 to the chosen N. They should follow the stability condition $\sum_{i=1}^{N} \mu_i \alpha_i > 0$. The Ogden model is characterized by a great flexibility (especially for $N = 2$ or $N = 3$), but is also featured by a quite high number of parameters. However, in its higher forms it is widely optimized and used in different commercial finite element software.

1.2.3.2 *Physically-based models*

Physical models are instead based on the finding of correlation between the parameters used and different physical properties of the material, such as the chain maximum extensibility or the crosslink density of the elastomer. Here we briefly review the Neo-Hookean model and the tube models, although many others could be cited, such as the chain model from Arruda and Boyce [6] and many of the models derived.

NEO-HOOKEAN MODEL The neo-Hookean model is considered by many as the most simple phenomenological model; however, it has been developed by Treloar in 1943 [125] from different considerations about molecular chain statistics. In fact, he considered elastomeric materials as constituted by a network of long flexible chains, randomly oriented and linked by chemical bounds at the junction points.

Moreover, he considered a Gaussian statistical distribution to estimate the number of chain conformations, and obtained the following strain energy density

$$\Psi = \frac{1}{2} nkT \left(I_1 - 3 \right) \tag{58}$$

where n is the chain density per unit volume, k is the Boltzmann constant and T is the absolute temperature.
Because of its simplicity, the neo-Hookean model is widely used for analytical calculations, and leads to good agreement with experimental results for low levels of strains (up to 50%).

TUBE MODEL The tube model, developed by Heinrich and Kaliske in 1997 [46] is based on the concept that every polymeric chain is constrained by the other chains to stay in a tube, due to the high degree of entanglement of this kind of polymers. The strain energy function for this model is defined as

$$\Psi = G_c I_1 - \frac{2G_e}{\beta} \left(\lambda_1^{-\beta} + \lambda_2^{-\beta} + \lambda_3^{-\beta} \right) \tag{59}$$

where G_c, G_e and β are three fitting parameters, which can be connected to physics of the polymer chains. Because of the strong limitations of this model in describing material behavior under large strains, Heinrich and Kaliske presented some years later a similar model, described in the next paragraph.

EXTENDED TUBE MODEL In 1999, Kaliske and Heinrich [60] updated their model to include chain extensibility, while also using a non-Gaussian distribution to describe the polymer chain length distribution. The strain energy function presented by them is

$$\Psi = \frac{G_c}{2} \left[\frac{\left(1 - \delta^2\right) \left(I_1 - 3 \right)}{1 - \delta^2 \left(I_1 - 3 \right)} + \ln \left(1 - \delta^2 \left(I_1 - 3 \right) \right) \right] - \frac{2G_e}{\beta} \left(\lambda_1^{-\beta} + \lambda_2^{-\beta} + \lambda_3^{-\beta} \right) \tag{60}$$

Here the parameters are G_c, G_e, β and δ. The last parameter, δ, allows to take into account finite chain extensibility.

While having only four parameters, this model allows to correctly describe and predict rubber mechanical behavior under complex loading history and at high levels of strain. In fact, it has also been judged my Marckmann and Verron [77] as one of the best hyperelastic models for rubber materials, because of its remarkable fitting and predictive capabilities.For these reasons, the Extended Tube model will be used through the Thesis in order to describe hyperelastic behavior of rubber.

Part II

RESEARCH ACTIVITIES

This section deals with different research activities. In Chapter 2, an an overview of biaxial testing for rubber is presented, together with novel approaches for mechanical characterization of filled elastomers; Chapter 3 describes an approach based on the model of Dorfmann and Ogden used in order to capture some relevant aspects related to the Mullins effect. Chapter 4 contains a proof of concept regarding the generalization of the Rivlin-Thomas approach to fatigue of rubbers with respect to planar biaxial samples.

2

BIAXIAL TESTING ON FILLED RUBBER

2.1 INTRODUCTION

2.1.1 *Biaxial testing on filled elastomers*

As stated in Chapter 1, elastomers are generally tested in more than one loading condition in order to obtain more reliable results in term of stress and strain response to solicitations of any kind. In fact, since hyperelastic materials show a non-linear stress-strain behavior, hyperelastic constitutive laws generally come in with a number parameters usually higher than 2; consequently, the need to test a material in different loading conditions ensures a better characterization of the mechanical behavior through more accurate curve fittings.
This is a standard approach with elastomeric materials, due to the complexity of the constitutive models used to describe the mechanical behavior of the material. For this reason, the different mechanical tests commonly applied on rubbers have some kind of 'identification names'. Moreover, thanks to the incompressibility assumption, it is generally possible to define the principal stretches in the different loading conditions. In particular, three tests are generally acknowledged as standard:

- *Uniaxial loading*, where the principal loading conditions are $\lambda_1 = \lambda$,$\lambda_2 = \lambda_3 = 1/\sqrt{\lambda}$;

- *Pure shear*, with its principal loading conditions defined as $\lambda_1 = \lambda, \lambda_2 = 1, \lambda_3 = \lambda^{-1}$;
- *Equibiaxial loading*, in which the principal stretches are $\lambda_1 = \lambda_2 = \lambda, \lambda_3 = 1/\lambda^2$.

In the previous definitions the parameter λ has been used in order to define the only independent variable through which the loading is applied. A graphical representation of the samples used in the context of this work can be found in Figure 7.

L. R. G. Treloar, one of the pioneers in the framework of mechanical testing on

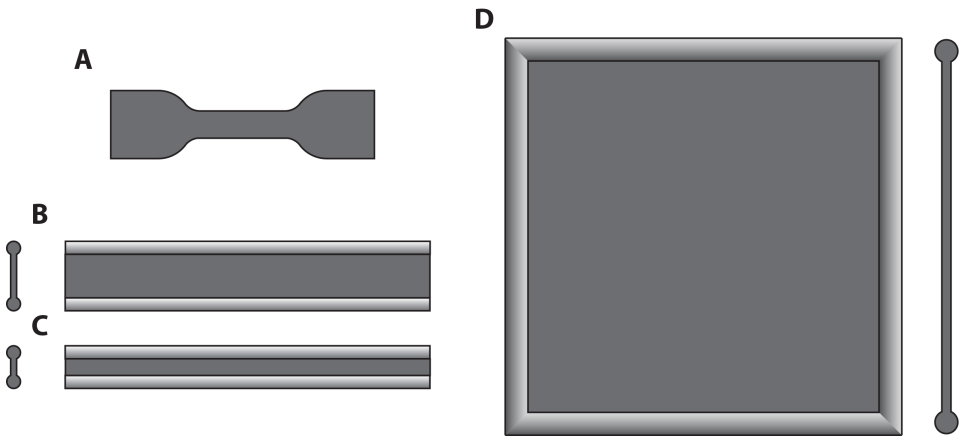

Figure 7: Different specimen shapes used for mechanical characterization. A) Uniaxial testing sample, with a width of 2 mm; B) and C) pure shear samples, with a nominal height of respectively 10 and 4 mm, a width of 80 mm and a thickness of 1.3 mm; D) BiaxTester squared specimens, with width and height of 77 mm and a thickness of 1.9 mm.

rubbers, in his fundamental work concerning this field [126] used four different loading conditions, namely:

- *2-Dimensional extension*, an equivalent of *equibiaxial loading*;
- *Simple elongation*, equivalent to the *uniaxial tension*;
- *Pure shear*;

- *Combined elongation and shear.*

His results are today acknowledged as benchmarks in order to evaluate predictability and fitting complexity of hyperelastic models, as can be seen in the works of Ogden et al. [93] and in the work of Steinmann et al. [122]. Marckmann and Verron [77] also used the data from Treloar (and from Kawabata, [62]) in order to make some sort of "ranking" of the various hyperelastic models, basing it on different parameters, e.g. the ability of the different models to accurately predict the behavior of the different loading conditions.
In this framework, biaxial testing of elastomers has always been a challenging kind of experiment, because of the complexity of the systems needed to realize the test and measure the obtained results, although its flexibility gives the opportunity to perform a great variety of tests, even for the imitation of complex loading conditions. Among the first experiments on this kind of loading conditions we surely find the ones from Treloar [126], already mentioned before, which were performed by inflating a rubber circular sheet clamped around its circumference into the form of a balloon. As reported by Treloar in [127], when inflating a circular sheet of rubber the strain field can be considered biaxial only *over a region in the neighborhood of the center of the sheet, or 'pole' of the spheroidal balloon*, to which the evaluations of the strain field must be limited.
Bubble inflation technique has been extensively studied in the last decades in order to get more reliable data through the use of new technology, such as digital image elaboration: for example, Reuge et al. [105] used a CCD video camera as optical extensometer and a pressure sensor to record both inflation state and blowing pressure, including the use of a magnetic probe in order to evaluate the bubble thickness over pressure increase in order to validate the experimental results obtained through the CCD camera. Starting from this kind of set-up, Rachik et al. [100] considered different strain energy functions and calculated the correspondent parameters using both direct identification procedures (using uniaxial and equibiaxial tension test data) and inverse identification techniques from bubble inflation and finite element analysis, showing that the latter was a good alternative to get material parameters thanks to the combination of different

techniques and the consequent parameter optimization. However, this technique results to be difficult to apply because of the high non-linearity of the solutions obtained through direct optimization of the parameters in the finite element code. Later, Sasso et al. [114] used bubble inflation technique together with a setup composed of two cameras and a 3D particle tracking software to determine the surface strain field of the inflated rubber sheet. The processed results were then used to fit different hyperelastic constitutive models and used in a Finite Element analysis software in order to compare the results with the experimental observations, showing that the application of such techniques leads to results comparable with the ones obtained through the use of 'standard' procedures.

In the last 15 years, however, many researchers focused on two different shapes

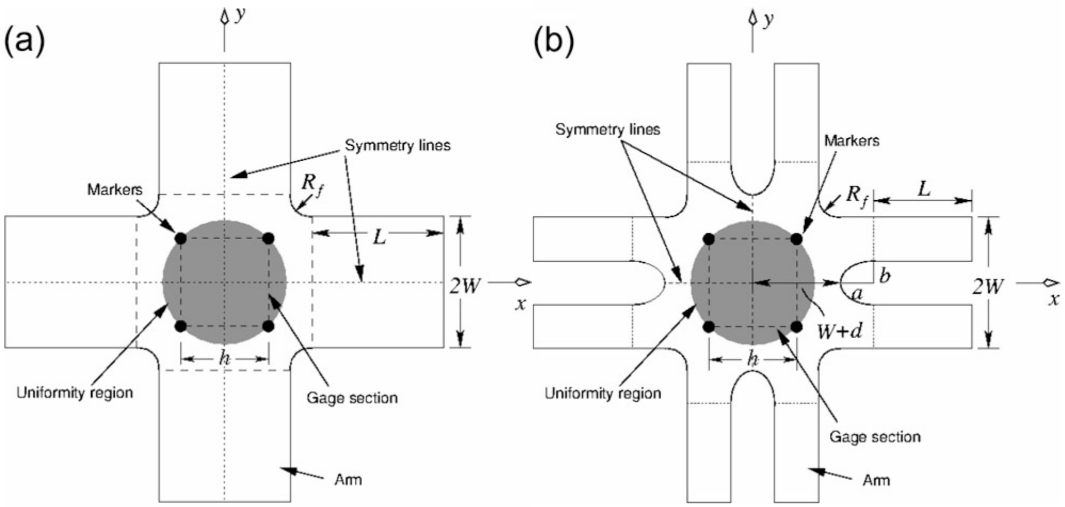

Figure 8: Cruciform specimens from Zhao et al. [133]. a) Standard cruciform specimen; b) Cruciform specimen proposed by Zhao et al.

for biaxial testing of elastomers, which are cruciform and squared samples. To the author's knowledge, Chevalier et al. [18] were the first to use a cruciform rubber specimen, together with an Image Correlation software, which allowed to determine the biaxial strain field in this sample. Other authors, such as Sasso et al. [115], further refined the Image Correlation technique to get more reliable results. Zhao et al. [133] tried to optimize cruciform samples with the aim of improving

the degree of uniformity of stress and strain in the test region while considering that such experimental setup should satisfy the two following conditions: the gripping method and the specimen itself should optimize load transfer from the grippers to the symmetry lines of the specimen; normal stresses over the symmetry lines should be uniform within the reference length for determining the nominal stresses, in order to get a reliable correspondence between the registered nominal stress and the nominal stresses in the sample. For this reason, they proposed a new specimen design, displayed un Figure 8. Other works on cruciform sample optimizations are, for example, the works from Hu et al. [54] and Andrusca et al. [5]. However, cruciform specimens are known to be difficult to handle because of the poor uniformity of stretches in the test piece. In fact as reported in [36], the stretch registered on the branches of such specimens is larger than that at the center, where it is really difficult to achieve strain values higher than 30%.

Squared samples partially solve these kinds of problems, thanks to the different shape. However, in this case the clamping system plays an important role due to different effects generated by the clamps, such as compression or shear strains in the edge portions of the sample, together with over-constraint of the sample deformation when using clamping systems that do not have the ability to adapt their shape to the deformation of the sample itself, as the ones used for cruciform specimens. For the latter, clamping systems composed of small clamps and linear rails are generally used, so that the sample edges are not necessarily constrained to stay undeformed throughout the biaxial testing. Moreover, the deformation in such samples can be highly inhomogeneous due to the vicinity of the clamping system and the area to be measured: for this reason, different authors tried to solve this ind of problem in many different ways. For example, Fujikawa et al. [37] proposed to subtract the contribution of the rubber between the clamps by using an heuristically determined equation. Later, Fujikawa et al. [36] proposed a different experimental approach, which consisted in notching the rubber sheets between the different clamping arms. This approach brought them to optimize the shape of the cut through the employment of Finite Element software to to

verify the effectiveness of the aforementioned approach. A similar approach has been also used on the BiaxTester, as can be seen in the later sections of this Chapter.

2.1.2 *Comparison of different software for Digital Image Correlation*

Digital Image Correlation (often referred to as DIC) is an non-contact optical technique that allows measurement of surface deformation and particle motion in a specific Region Of Interest (ROI) on previously treated objects through the use of tracking techniques and correlation analysis. This method is based on the division of the ROI in different subsections (i.e. groups of pixels, often called *subsets*) and on the subsequent identification of the locations of such subsections in consecutive images through image processing and correlation techniques, which basically help to somehow obtain a one-to-one correspondence between material points in the reference and current configurations (respectively the first image and the subsequent ones). This is done by obtaining displacement and strain information through the transformation used to match the location of the subset in the current configuration. The tracking and strain identification, when applied on multiple subsets on the whole region of interest gives then a discrete displacement field, which can then be translated to both strain and velocity field of the surface points of the object to be analyzed. The technique was initially employed only in the case of 2D surface mapping, however it rapidly evolved to a 3-D technique, called Stereo Digital Image Correlation (SDIC).
The technique is based on the assumption that considering a subset as a group of coordinate points, it is possible to find the transformation of the initial reference subset points to the current configuration. This transformation is typically constrained to be linear and of the first order –although in the case of large strains it

is possible to consider second-order transformations, as can be seen in the work from Lu and Cary [74]– :

$$\widetilde{x}_{cur_i} = x_{ref_i} + u_{rc} + \frac{\partial u}{\partial x_{rc}}\left(x_{ref_i} - x_{ref_c}\right) + \frac{\partial u}{\partial y_{rc}}\left(y_{ref_j} - y_{ref_c}\right) \tag{61}$$

$$\widetilde{y}_{cur_j} = y_{ref_j} + v_{rc} + \frac{\partial v}{\partial x_{rc}}\left(x_{ref_i} - x_{ref_c}\right) + \frac{\partial v}{\partial y_{rc}}\left(y_{ref_j} - y_{ref_c}\right) \tag{62}$$

where x_{ref_i}, y_{ref_j}, x_{ref_c} and y_{ref_c} are respectively the x and y coordinates of an initial reference subset point and the x and y coordinates of the center of the initial reference subset; $\widetilde{x}_{cur_i}$ and $\widetilde{y}_{cur_j}$ are, instead, the x and y coordinates of a final current subset point. The subscripts (i, j) are the indices used for the relative location of the subset points with respect to the center of the subset, as well as for correspondences between subset points in the current and reference configuration. The subscript rc used in 61 means that the transformation is from the reference to the current coordinate system. The different parameters are then here grouped in the vector p:

$$p = \left\{ u,\ v,\ \frac{\partial u}{\partial x},\ \frac{\partial u}{\partial y},\ \frac{\partial v}{\partial x},\ \frac{\partial v}{\partial y} \right\} \tag{63}$$

The objective of this kind of analysis is then to find the optimal p, such that the transformation of equation 61 gives the best possible correspondence between the reference coordinates x_{ref_i} and y_{ref_j} and the current coordinates $\widetilde{x}_{cur_i}$ and $\widetilde{y}_{cur_j}$. This is done through correlation criteria, which allow to establish a metric for similarity between the final reference subset and final current subset. However, this is beyond the scope of this Thesis; for more information about these aspects, the reader is addressed to the works from Lu and Cary [74] and the work from Blaber et al. [10].

The two software based on this techique and used through the whole PhD work are a commercially available software, GOM® ARAMIS, and a free toolbox for MATLAB, called NCorr and developed by Justin Blaber (please refer to *www.ncorr.com* and to the work from Blaber et al. [10] for more information). The two software are different in both capabilities and data handle: in fact, as for example ARAMIS

can handle stereo images and perform SDIC, NCorr does not have this kind of feature; moreover, the shape of the subsets handled by the two software are different. Moreover, while ARAMIS is a widely used software in the rubber industry, the NCorr toolbox is fairly new, and few validations of this software under large deformations have been performed. Due to the generally high loadings applied on elastomers, this validation results to be an important factor. Because of this aspect, a primary evaluation of the registered differences between the software has been performed, showing that no differences are registered on the displacement fields of the two software compared. This evaluation has been performed by using the same images of an equibiaxially stretched sample on the two different software and then comparing the displacement and deformation fields. This comparison led to the validation of the obtained results, as can be seen in Figure 9 for the displacements and in Figure 10 for what concerns the deformation fields.

2.1.3 *The BiaxTester*

The BiaxTester, produced by Coesfeld GmbH. & co. KG, is the prototype of a testing machine developed in order to test squared rubber specimens under planar biaxial loading conditions. It is actually under testing phase at the *Leibniz-Institut für Polymerforschung e.V.* in Dresden.
The testing system, shown in Figure 11, is constituted by 4 electromechanical drives, and each drive is equipped with a travel and force sensor. Each drive can run an individual motion profile under certain ranges, as shown in Table 1, and the user can choose the kind of dynamic movement from standard (e.g. sine, pulse, rectangular, triangular and sawtooth waves) or custom-made profiles, which can be uploaded and inserted in the software as `.csv` files, giving a great customization for what concerns the testing phase. Moreover, the drives and the motors can independently handle high levels of total strain applicable on the sample, together with high frequencies in dynamic loading; however, although each motor could move independently, it is generally suggested to always symmetrically move the

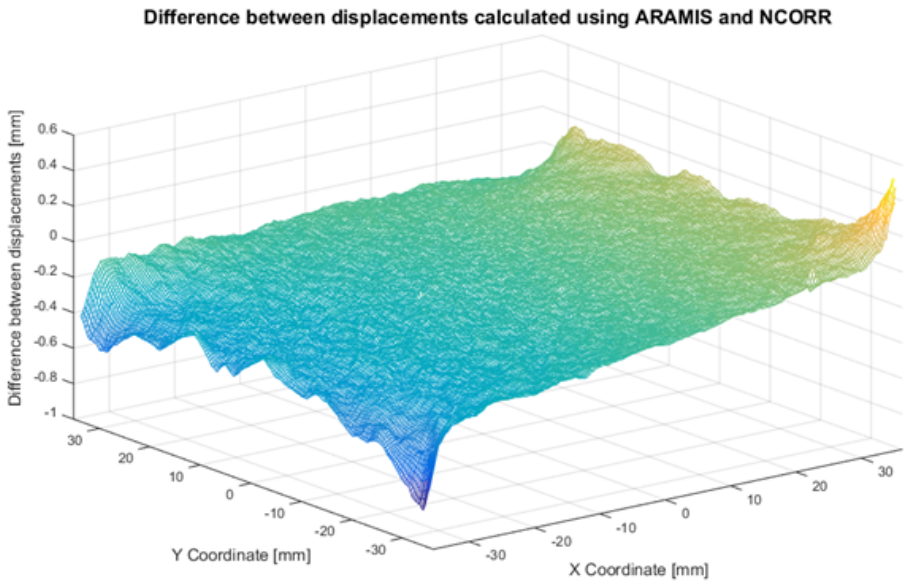

Figure 9: Comparison of the displacement fields obtained through ARAMIS and NCorr. The maximum difference between the two displacement fields is of about 0.7 mm on a total imposed displacement of 30 mm ($\sim$ 2.3% of the total displacement), which is an acceptable result, given the substantial differences in the calculation procedures of the software.

opposite motors.

Some of the most interesting features of this kind of tester are, for example, the possibility to perform tests at arbitrary loading (and displacements) in the two directions, and the possibility to perform quasi-static and dynamic tests on the materials. Nevertheless, The Biaxial Tester gives the possibility to test the rubber in a variety of different loading conditions, which surely can be a useful tool to enhance the understanding and fitting of the complex mechanical behavior of filled elastomers.

This testing machine is also equipped with an infra-red video capture system, composed by an IR-camera and two infrared light sources, as can be seen in Figure 11; the camera is a a JAI® BM-500GE, a monochrome progressive scan camera with 5 megapixels resolution and GigE Vision (GE) interface, through which is possible to automatically transfer the images on a personal computer through the Ethernet

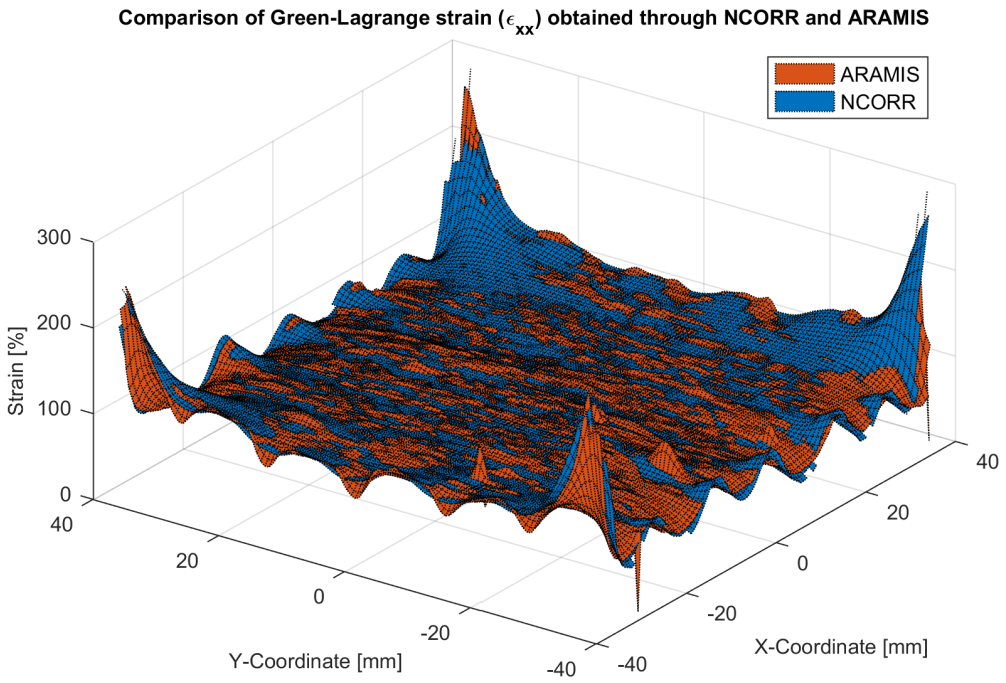

Figure 10: Comparison of the Green-Lagrange strain ϵ_{xx} obtained through NCorr and ARAMIS. A partial smoothing of the data obtained through NCorr can be seen on the edges, while in the rest of the sample the fields overlap each other, showing that there is almost no difference in the registered values.

port; the Charged Coupled Device (CCD) sensor can operate at 15 frames/second in continuous mode. The two light sources give the possibility to contemporaneously take images through transmitted and reflected light, which are needed to respectively investigate the surface strain (or displacement) field and crack edge –or length– in crack propagation analysis.

The samples mounted on the BiaxTester were initially rubber slabs with dimensions 100mm x 100mm x 1mm. However, the shape of such samples have been continuously upgraded through the years in order to get more reliable results from the machine itself. The rubber slabs were, in fact, tightened in the clamping system through normal screws, thus resulting in compression states and deformation around the clamps themselves, connected to shear stresses in the same region upon stretching of the sample. For this reason, a different sample and clamping system

Parameter	Features
Load range	1-1000 N
Load speed	0.1-50 Hz (0.1-10 Hz with displacements above 10 mm)
Maximum displacement	60 mm for each side (120 mm in total)
IR camera	Automatic or triggered acquisition (1 image per second)
Displacement sensor	Precision of ∼0.1 mm
Load Cells	Precision of 1N; maximum detectable load of 2kN

Table 1: General features of the Biaxtester produced by Coesfeld GmbH.

has been developed. The sample, as depicted in Figure 7 has an outer beaded edge and smaller overall dimensions, so that the clamping system interferes with the sample, resulting in lower (and in some cases negligible) compression of the sample edges. Another important upgrade has regarded the substitution of the whole steel clamping system with a new one, completely redesigned and made of Carbon fiber Reinforced Polymer (CFRP) which, thanks to the low weight and the longer rails, allows to both reach larger displacement levels and reach higher loading frequencies. The old and the new clamping systems can be respectively seen in Figures 12 and 13.

2.2 CLAMPING SYSTEM AND SPECIMEN OPTIMIZATION

In order to optimize reliability of the results obtained through the BiaxTester, different analyses have been performed concerning the various types of deformation and the resulting strain field on the sample surface. Study of the feasible sample geometries and the need to find a possible optimal shape that would fit into the —recently updated— carbon fiber clamping system led to three different specimen shapes, all displayed in Figure 14. The three shapes have two important differences:

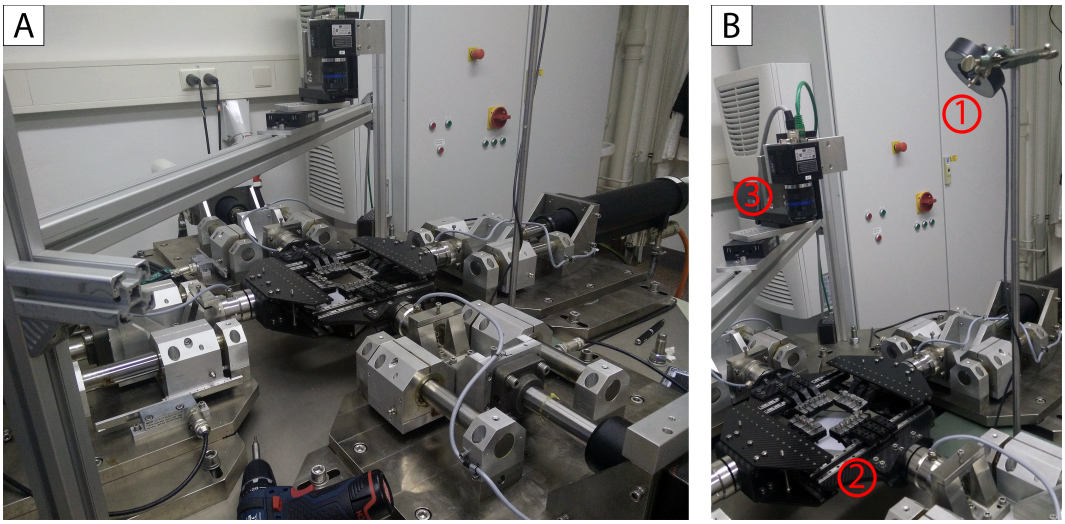

Figure 11: The BiaxTester at the *Leibniz-Institut für Polymerforschung e.V.*. A. Photo of the whole system. B. Detail of the image acquisition system: 1-Light for the images with reflected light; 2-Light for the images T; 3-Infrared camera for image and video acquisition.

- samples B and C present notches in between the clamping arms, in order to avoid the necessity to take into account the deformation of these regions in the refinement of the force-displacement results;
- samples C are tested with a slightly different clamping system, with the two angular orthogonal clamps connected by a single upper clamp, in order to reduce the shear phenomena on the sample corners.

It is necessary to point out that, due to the complex shape of the final product, the notches were hand-made on the samples by using a die cutter, therefore no direct study on the notch dimension was done, as for example is possible to see in the work from Kawabata [36]; however, all the notches have a width of 2 mm.

In order to broaden as much as possible the strain field spectrum in the tests used to compare the different samples, a test involving as many as possible loading configuration has been applied. It is depicted in Figure 15, where it is possible to see the movement on the different clamps vs time and vs. each other. This kind of loading can be divided in three different regions:

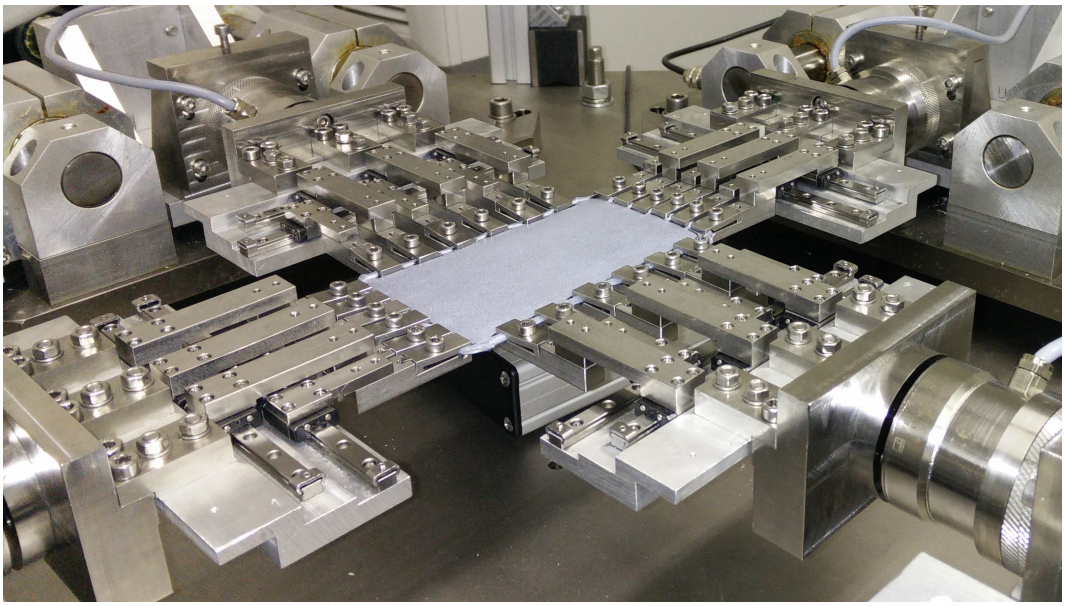

Figure 12: Detail of the old BiaxTester clamping system.

- a first region in which the loading can be described as simple pure shear;
- a second region in which the displacement of two opposite motors is fixed and the transversal motors move up to reaching the same displacements of the other motors;
- a third region in which the four motors move at the same speed, maintaining the same level of displacement, as in equibiaxial loading.

A test like this covers different aspects that are generally encountered when biaxially loading a rubber sample, and gave us the possibility to fully test the performances of the three samples described before. Moreover, in order to evaluate in the widest possible range the capabilities of the different samples, different aspects have been taken into account for what concerns the strain field. In fact, every sample has been tested with the same loading condition and the same program setup while the CCD camera, whose trigger is integrated in the "control box" of the BiaxTester, would take images of the samples at the same displacement values. Such images have been analyzed with the Digital Image Correlation software GOM®

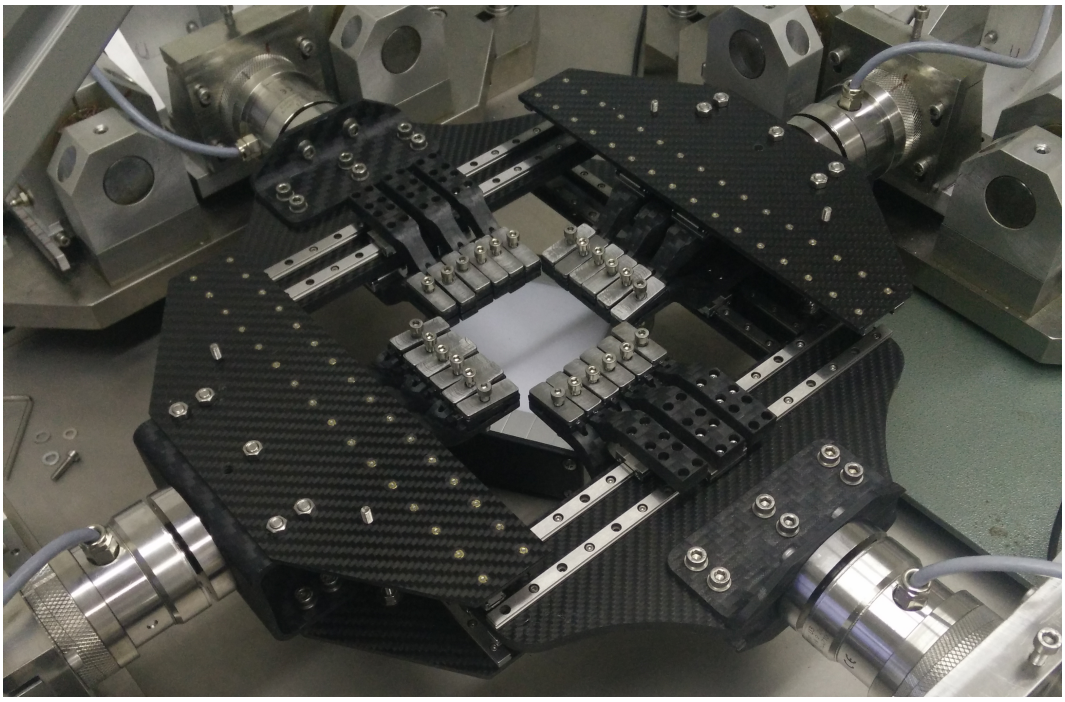

Figure 13: Detail of the BiaxTester CFRP clamping system.

ARAMIS. Results from the DIC analysis were then refined in order to extract four different parameters:

- The mean of the major strain on the sample surface, $\bar{\lambda}_1$;
- the amount of surface subsets whose principal strain was close ($\pm 5\%$ of the calculated $\bar{\lambda}_{max}$) to the average value calculated before;
- The mean value of biaxiality on the sample surface,$\bar{B}$, defined as

$$B = 1 - \frac{(\lambda_1 - \lambda_2)}{(\lambda_1 - 1)} \tag{64}$$

  where λ_1 and λ_2 are respectively the first and the second principal stretches;
- the amount of surface subsets whose biaxiality was close ($\bar{B} \pm 0.05$) to the average value calculated before;

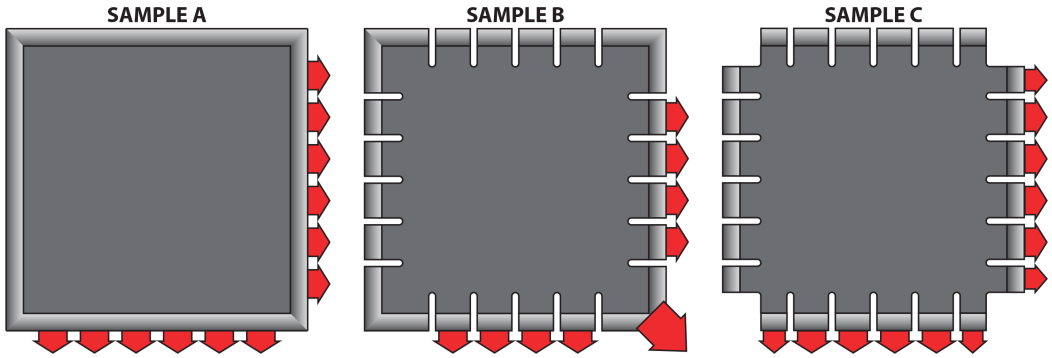

Figure 14: Illustration of the different sample shapes investigated.

This parameter has been chosen because for each loading condition applicable on the BiaxTester it has a specific value regardless of the loading magnitude. In fact it is equal to 1 for equibiaxial loading conditions, to 0 in pure shear loading and between 0 and 1 for any other biaxial loading state. This means that, for this particular test, the biaxiality will vary through the different regions of the test as in Figure 16. However, this parameter is not defined when there is no registered strain on the images subsets, i.e. in reference configuration, so it has been used only as an instrument to quantitatively evaluate the strain state of the sample in this particular case and, in general, should be carefully used.

Results from the analysis of the three samples can be seen in Figure 17, where the two upper graphs show the mean of the major strain on the surface of the different samples and the mean biaxiality parameter obtained through the DIC analysis. The lower graphs show, instead, the percent of the analyzed srface with parameters close to the averages calculated before. The trends show that, on comparison, the sample that achieves the best performances (intended as closer to the theoretical behavior of fully homogeneous deformations on the sample surface, as shown in Figures 15 and 16) is the sample with notches between the clamps and interlocked angular clamps (sample C on Figure 14). On the standard sample (sample A on Figure 14), the presence of material between the clamps heavily affects the homogeneity of the deformation field, especially on the borders, and in fact on this kind of sample only a small portion of it can be really

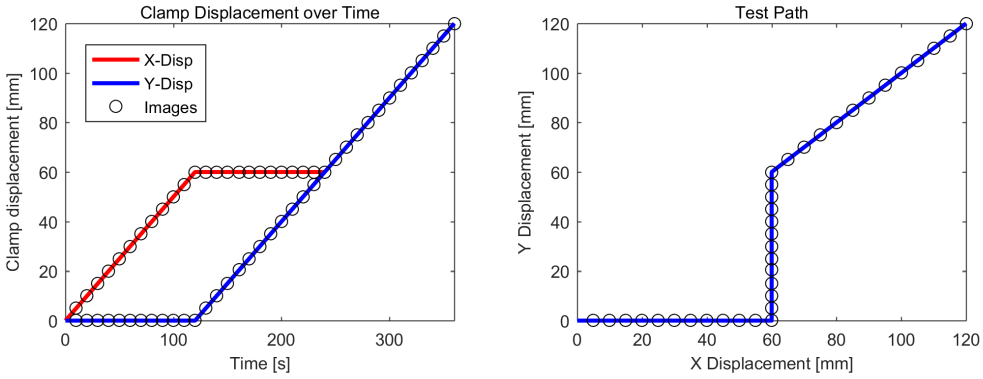

Figure 15: Displacements along x and y direction in the benchmark test. The displacements are shown over time and in the x-y displacement graph; the black circles represent the images taken by the camera during the test.

considered as homogeneously deformed; further analyses showed, in fact, that only the central region, with a diameter of roughly 40mm, can be considered as homogeneous. The behavior of the sample with notches and without interlocked clamps (sample B in Figure 14) lies somehow in the middle: in fact, although the notches alter the deformation behavior between the clamps, the orthogonal stretch of the angular clamps generate a high amount of shear stresses on the sample angles, reducing the overall region which is homogeneously deformed.

Concerning the mean values of major strain and of biaxiality, as can be seen in Figure 17, sample C behaves better than the others with respect to higher (and consequently closer to the theoretical value) overall major strain and biaxiality values closer to the theoretically foreseen, displayed in Figure 16. This approach, similar in terms of results to the work of Fujikawa et al. [36] has given many insights about the understanding of both Digital Image Correlation techniques and of how rubber samples behave under complex loading conditions; moreover, the promising results obtained through the Digital Image Correlation led to the investigation of any discrepancies between BiaxTester data and data from conventional testing machines.

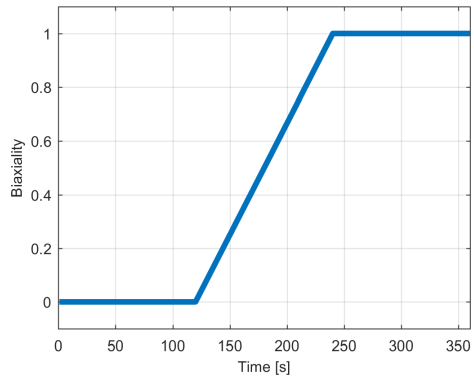

Figure 16: Biaxiality, as defined in equation (64), in the benchmark test. The black circles represent the images taken by the camera.

2.3 COMPARISON OF PURE SHEAR DATA FROM THE BIAXTESTER AND THE CONVENTIONAL PURE SHEAR SPECIMENS

Thanks to the capabilities of the BiaxTester, it is possible to test materials over a wide range of deformation going from Pure Shear loading (where, for incompressible materials, $\lambda_1 = \lambda, \lambda_2 = 1, \lambda_3 = 1/\lambda$) to equibiaxial loading conditions (where, instead, $\lambda_1 = \lambda_2 = \lambda, \lambda_3 = 1/\lambda^2$). This led to the possibility of effectively compare the data obtained through the BiaxTester with more conventional data obtained through the use of different testing machines, such as the Instron® Electropulse E100, a dynamic testing machine. The latter was used to test pure shear samples, as the ones depicted in Figure 7. Moreover, in order to include in this analysis more dependence of the data upon geometry of the samples, pure shear samples with a different height-width ratios were used through the analysis. Two particular aspects were investigated with reference to possible differences among the samples: at first, different analyses were performed through digital image correlation instruments, in order to evaluate the strain field over the different samples surface, in order to highlight any possible effect due to the presence of the edges in pure shear specimens; afterwards, different comparisons were made through stress comparison between the different samples. In particular, every test

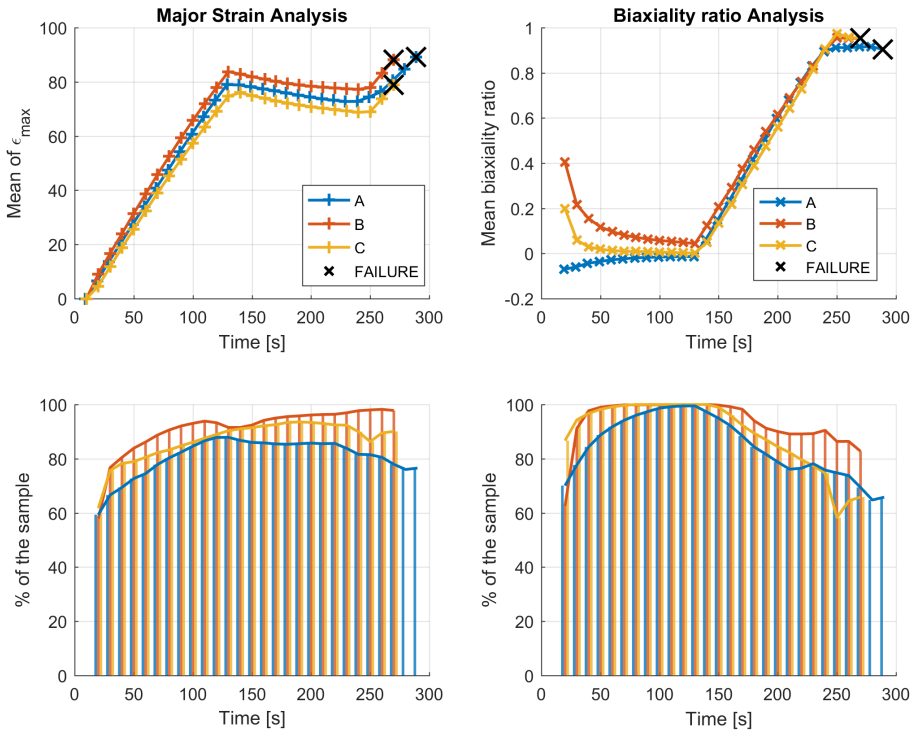

Figure 17: Results obtained for the three kinds of samples during the test depicted in Figure 15. It is evident how, among the three different samples, the one having the most homogeneous strain fields is the sample B (represented by higher percentage of the sample being at the predicted major strain and biaxiality levels, as can be seen in the two lower graphs). Moreover, the same sample presents also a more higher level of major strain attained in the during the whole test, thus showing a behavior closer to the theoretical one.

has been performed at the same strain rates and with samples composed of styrene-butadiene rubber filled with 50 phr of carbon black; moreover, in order to exclude any phenomenon related to different vulcanization time or other phenomena possibly connected to aging, all the samples have been cut from the same vulcanized rubber sheet, and then tested after 24 hours, while being kept at 20° C. Results from

Step	Amplitude (%)	BT single clamp displacement (mm)	Instron imposed displacement (mm)
1	10%	3.85 mm	1 mm
2	20%	7.7 mm	2 mm
3	30%	11.55 mm	3 mm
4	50%	19.25 mm	5 mm
5	70%	26.95 mm	7 mm
6	90%	34.65 mm	9 mm
7	110%	42.35 mm	11 mm
8	140%	50.05 mm	13 mm
9	150%	57.75 mm	15 mm

Table 2: Maximum amplitudes imposed on the BiaxTester and on the standard pure shear samples in order to compare results.

digital image correlation are shown in Figure 18, where it is possible to evince that, in the case of pure shear samples tested with the Instron Electropuls, there is an evident effect on the strain state at the edges of the sample; this effect generates compressive strain state in the direction transversal to loading for approximately twice of the initial height of the sample. This edge effect, noticed also by Treloar [126], generates an inhomogeneous strain field along the edges of the sample, which is generally neglected also through the use of samples with a higher ratio between width and height. Biaxial samples, instead, seem to be not influenced by this kind of effect, as is also shown in Figure 18 because of the clamped edges. In fact, the material cannot undergo compressive deformation in direction transversal to loading because of the clamping system; this gives to the BiaxTester samples a strain homogeneity which is basically unachievable with a normal pure shear sample.

Comparison of the stresses lead to almost the same conclusions: in fact, as can be seen in Figure 19, stress-strain curves obtained through the BiaxTester are remarkably higher than the ones obtained through the Instron Electropulse with pure shear specimens, as if specimens tested in the BiaxTester behave more rigidly. In order to try to reduce this kind of effect, an approach also mentioned by Treloar [126] has been adopted, which consisted in 'correcting' the stress-strain behavior by trying to remove the contribution of the outermost parts of the sample. This approach consists in testing samples with different widths and subtracting the resultant force registered on the narrower sample from the one obtained by using the wider one; after this, it should be in theory possible to calculate the stress acting on the central part of the sample. However, this approach did not lead to any improvement in the stress measurement, although tested by using a wide range of sample width (ranging from 40 mm to 70 mm together with an 80 mm sample for the 'normal' pure shear calculations), and is not displayed here. However, as displayed in Figure 20, the use of samples with a lower height-width ratio gives performances which are closer to the ones obtained with the BiaxTester.

2.4 BIAXIAL INVESTIGATIONS ALONG DIFFERENT LOADING PATHS

As anticipated before, rubber mechanical behavior has been widely investigated also in terms of multiaxial testing; apart from the ones cited before, an interesting work within this framework is the one from James et al. [59], where an approach similar to the Digital Image Correlation was applied in order to accurately determine the strain state of biaxially stretched elastomers.
However, to the author's knowledge very few works focus on the biaxial behavior of rubbers through different loading paths: up to now, in fact, a similar approach has been applied only by Kondo et al. [65], however for a different purpose and with relatively different materials (in that case, in fact, a two-step load application was used on polyrotaxane crosslinked via cyclic molecules in order to study aspects of the strain-induced swelling); one of the reasons for this lack in literature

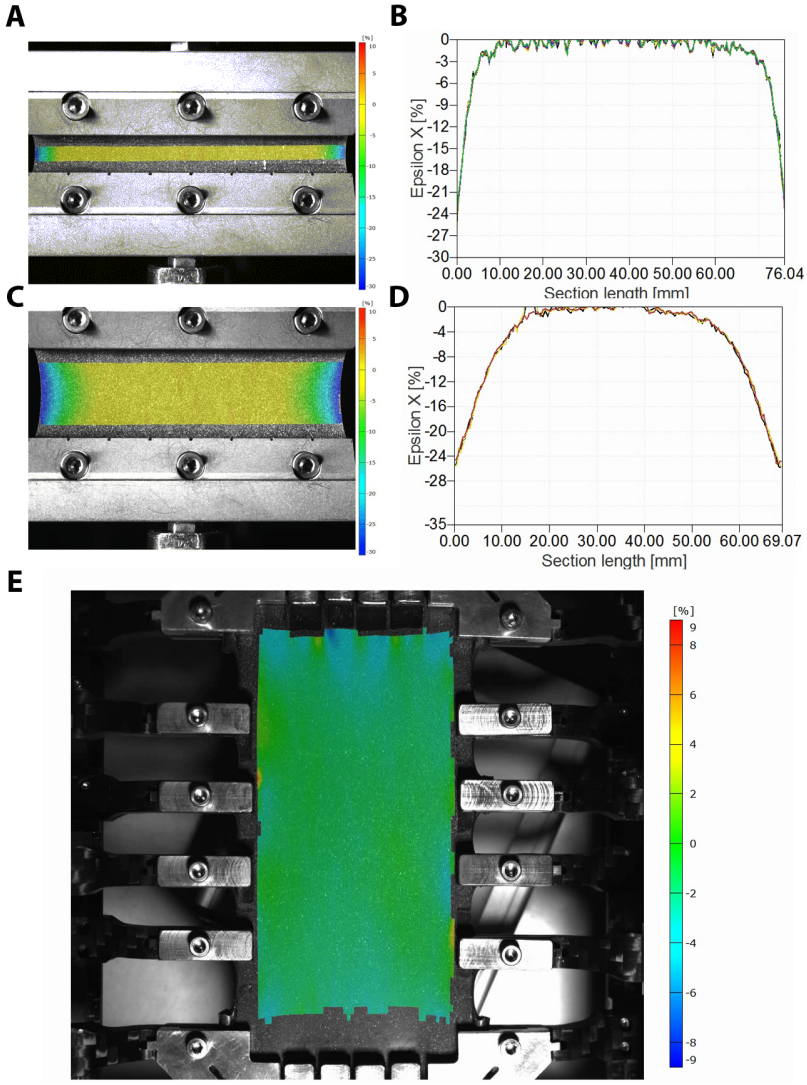

Figure 18: Results from DIC evaluation. A) strain field ϵ_{xx} in samples with a height of 4 mm; B) variation of the strain field along the sample with 4 mm as nominal height C) strain field ϵ_{xx} in samples with a height of 10 mm; D) variation of the strain field along the sample with 10 mm as nominal height; E) strain field in the direction transversal to loading for BiaxTester samples.

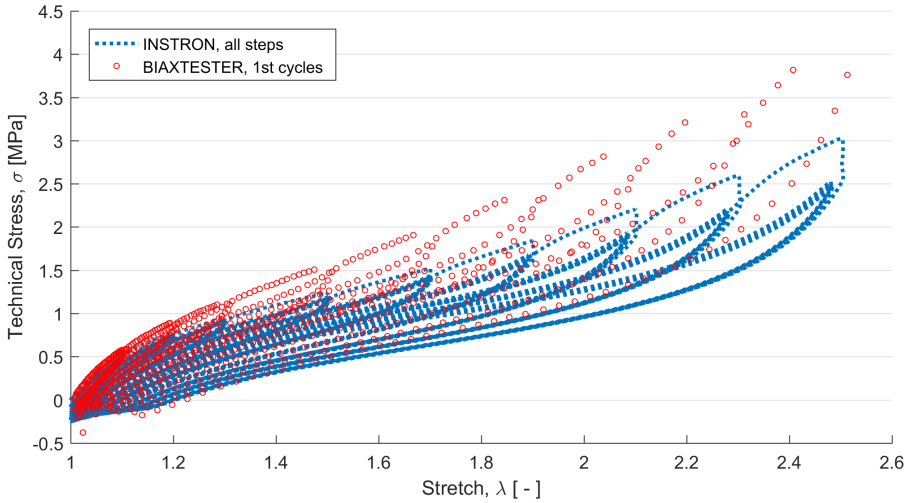

Figure 19: Data comparison between cyclic loading of BiaxTester and conventional pure shear samples.

probably resides in the lack of biaxial testing machines available today. In fact, although biaxial testing through bubble inflation techniques (as in the work from Treloar [126] or the one from Reuge et al. [105]) is in general an easy way to test such elastomers, it is not possible to truly vary the strain state of the inflated rubber sheet (apart from varying the circular clamp that 'pins' the rubber sheet, which theoretically should give a different strain state on the pole of the inflated surface); also, testing with cruciform specimens seems not an option on this context because of the difficult correlation between the imposed displacement and the registered strain on the sample surface, which can be done only in case of testing machines with the possibility of controlling the displacement of the transverses through the registered strain on the surface (which, in most cases, is not a viable way due to the complexity of the system and to the necessity of fine-tuning the strain field calculations through real-time digital image correlation).

In case of biaxial testing of squared samples, however, this approach seems really promising due to the high constraints imposed on the samples during the different deformation steps in basically any imposable loading condition, as seen in the previous section. Moreover, this approach may lead to better understanding of the

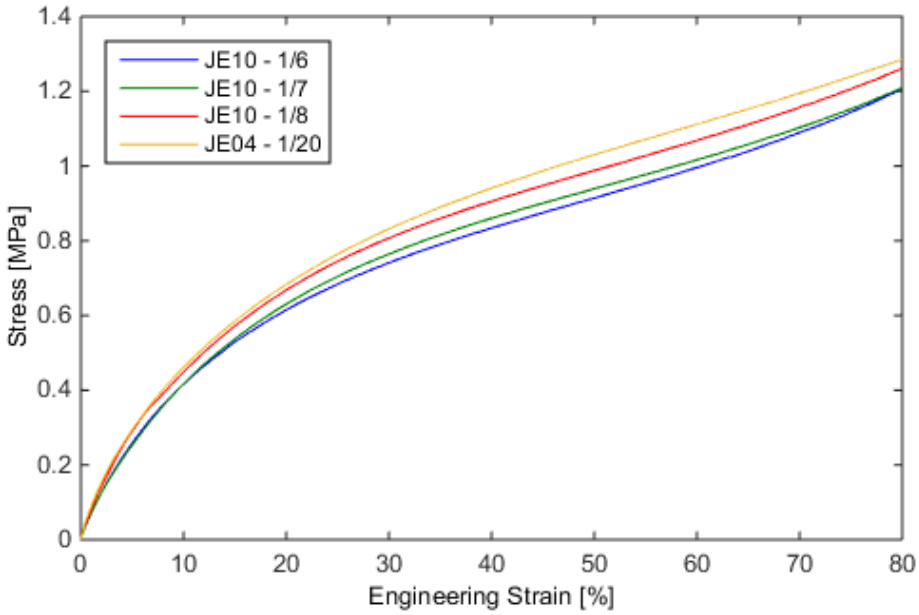

Figure 20: Data comparison between pure shear samples with a different height-width ratio, displayed in the legend.

rubber behavior and of the filler contribution, due to the complex loading regime imposable in this way.

For this reason, three different paths have been chosen for this kind of test, as depicted in Figure 21: in particular, path 1 may be associated to pure shear loading in the first part, where $\lambda_x = \lambda$ and $\lambda_y = 1$; after that, loading starts in the orthogonal direction while clamps in the first one stay still ($\lambda_x = \overline{\lambda}$ and $\lambda_y = \lambda$). Path 2 is instead a simple equibiaxial loading, where $\lambda_x = \lambda_y = \lambda$, and path 3 is a combination of the two, because for every step one of the two sets of clamps stay still while the other is moving; this 'stair-like' movement of the clamps is in fact basically what happens in Path 1, but with more steps. Finally, Each of the test as performed at ambient temperature, and all the different tests lasted the same amount of time ($t = 120s$), in order to put the samples in the same testing conditions. Images taken during the tests, and subsequent strain field evaluation through digital image correlation have been used to ensure that there were no deviations of

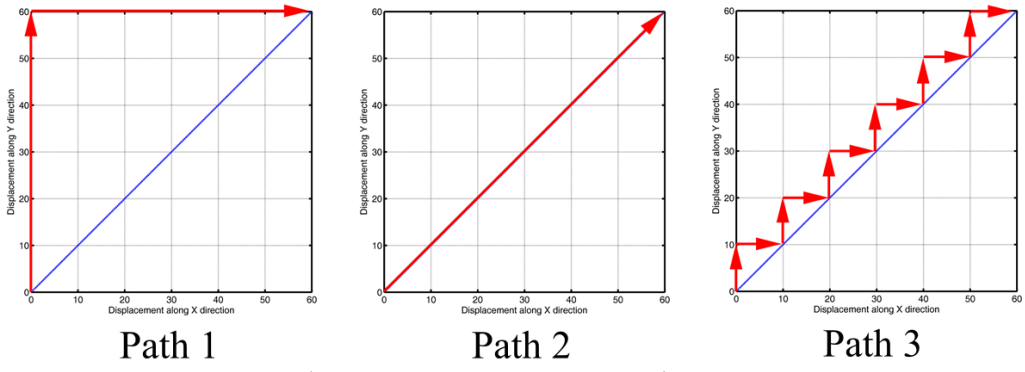

Figure 21: The three different paths in terms of displacement of the clamps in the orthogonal directions. Path 1 may be associated to pure shear loading in the first part, and then loading in the orthogonal direction while keeping the other one fixed; Path 2 is a simple equibiaxial loading; Path 3 is a combination of the two, and in fact the 'stair-like' movement of the clamps is basically what happens in Path 1, but with more steps.

the strains from the imposed ones. Finally, every sample has been preconditioned with 20 cycles of equibiaxial loading up to a maximum displacement of 60 mm, the same maximum loading of the three path tests.

In order to exclude as much as possible any effect related to strain induced crystallization, this ind of test has been performed on both rubber that crystallize under strain, such as Natural Rubber (NR) and rubbers that are not subjected to this kind of phenomenon, as Butadiene Rubber (BR). Moreover, in order to obtain information about the influence of the compound on the behavior registered by the sensors on the BiaxTester, the BR was mixed with NR for the third type of elastomer. All the data described about the different compounds are summarized in Table 3. The obtained results are then shown in Figures 22, 23, 24, 25 and 26. It is possible to notice, as also underlined in Table 4, that at the end of the tests (i.e. when the sample is finally equibiaxially loaded in all the three different paths) along path 1 and 3 there is a difference in the orthogonal registered forces, which is then translated in a difference in the nominal stresses. Moreover, this difference tends to increase as the amount of filler is increased and as the path is further from the equibiaxial load-

Rubber code	NR (phr)	BR(phr)	SBR (phr)	CB (phr)
A	0	100	0	50
B	100	0	0	50
C	50	50	0	50
E	0	0	100	50
F	0	0	100	25

Table 3: Composition of the tested rubbers

ing condition, as noticed by doing the same experiment with Styrene-Butadiene rubber with different amounts of carbon black. Another important thing to notice, especially in the cases of rubbers A and E, is that there seems to be some kind of relaxation effect at the beginning of any loading combined with an increase in registered stress (this one due to stretching in the orthogonal direction). This effect, although unexpected, is in general connected to stress relaxation of filled rubber under constant strain application. However, the unusual phenomenon is that this kind of relaxation arises during loading, although in the orthogonal direction. The results of these experiments are consistent with the ones obtained by Ellyin et al. [29], although performed with a somewhat different kind of material and at larger deformations applied by the clamp movement.

This analysis showed that it is in general necessary to use enriched formulations when trying to effectively describe mechanical behavior of complex materials, such as rubber, especially when dealing with a combination of complex loading and high levels of deformation. Also, this effect can be highly enhanced by other factors, such as complex geometries and combination of different elastomers, meaning that in order to describe deformation behavior of rubber tires and other complex objects made of this kind of material, a great attention should be paid on the choice of the model used, trying to never exclude phenomena that can occur, such as stress relaxation or time-dependent phenomena; however, complex models are often difficult to handle because of the possible combined influence of the different parameters on a particular aspect of the mechanical behavior of such materials.

Test	Rubber	$\max(\sigma_x)$	$\max(\sigma_y)$
Path 1	A	1.94 MPa	2.12 MPa
	B	0.81 MPa	1.03 MPa
	C	1.46 MPa	1.68 MPa
	E	2.47 MPa	2.77 MPa
	F	1.28 MPa	1.37 MPa
Path 2	A	2.28 MPa	2.29 MPa
	B	0.92 MPa	0.95 MPa
	C	1.71 MPa	1.68 MPa
	E	2.49 MPa	2.55 MPa
	F	1.33 MPa	1.30 MPa
Path 3	A	2.26 MPa	2.20 MPa
	B	0.81 MPa	0.87 MPa
	C	1.67 MPa	1.69 MPa
	E	2.47 MPa	2.55 MPa
	F	1.31 MPa	1.30 MPa

Table 4: Results of the different path tests in terms of difference in nominal stresses along the two directions.

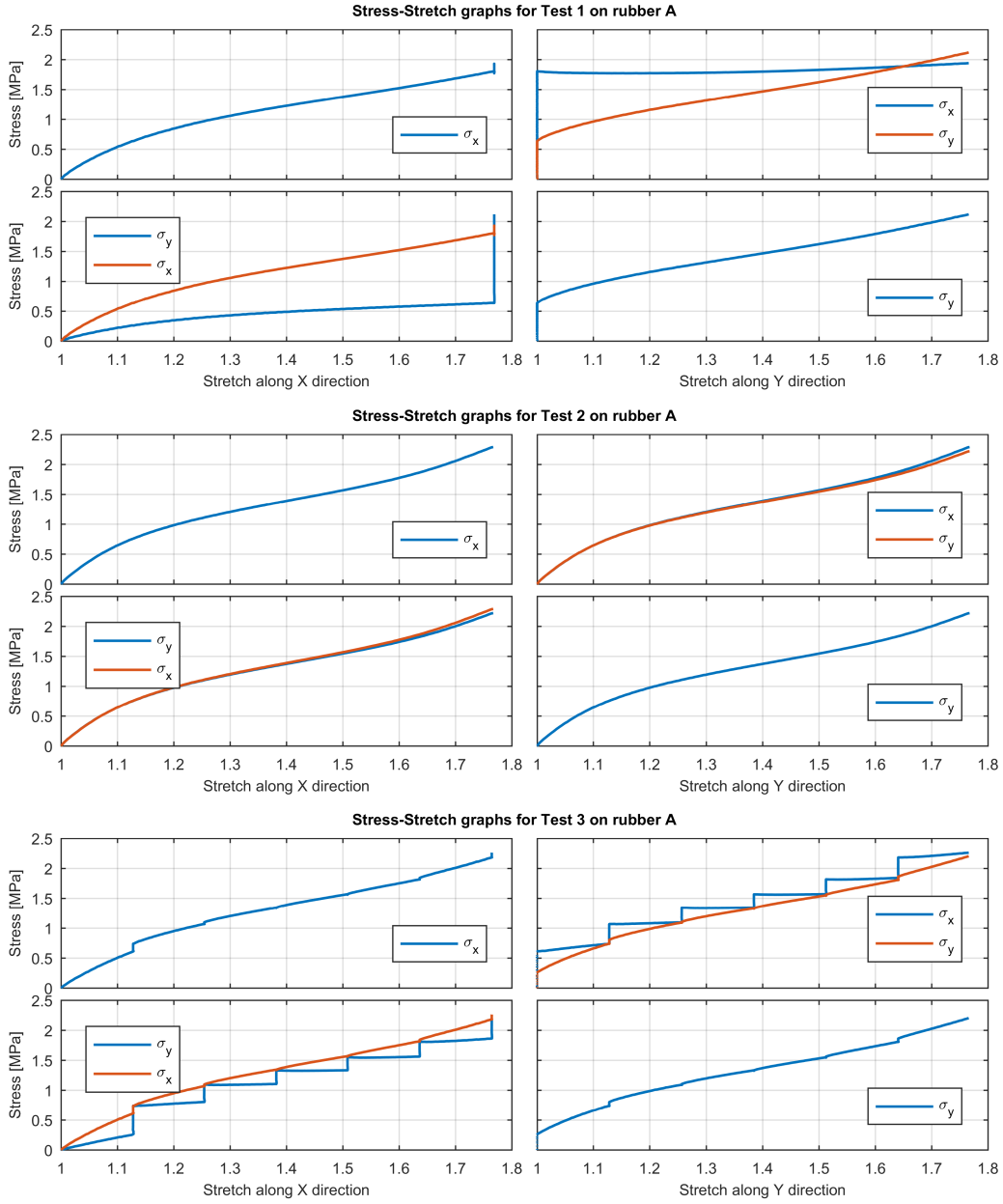

Figure 22: Results following the different paths for rubber A.

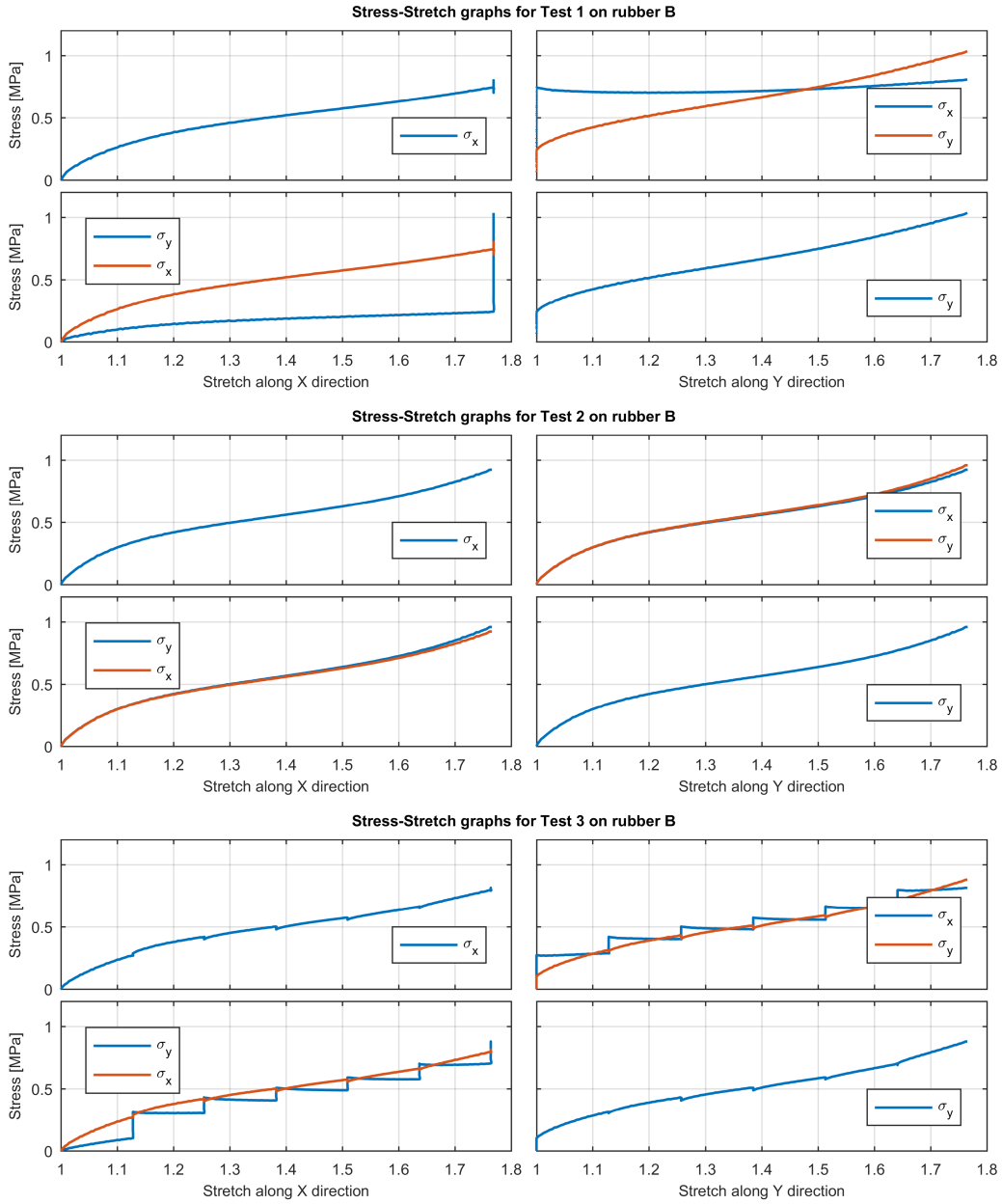

Figure 23: Results following the different paths for rubber B.

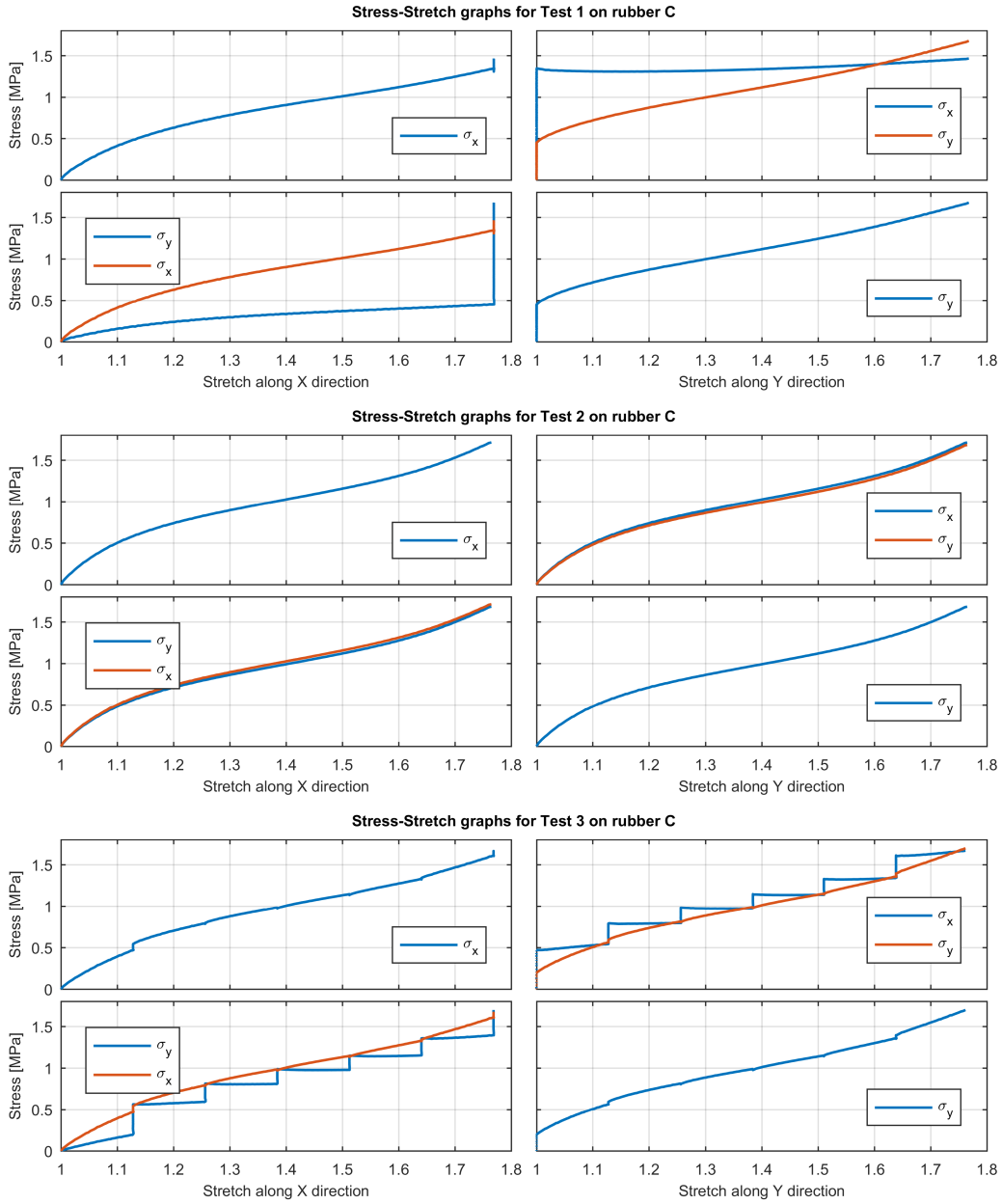

Figure 24: Results following the different paths for rubber C.

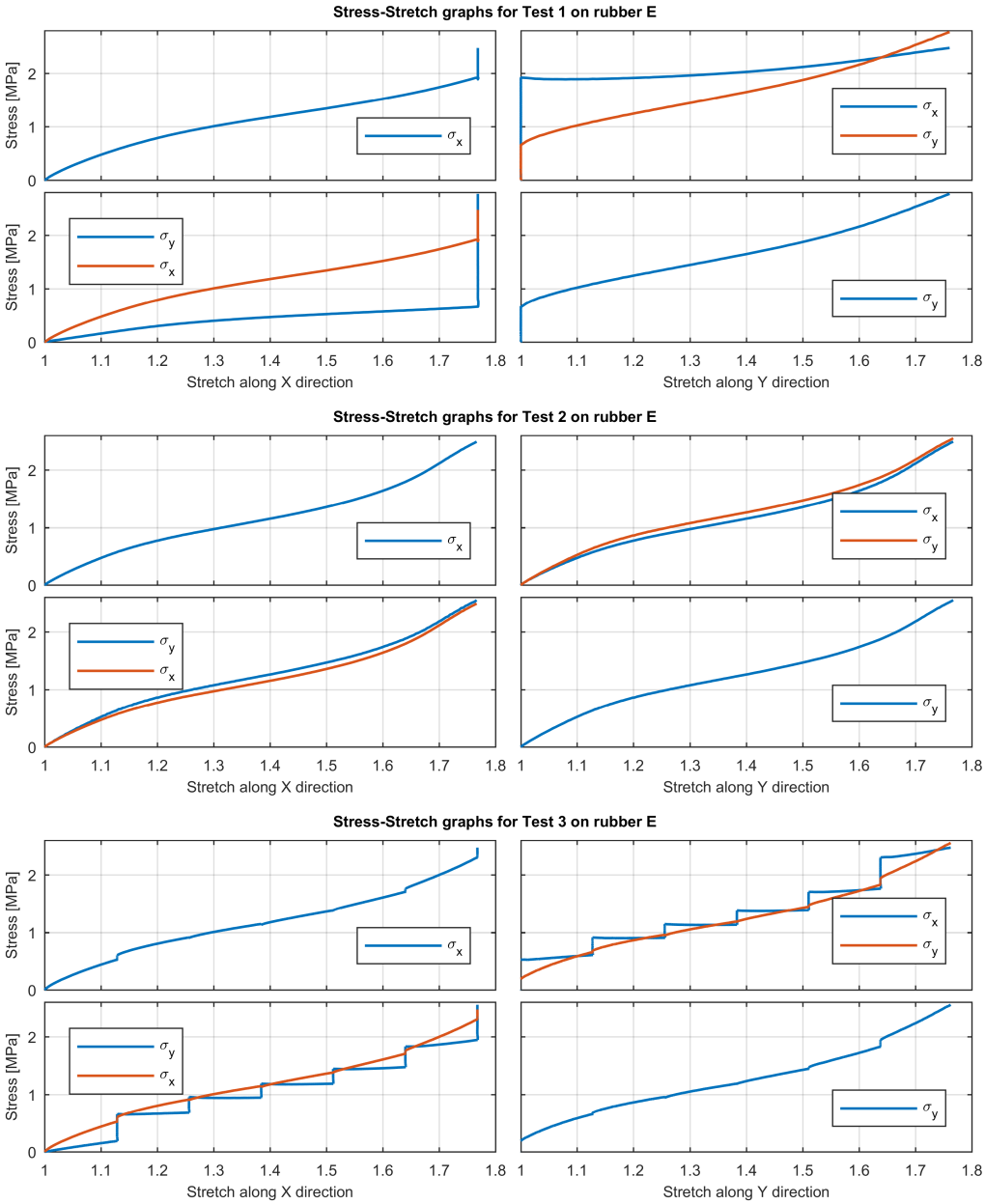

Figure 25: Results following the different paths for rubber E.

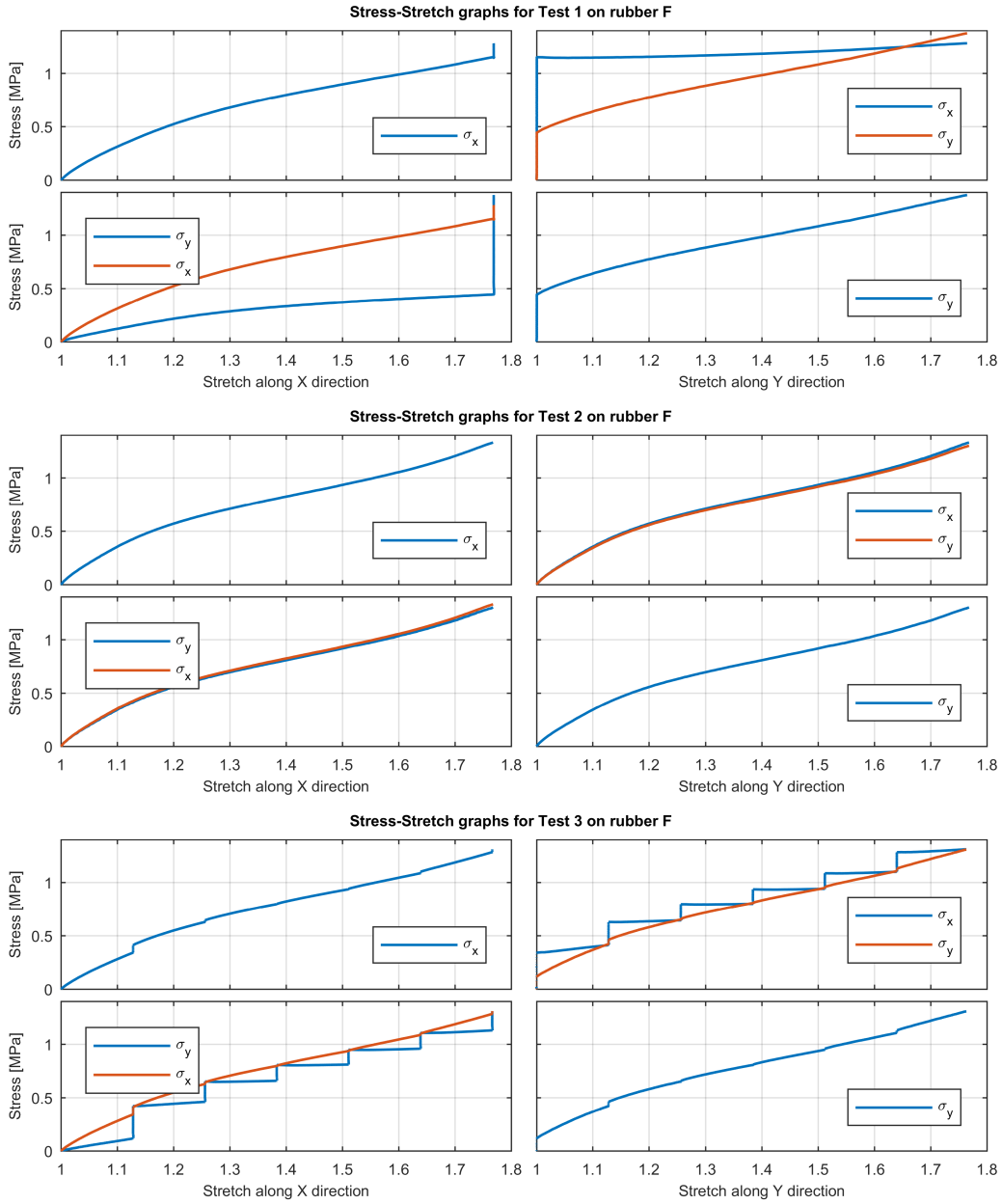

Figure 26: Results following the different paths for rubber F.

3

THE MULLINS EFFECT: MATHEMATICAL MODELING OF STRESS SOFTENING, HYSTERESIS AND PERMANENT SET IN FILLED RUBBER

3.1 INTRODUCTION

Elastomers for application in the automotive and structural field are generally filled with different amounts of reinforcement particles. These particles, called 'fillers', offer a great enhancement in terms of mechanical properties for rubber. For example, while at ambient temperature the elastic modulus of unfilled elastomers is of about 3 MPa, standard aggregates may increase the elastic modulus of also more than ten times.

However, inclusion of reinforcement generally leads also to the increase of different other dissipative effects, such as viscoelastic moduli and stress softening phenomena. Many authors tried to describe the phenomenology connected to the addition of reinforcement in elastomer ic networks, proposing for example models based on chain locking and slippage over the particle aggregates, such as Houwink [53], or more complex models based on the presence of different polymeric phases in the elastomeric matrix that interact in a different way with the particle aggregates, as in the work from Fukahori [38], but up to now no theory has been generally acknowledged as better than others, also because of the difficulties connected to experimentally analyze the interaction among polymer chains and aggregates.

Cyclic loading and unloading of filled rubber samples show, in fact, many different dissipative phenomena, such as stress softening upon reloading, hysteresis and residual strain. The stress softening, commonly referred as Mullins effect due to the his pioneering studies on the phenomenon [84]. This kind of effect is basically a change in material stiffness upon the first elongational deformation of the rubber sample. As can also be seen in Figure 27, this effect seems to be directly dependent on the maximum strain achieved, and in fact the material returns to the original stress-strain behavior if stretched more than before in its loading history. The tress softening effect is generally connected to the amount of filler in the elastomer, and is usually considered to be negligible for unfilled elastomers [24], and depends directly on the amount and on the size of the aggregates used to enhance the mechanical properties of filled rubber. Moreover, for a certain amount of cycles (generally 10-20) the stress reduction at a given strain on each successive cannot be considered as negligible, especially between the first and second cycle, while afterwards the loading-unloading cycles can be considered stable until other phenomena, such as fatigue effects, incur through micro-crack nucleation and growth (but generally such phenomena happen at more than 10^4 cycles [80]).

As already anticipated, residual strain and hysteresis are intrinsically connected to Mullins effect, because all those three phenomena arise only in filled rubber, and again directly depend on the amount of filler. Both effects appear in the same way as stress softening effect: in fact, they can be considered stable at the same time and are generally not seen in unfilled rubber; however, this kind of hysteresis seem to be independent from the displacement rate of the test itself, as shown in 28.

The stress softening seems to be generally connected to a change in the polymer chain configuration with respect to the filler particles, as many authors (as reported in [24]) underlined during the years with different physical explanation of the phenomenon. For example, Blanchard and Parkinson [11] explained the Mullins effect through the use of the concept of bond ruptures. By considering that the pre-strain induces the rupture of the weaker bonds (physical bonds) at

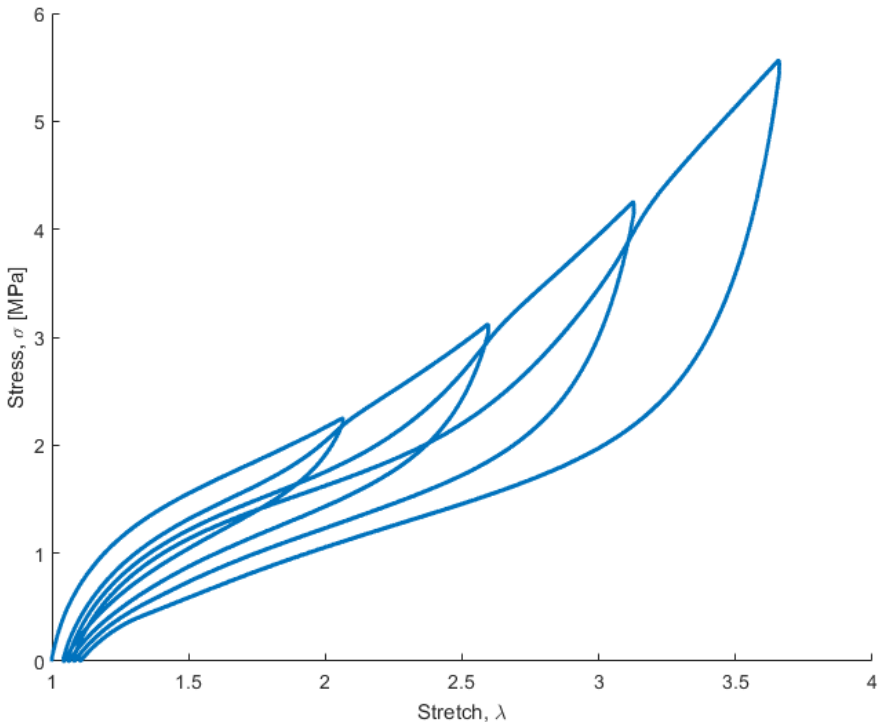

Figure 27: Experimental data.

the rubber–particle interface, they assumed that further pre-strain could break the stronger bonds (chemical bonds). This idea has been used as a base to develop some kind of physical interpretation of the phenomenon also by Bueche [14], which also interpreted the Mullins softening as rupture of the stronger bonds within chains linking two particles, by considering the particles as rigid and by applying an affine displacement between the centers of the particles, thus concentrating high levels of strain on the molecular chain itself. This explanation justified also the absence of this phenomenon in unfilled rubbers by considering that, in the case of a molecular network, shorter chains are not subjected to over-stretch because of the different arrangement of the junctions between the chains.

Filled elastomers, however, show also another interesting behavior: in fact,

under certain conditions, healing has been observed through the recovery of the permanent set or the return to initial values of the stress at fixed strain or of the complete stress–strain response. Mullins [83] studied the stress recovery of a filled natural rubber previously stretched up to 420%. For that, after various recovery periods, he measured the stress at an elongation of 200% and compared it to the stress measured on the material stretched to the same elongation for the first time (virgin material), showing a temperature-dependence of the recovery. At high temperatures, Harwood and Payne [45] studied the stress-recovery in unfilled natural rubber depending of the type of crosslinking,showing that the recovery depends on the type of crosslinking and may be almost complete for monosulfide crosslinked and carbon to carbon crosslinked vulcanizates. Therefore, the physical phenomena taking place during the Mullins softening can be recovered with a high temperature or a solvent exposure. In usual conditions at room temperature, this healing can be neglected and the Mullins effect can be considered as a damaging process, which is how it is introduced in the phenomenological models. However, the physical explanation proposed by Bueche [14] does not take into account for any recovery, because of its irreversible nature, so it is not considered anymore as a reasonable explanation for the Mullins effect.

One of the most interesting approaches able to justify these experimental observations seems to be the one given by Houwink [53], which connects the Mullins effect to a relative slipping of molecules on the filler surface during the first extension. After slippage, the new bonds would be of the same physical nature as the original ones, but would appear at different places along the rubber molecules. This causes a configuration change and a lower mechanical response up to the maximum stretch approached previously by the elastomer, changing also the material entropy, which could be restored by a temperature increase. This approach has also been validated by Clément et al. [20] through observations via atomic force microscopy during uniaxial tension tests on silica-filled PDMS, showing also that a higher degree of stress softening is observed in materials containing a non-homogeneous distribution of silica, because of larger local strains in regions with high silica concentrations.

Vacuole formation has been another theory behind the stress softening, but different authors through the years discredited it for two main reasons: on one side, in fact, the generation of vacuoles during prestretch should automatically generate a substantial increase in volume during prestretch while on the other side this effect would be practically irreversible. Kraus et al. [67] and Dannenberg et al. [23] carried out some swelling tests to ascertain the extent of bond rupture in pre-stretched filled rubbers, and both groups measured a rather small change in the network density compared to the relatively large stress softening observed. The amount of bond ruptures at the rubber–particle interface, in fact, seemed moderate and could not lead to the generation of a non negligible amount of vacuoles in the network, thus being the main source of the Mullins softening.
Lately, instead, the theory given by Klüppel and Schramm [64] seems to be the most interesting under various points of view, regarding both mechanical behavior, volume constancy and the possibility to recover from previous softening. The authors proposed to attribute the main source of the stress-softening to the rupture of carbon-black structure, especially for highly reinforced materials. Moreover, this theory is difficult to extend to the case of unfilled crystallizing rubbers.
This kind of approach would explain in a straightforward way the behavior of rubber filled with carbon black and the rubber recovery at high temperatures, shown by Mullins (1948), Laraba-Abbes et al. (2003), Harwood and Payne (1966), but is not easily applicable for rubber filled by silica, due to the strong chemical bonding between this kind of aggregate and the molecular chains: in fact, while in rubber filled with carbon black the filler-polymer interactions can be attributed to physical bonding (*i.e.* Van der Waals interactions), the bondings between silica particles and elastomer macromolecules are generally stronger bonds. This phenomenon can dramatically influence crack propagation behavior of filled elastomers, mainly because, while advancing in the material, the crack influences the strain state of the neighboring region by softening it. Other dissipative phenomena, as for example the rubber viscoelasticity, can actually influence the

crack propagation behavior in different ways, generating hysteresis and relaxation.

3.2 MATHEMATICAL FORMULATION

3.2.1 *The framework of pseudoelasticity*

Let us consider a body $\mathcal{B}$ occupying a certain portion of space, Ω, with $\mathbf{X}$ defining the position vectors of each material point. After the deformation the body will occupy the region Ω_d, while the material point is deformed to the position $\mathbf{x}$. The deformation gradient $\mathbf{F}$ is then defined as

$$\mathbf{F} = \frac{\partial \mathbf{x}}{\partial \mathbf{X}} \tag{65}$$

Following the approach adopted by [92] and [27], let us consider that the response of the aforementioned body is defined through an energy density function $W = W(\mathbf{F}, \eta_1, \eta_2)$ which depends not only on the deformation gradient $\mathbf{F}$, but also on a certain number of internal variables, η_i.
The nominal stress, here taken as first Piola-Kirchhoff stress tensor, $\mathbf{P}$, is then defined as

$$\mathbf{P} = \frac{\partial W}{\partial \mathbf{F}}(F, \eta_1, \eta_2) \tag{66}$$

for a compressible material, and as

$$\mathbf{P} = \frac{\partial W}{\partial \mathbf{F}}(F, \eta_1, \eta_2) - p\mathbf{F}^{-\mathbf{1}} \tag{67}$$

for an incompressible material. Here, p is the hydrostatic pressure and works as a Lagrange multiplier, and ensures incompressibility. Moreover, Cauchy stress σ can be connected to $\mathbf{P}$ through the Piola transformation, giving respectively

$$\sigma = \mathbf{F}\frac{\partial W}{\partial \mathbf{F}}(F, \eta_1, \eta_2) \tag{68}$$

$$\boldsymbol{\text{œ}} = \mathbf{F}\frac{\partial W}{\partial \mathbf{F}}(F, \eta_1, \eta_2) - p\mathbf{I} \tag{69}$$

for a compressible and incompressible body.
In the context of pseudoelasticity, as previously stated by [70], the internal variables η_i are not necessarily required to be continuous, while the energy function W, which we will refer to as pseudo-energy function throughout the paper, is required to comply with the condition of objectivity, i.e. it cannot be affected by superimposed rigid body translations or rotations.
In the previously named context, other than the equilibrium equation

$$\nabla_{\mathbf{X}} \cdot \mathbf{P} = \mathbf{0}, \quad \forall\, \mathbf{X} \in \Omega \tag{70}$$

where the operator $\nabla_{\mathbf{X}}$ defines the two different conditions must be satisfied at the equilibrium and in absence of body forces throughout the space region occupied by the body

$$\frac{\partial W}{\partial \eta_1}(\mathbf{F}, \eta_1, \eta_2) = 0, \quad \frac{\partial W}{\partial \eta_2}(\mathbf{F}, \eta_1, \eta_2) = 0 \tag{71}$$

These equations come directly from the application of the calculus of variations on the energy functional, in order to allow smooth solutions for $\mathbf{F}$ and $\mathbf{x}$, while leaving the possibility for η_1 and η_2 to be non-smooth through the space region Ω, e.g. allowing η_1 and η_2 to undergo discontinuities or even to jump, as also seen in [70].

3.2.2 *The pseudo-energy function*

The framework described before allows for a wide range of models to be used. For example, by sticking to the work of Dorfmann and Ogden [27], it is possible to choose a pseudo-energy function of the form

$$W(\mathbf{F}, \eta_1, \eta_2) = \eta_1 W_0(\mathbf{F}) + (1 - \eta_2) N(\mathbf{F}) + \phi(\eta_1, \eta_2) \tag{72}$$

Here, W_0 represents a suitable strain energy density able to correctly describe the mechanical behavior of the material on the virgin loadings (i.e. any loading higher than the maximum loading ever experienced by the material), N_0 is another suitable function, introduced to better describe the residual strain on the material upon unloading, while η_1 and η_2 are the aforementioned *internal variables*. The function $\phi(\eta_1, \eta_2)$, instead, is generally called *dissipation function*, and is directly connected to the amount of energy dissipated by the body while loading and unloading. Moreover, the combination of the pseudo-energy function (72), together with the condition (71), gives some restrictions on the shape that the internal variables can assume: on this point of view, the *dissipation function* itself gives the direct restrictions.

In order to separate the contributions of stress softening and residual strain, it is generally considered that the dissipation function $\phi(\eta_1, \eta_2)$ can be additively decomposed in the two dissipation functions $\phi_1(\eta_1)$ and $\phi_2(\eta_2)$. In order to keep into account that the material properties can change after loading of the material up to a certain degree, the variables η_1 and η_2 are needed to be able to switch between active or inactive, under certain conditions: the objective is, in fact, that these variables are *active* when the deformation in the material is lower than the one previously attained, and *inactive*, or equal to 1, when the material undergoes deformation states higher than before. This change may, for example, be induced when unloading is initiated. During virgin (or primary) loading η_1 and η_2 are inactive and are set to be equal to one, which in the primary loading translates as

$$W_0(\mathbf{F}) = W(\mathbf{F}, 1, 1) \tag{73}$$

From this point onward, every term with subscript 0 will be referred to conditions in which the variables η_1 and η_2 are inactive.

When η_1 and η_2 are active, instead, we can suppose that equations 71 can be solved in order to get the shape of the two internal variables in terms of the components

of the deformation gradient $\mathbf{F}$.
By considering an isotropic response of the material, it is possible to assume that

$$W(\mathbf{F}, \eta_1, \eta_2) = W(\lambda_1, \lambda_2, \lambda_3, \eta_1, \eta_2) \tag{74}$$

Equation 74, allows us to write equation 71 in a different form:

$$\frac{\partial W}{\partial \eta_1}(\lambda_1, \lambda_2, \lambda_3, \eta_1, \eta_2) = \mathbf{0}, \quad \frac{\partial W}{\partial \eta_2}(\lambda_1, \lambda_2, \lambda_3, \eta_1, \eta_2) = \mathbf{0} \tag{75}$$

where it is by assuming that it is possible to explicitly express the dependency of η_1 and η_2 upon the principal stretches as

$$\eta_1 = \eta_1(\lambda_i, \lambda_j, \lambda_k) \quad \eta_2 = \eta_2(\lambda_i, \lambda_j, \lambda_k) \quad \{i, j, k\} = \{1, 2, 3\} \tag{76}$$

As in equation 73 we indicated with the subscript 0 every condition in which η_1 and η_2 are inactive, we will indicate as $w(\lambda_1, \lambda_2, \lambda_3)$ any energy function with active η_1 and η_2:

$$w(\lambda_1, \lambda_2, \lambda_3) = W(\lambda_1, \lambda_2, \lambda_3, \eta_1(\lambda_1, \lambda_2, \lambda_3), \eta_2(\lambda_1, \lambda_2, \lambda_3)) \tag{77}$$

As previously introduced, whether or not the internal variables are active, the principal Cauchy stresses for an incompressible media are given by

$$\sigma_i = \lambda_i \frac{\partial W}{\partial \lambda_i} - p, \quad i \in \{1, 2, 3\} \tag{78}$$

By considering the isotropy constraint, the equilibrium condition on the internal variables in equation 71 and upon differentiation of equation 72 with respect to both η_1 and η_2, we obtain the two conditions

$$\begin{aligned} W_0(\lambda_1, \lambda_2, \lambda_3) + \frac{\phi(\eta_1, \eta_2)}{\eta_1} &= 0 \\ N(\lambda_1, \lambda_2, \lambda_3) + \frac{\phi(\eta_1, \eta_2)}{\eta_2} &= 0 \end{aligned} \tag{79}$$

By taking into account incompressibility of the media and the possibility to completely determine the in-plane principal stretches (i.e. by defining a certain loading condition, as defined in chapter 1), it is possible to reduce the dependence of the pseudo-energy function to only one of the stretches. By considering, for example, uniaxial tension as loading condition and incompressibility of the medium, it is possible to write

$$\hat{W}(\lambda, \eta_1, \eta_2) = W(\lambda, \frac{1}{\sqrt{\lambda}}, \frac{1}{\sqrt{\lambda}}, \eta_1, \eta 2) \tag{80}$$

where the circumflex symbol ˆ indicates that a certain loading condition has been identified and that it is possible to find a combination between the three principal stretches.

As we anticipated before, in order to separate the contributions of stress softening and residual strain, the dissipation function $\phi(\eta_1, \eta_2)$ can be additively decomposed in $\phi_1(\eta_1) + \phi_2(\eta_2)$. Inserting this in Equation 79 we obtain:

$$\begin{aligned} W_0(\lambda_1, \lambda_2, \lambda_3) + \phi_1'(\eta_1) = 0 \\ -N(\lambda_1, \lambda_2, \lambda_3) + \phi_2'(\eta_2) = 0 \end{aligned} \tag{81}$$

Together with the identification of a certain loading condition and by including incompressibility, further differentiation of the equations in 81 with respect to λ will then give

$$\begin{aligned} \frac{\partial \hat{W}_0}{\partial \lambda} = -\frac{\partial \eta_1}{\partial \lambda} \phi_1''(\eta_1) \\ \frac{\partial \hat{N}}{\partial \lambda} = -\frac{\partial \eta_2}{\partial \lambda} \phi_2''(\eta_2) \end{aligned} \tag{82}$$

Following the approach of Ogden and Roxburgh [92], it is now necessary to choose the analytical form of the damage function ϕ_1 and ϕ_2, which are subject to the following constraints:

$$\begin{aligned} \phi_1(1) &= 0 & \phi_2(1) &= 0 \\ -\phi_1'(1) &= W_0(\lambda_1, \lambda_2) & \phi_2'(1) &= N(\lambda_1, \lambda_2) \\ \phi_1''(\eta_1) &< 0 & \phi_2''(\eta_2) &< 0 \end{aligned} \tag{83}$$

Equations in 83 respectively come from the equation 73, equations 81 and from the definition of stress softening itself, after some considerations on equations 82. It is important to remember that, as the aim is to model the stress softening in filled rubber (together with other different phenomena, such as hysteresis and permanent set), it is appropriate to let η_1 and η_2 vary in the range $(0, 1]$.

3.2.3 *The damage functions*

Let us consider a certain strain state, identified by the first two principal stretches as equal to λ_{1m} and λ_{2m}; by considering incompressibility we can define the third principal stretch as equal to $(\lambda_{1m}\lambda_{2m})^{-1}$. As in the work from Dorfmann and Ogden [27], we choose the function ϕ_1 so that its derivative is

$$-\phi_1'(\eta_1) = \mu\, m\, tanh^{-1}\left[r\,(\eta_1 - 1)\right] + W_m \tag{84}$$

where W_m is the pseudo-energy function associated with the strain state identified by the three principal stretches $\left\{\lambda_{1m}, \lambda_{2m}, (\lambda_{1m}\lambda_{2m})^{-1}\right\}$. Moreover, this particular strain state is chosen to be the one corresponding to the strain state at which unloading started from a primary loading curve; for the whole unloading phase,

the value of $_m$. By inserting the suggested function for ϕ_1' into the first equation of 81, we obtain the analytical expression for η_1

$$\eta_1 = 1 - \frac{1}{r} tanh\left(\frac{W_m - \hat{W}_0(\lambda)}{\mu m}\right) \tag{85}$$

As reported in the work from Dorfmann and Ogden [27] the second internal variable η_2 can be defined as

$$\eta_2 = tanh\left[\left(\frac{\hat{W}_0(\lambda)}{W_m}\right)^{\alpha(W_m)}\right] \cdot tanh^{-1}(1) \tag{86}$$

where $\alpha(W_m)$ is generally defined as a function dependent on W_m, generally defined as $\alpha(W_m) = a + b\, W_m$.
These two internal variables are needed to model the mechanical behavior of filled rubber under cyclic loading, with the objective of effectively describe mechanical behavior in terms of stress softening and permanent set. However, the use of variables as defined up to now is not enough in order to better describe also other phenomena connected to the Mullins effect, such as hysteresis. Consequently, a different form of the internal variables must be used in order to better describe material behavior.

3.2.4 *Rubber hysteresis - Differences between loading and unloading*

As previously seen, cyclic loading of rubber generates at first a softening of the material itself, leading to a stabilization of the mechanical properties after a certain amount of cycles. However, this stabilized behavior generally comes with hysteresis in the loading cycles. This hysteresis seems to be dependent upon the strain rate starting from a certain level of strain, while seems to be completely independent from it for lower values of strain rate, i.e. for low enough values of strain rates,

the loading-unloading cycles remain constant regardless of the imposed strain rate. This effect can also be seen in figure 28, where a sample of where the results from cyclic tests at slow speed of an SBR sample filled with 50 phr of carbon black are shown: four different samples have been subjected to loading-unloading cycles with transverse speeds of 50, 30, 15 and 7.5 mm/min, each for 25 cycles. The results show basically no dependence of the strain rate on the hysteresis and residual strain.

In order to model this behavior, it is not possible to use the same internal variables

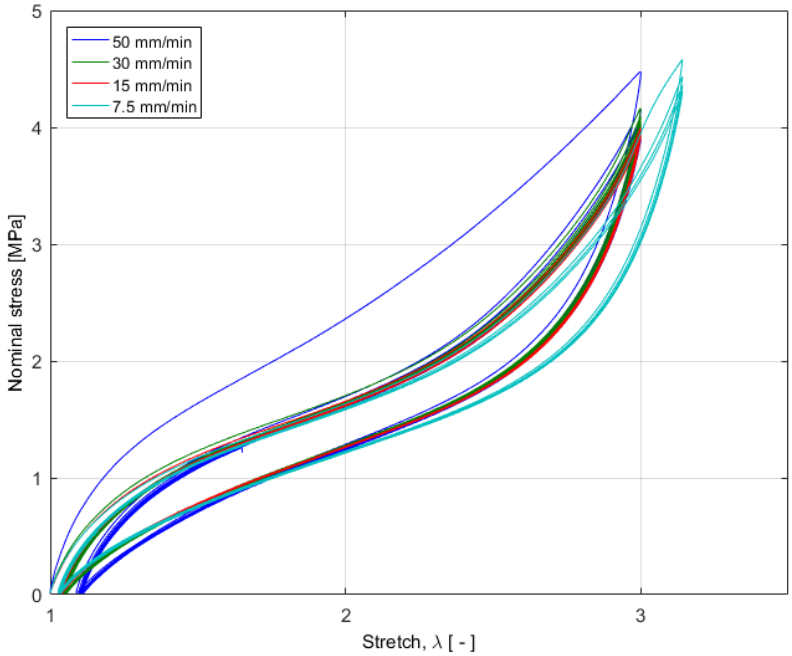

Figure 28: Pure shear loading tests on Butadiene Rubber with 50 phr of carbon black. The different colors show tests performed at different strain rates; it is evident how the hysteresis cycle remains basically constant regardless f the different strain rates.

as previously defined. However, it is convenient to modify η_1 in order to take into account also this ind of effect. In particular, by defining η_1 as follows, it is possible

to widen the range of phenomena taken into account by this internal variable. In particular, it is possible to choose η_1 as

$$\eta_1 = 1 - \frac{1}{r}\tanh\left[\frac{W_m - \tilde{W}_0(\lambda)}{\mu[m + c\, f(\lambda, \lambda_m, \lambda_{INV})]}\right] \tag{87}$$

where c is a parameter, while $f(\lambda, \lambda_m, \lambda_{INV})$ is a suitable function depending on the actual stretch, the maximum stretch achieved during loading and the minimum stretch of the actual loading phase to which the material is subjected. In our particular case, the function has been chosen to be

$$f(\lambda, \lambda_m, \lambda_{INV}) = (\lambda - \lambda_{INV})(\lambda - \lambda_m) \tag{88}$$

where λ_{INV} is the minimum stretch reached in the last monotonic loading portion of the loading history.

3.3 APPLICATION OF THE MODEL

Combination of the pseudo-energy function to represent loading and unloading in equation 72 and of equation 66, together with the consideration that it is possible to exclude from such model gives the first Piola-Kirchhoff tensor component in a generic loading condition as

$$P_{11} = \eta_1 \hat{W}_0'(\lambda) + (1 - \eta_2)\hat{N}'(\lambda) \tag{89}$$

As stated in equation 73, when rubber is loaded on a primary loading curve the internal variables are inactive; in this case it is possible to define the quantity in equation 89 as

$$P_{11} = \hat{W}_0'(\lambda) \tag{90}$$

In order to model material response during primary loading, the extended tube model from Kaliske and Heinrich [60] has been chosen. This model, based on a

physically-motivated framework, treats polymeric chains as constrained to remain in a tube formed by the surrounding chains. It takes into account may aspects, such as limited chain extensibility and entanglement density, through the use of a non-Gaussian distribution for the chain length, and some aspects of percolation theory to properly define the constraints to which polymeric chains are subjected. The potential assumes the form

$$W(\lambda_1,\lambda_2,\lambda_3) = \frac{G_c}{2}\left[\frac{\left(1-\delta^2\right)\left(I_1-3\right)}{1-\delta^2\left(I_1-3\right)} + ln\left(1-\delta^2\left(I_1-3\right)\right)\right] + 2\frac{G_e}{\beta^2}\sum_{A=1}^{3}\left(\lambda_A^{-\beta}-1\right) \quad (91)$$

In this hyperelastic model, the parameters are G_c, G_e, δ and β, while I_1 represents the first invariant of the right Cauchy–Green deformation tensor, $\mathbf{C}$. This model has been acknowledged as one of the best hyperelastic models in terms of number of parameters and for its ability to physically give meanings to the different parameters, as can be seen in the work of Marckmann and Verron [77]. The response connected to residual strain behavior is instead described by means of a modified Neo-Hookean model

$$N(\lambda_1,\lambda_2,\lambda_3) = \frac{1}{2}\left[\nu_1\left(\lambda_1^2-1\right)+\nu_2\left(\lambda_2^2-1\right)+\nu_3\left(\lambda_3^2-1\right)\right] \quad (92)$$

When unloading is initiated from any point on the primary loading path, the variables η_1 and η_2 become active and the energy function, together with the stress, changes continuously. However, $f(\lambda,\lambda_m,\lambda_{INV})$, as defined in equation 88 is equal to 0 in both those cases, because in the primary loading curve $\lambda = \lambda_m$ and in the unloading curve $\lambda = \lambda_{INV}$. During reloading, however, this part of the internal variable η_1 activates, and thus describes the hysteretic behavior to the material.
In order to test the efficiency of the model, pure shear loading-unloading tests on Butadiene rubber have been chosen. This rubber, filled with 50 phr of carbon black, was not prestretched and was tested 24 hours after the vulcanization process. In order to fit all the parameters of the model, available in table 5, three different steps were needed: at first, the parameters of the hyperelastic model have been obtained through fitting of a material stretched up to failure in uniaxial and pure shear loading condition; afterwards, a fitting for the other parameters (except for

the reloading parameter c) through nonlinear least squares data fitting on an unloading curve. After this, a third fitting procedure gave the last parameter for the model. The results are shown in table 5 and in figure 29.

The results show good agreement between the experimental and the modeled

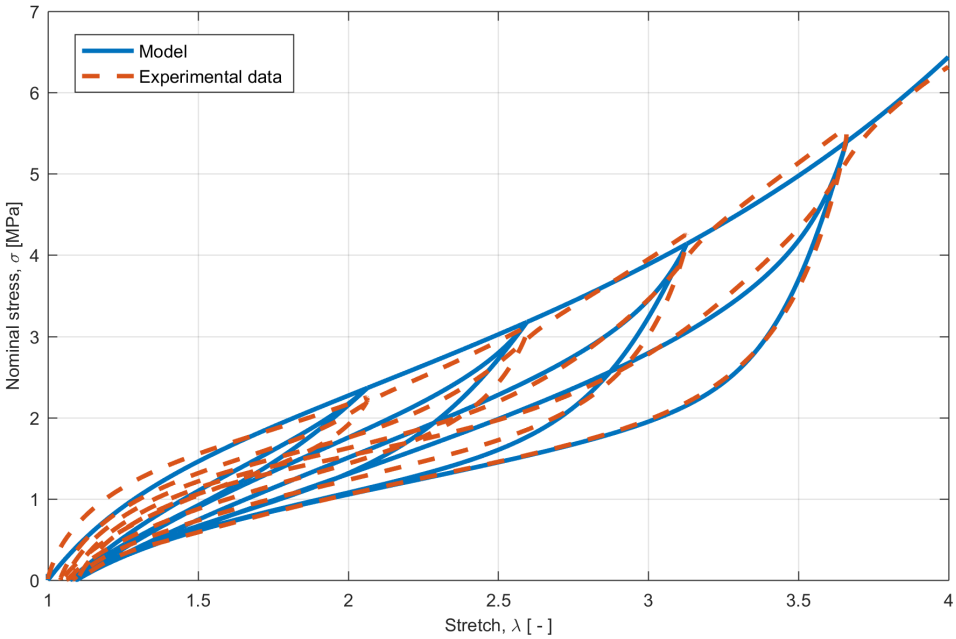

Figure 29: Comparison of the experimental stress-strain curve of Butadiene rubber filled with 50 phr of carbon black with the response obtained through the Ogden-based model.

data, on both unloading and reloading. However, it is important to note that cyclic loading introduces an anisotropy in the material. Up to now, this is not taken into account in this model, and if the material is then subsequently loaded to a different stretch in another direction, the material will respond as if it was isotropic. This aspect, taken into account for example in the works of Rebouah et al. [101, 102], where a model based on anisotropization of the model proposed by Göktepe and Miehe [43] has been extended to anisotropic behavior by using the discretization in 42 spatial directions proposed by Bažant and Oh [8].

Parameter	Value
G_c	0.9403 MPa
G_e	0.3125 MPa
β	-0.0024
δ	0.1255
ν_1	$1.739 \cdot 10^{-5}$
ν_2	0.2408
ν_3	0.25
a	1.5666
b	1.8917
m	0.8738
r	19.624
c	59.701

Table 5: Parameters fitted in order to obtain the stress-strain response in figure 29.

4

FATIGUE TESTING OF ELASTOMERS WITH THE BIAXTESTER

4.1 INTRODUCTION ON FATIGUE TESTING ON ELASTOMERS

As stated in Chapter 1, withstanding very large strains without permanent deformation or fracture is what makes rubber one of the best suited materials for applications that involve abrasion, dampening or severe regimes of deformation, such as tires, vibration isolators, seals, belts, medical devices, footwear and many others. However, all of these application share a common need that can be translated in long term durability of the material itself. In this framework, aspects such as mechanical fatigue and crack growth in filled elastomers is a crucial point of the behavioral analysis of these materials. In order to find a solution for this issue, a great effort has been made in the recent years from both the industrial and the academic point of view, in order to identify the principal phenomena occurring in elastomers during fatigue and describe in some way the connection between physical parameters obtained from material testing and the effective behavior of materials under complex loading conditions in real situations.

Generally, fatigue failure processes involve two distinct phases, respectively characterized by a time frame in which cracks nucleate in regions that were initially free of macroscopic cracks and another, successive phase in which the nucleated cracks grow to the point of failure. In order to characterize this kind of behavior, different models for the prediction of fatigue life of elastomers have been developed

through two different approaches: one os based on the prediction of crack nucleation life, through the history of quantities that are defined at a material point, such as stress and strain; the second, instead, is based on fracture mechanics and focuses on predictions regarding growth of a particular crack, given its initial geometry and energy release rate history.

Of the two mentioned approaches, crack growth analysis is mostly based on the second. It explicitly considers preexisting cracks or flaws and is based on the study of the advancement of such cracks while subjecting the material to a certain loading. Griffith [41], one of the pioneers in this field, proposed a fracture criterion based on an energy balance including both the mechanical energy of a cracked body, and the energy associated with the crack surfaces. His approach was later developed in the field of crack growth in metals by Irwin [57] and Rice [106]. Originally, the approach used with rubber was based on the prediction of static strength needed to let the crack propagate, as seen in the works of Rivlin and Tomas [109], and in many other works, such as the one of Lindley [95] and the one of Lake and Yeoh [69], but in the late 1950s Thomas [124] extended this approach to analyze crack growth under cyclic loading. In particular, he found a square-law relationship between peak energy release rate and crack growth rate for unfilled natural rubber.

The hypothesis of Griffith about crack growth was that the advancement was due to the conversion of a structure's stored potential energy to surface energy associated with new crack surfaces. In the case of glass, he also showed that the surface energy associated with the crack faces of a broken glass filament was equal to the elastic energy released by the fracture. In the framework of crack propagation in rubbers, however, the energy released from the surrounding material is spent on both reversible and irreversible processes to create the new surfaces [5,25,80]. In any case, the energy release rate is considered to be the change in the stored mechanical energy dU, per unit change in crack surface area dA. This quantity, defined as *tearing energy* is generally associated with the symbol T, and is defined as

$$T = -\frac{dU}{dA} \tag{93}$$

Initially, calculation of the tearing energy was applied only in the analysis of rubber specimens under static loading [109], however Thomas [124] extended this approach also to crack growth under cyclic loading, finding that the maximum energy release rate achieved during a cycle determined the crack growth rate.
Three different samples (shown in Figure 30) are generally tested in order to obtain information about the crack propagation behavior of rubber:

- *single edge cut, simple tension specimens*; in this kind of sample, the energy release rate T depends on the gauge section strain energy density W, the size of the crack a, and a strain-dependent parameter k, experimentally defined by Lindley [95] as

$$T = 2\,k\,W\,a \qquad k = \frac{2.95 - 0.08\epsilon}{(1+\epsilon)^{1/2}} \tag{94}$$

- *single edge cut, planar tension specimen*; for this kind of specimen, similar in shape to the pure shear samples, the energy release rate T assumes a particularly simple form, dependent on the elastically stored energy density of the sample (W) and on the height of the unloaded sample, h

$$T = Wh \tag{95}$$

  However, some conditions should be respected in order to use it;

- *trouser specimens*; for this kind of sample, energy release rate T depends on the applied force F, the extension ratio l and strain energy density W in the "legs" of the specimen, the specimen thickness t, and the "leg" width b

$$T = \frac{2\,F\,\lambda}{t} - bW \tag{96}$$

However, few investigations of multiaxial fatigue of rubber are reported in the literature: some of the works about this topic are, for example, the works of Mars and Fatemi [129] [79] and and the work from Poisson et al. [98]. This is due

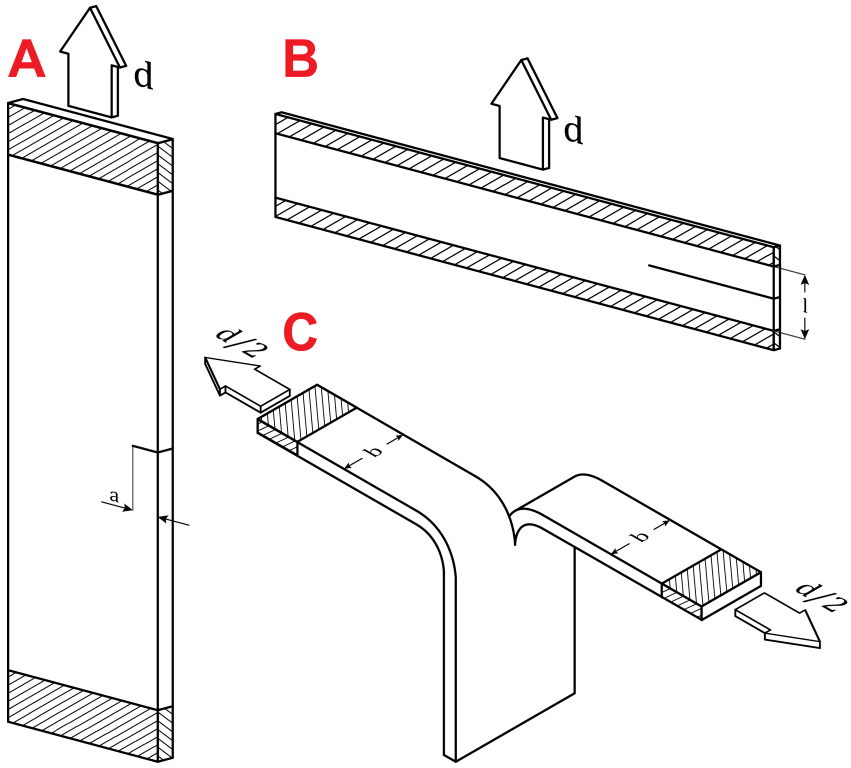

Figure 30: Standard samples used for crack propagation experiments and subjected to a cyclic displacement history ranging from 0 to d. A) single edge cut, simple tension specimen (a is the crack length); B) single edge cut, planar tension specimen, with l equal to the nominal height of the sample; C) trouser specimen, where each arm has a width equal to b.

to the difficulty of extending the commonly used criteria for the evaluation of the tearing energy in more complex loading conditions, such as biaxial loading. For this reason, this work will focus on the comparison of the results obtained through the use of standard single edge cut, planar tension specimens and the use of the Rivlin-Thomas [109] approach, and specifically of the calculation of the tearing energy as in equation 95, with the results obtained by using the same approach on BiaxTester specimens, in order to assess the capabilities of this mechanical tester on a kind of 'benchmark test' for this kind of experiments.

4.2 MATERIALS AND METHODS

In order to validate the Rivlin-Thomas approach on the BiaxTester samples, a comparison of the results obtained with different single edge notched, planar tension specimens have been chosen. In particular, two different types of pure shear specimens have been used, together with squared BiaxTester samples, as depicted in Figure 7 with an edge notch. The dimensions of such specimens are described in Table 6. The set-up and the specifications for the test of rubber specimens is described in tables 8 and 9. Calculation of crack growth over cycles for the different samples has been done using a custom-built MATLAB script, which evaluates the horizontal advancement of crack through the use of black-white images. Moreover, the calculation of the elastically stored energy in the sample has been performed by testing the same specimens as in the propagation analysis without notches, at the same displacement ranges of the different crack propagation tests, in order to exclude phenomena connected to different accuracy of multiple testing systems. Moreover, all the tests (the ones for the evaluation of crack propagation and the ones used to calculate the elastically stored energy) have been performed at 2 Hz. Regarding the elastically stored energy, it has been calculated by integrating the last unloading curve of a 100 cycles test, in order to both exclude stress softening phenomena and dissipated energy from the calculation, and dividing it by the total sample volume. The rubber used for this kind of analysis is instead described in table 7. Styrene-butadiene rubber has been chosen because of its low strain hardening effect and for the practically negligible strain induced crystallization, while the different amounts of carbon black can be used as a benchmark in order to compare

Testing machine	Width	Height	Thickness	Initial crack length
Instron	80 mm	10 mm	1.3 mm	20 mm
Instron	80 mm	4 mm	1.3 mm	20 mm
BiaxTester	77 mm	77 mm	1.9 mm	25 mm

Table 6: Rough dimensions of the tested specimens.

Rubber code	SBR	CB
JD	100	25
JE	100	50

Table 7: Materials used for the crack propagation experiments.

the obtained results with data available in literature. Moreover, in order use the Rivlin-Thomas approach on the different kinds of specimens, sample deformation fields need to comply with certain criteria, as defined by Rivlin [109].

If we consider a single edge cut, planar tension specimen as the one in Figure 30, it is possible to distinguish between different strain regions. In fact, as the sample is deformed in a direction transversal to the defined width of the sample, and this width is sufficiently large, the region at the left of the notch (region A) is substantially undeformed while the region on the other side of it (region B) is in a state of pure shear loading (defined by $\lambda_1 = \lambda$, $\lambda_2 = 1$, $\lambda_3 = \lambda^{-1}$), while the regions of the notch (C) and the sample edge on the opposite side with respect to the cut are in a complex loading state. Then, an increase in the cut length of amount dc (measured in the undeformed state) merely shifts the state of strain in the region C in a direction parallel to the cut, causing the region A to grow at the expense of the region B. Consequently, the growth of a crack by a quantity dc transfers transfers a volume of the test piece of dimensions $h \cdot t \cdot dc$ (where h is the undeformed height of the sample and t is its thickness) from a pure shear state to an undeformed strain state. Moreover, this is valid under the assumption of self-similar crack growth, as defined by Freund [35].

In order to validate the assumptions of self-similar crack growth and about the different strain regions on the samples, different Digital Image Correlation evaluations have been performed on the samples. Some explanatory images of the evaluations performed can be found in Figure 31, where longitudinal and transversal strain fields for the different samples are shown. It is clear that, for all the three samples, there is a region loaded only longitudinally next to the notch (shown as a green region on the transversal strain), while longitudinal strain show that at the

other side of the crack there is a practically unloaded region (the dark blue regions in the longitudinal strains). These evaluations were performed at the maximum imposed deformation on the sample (found for the two different kinds of rubbers in tables 8 and 9), and consequently also the lower strain regimes satisfy two criteria described above.

	Rubber D		
TESTING MACHINE	**INSTRON**		**BIAXTESTER**
SAMPLE	10 mm SAMPLES (JD10)	4 mm SAMPLES (JD04)	SQUARED SAMPLES (JD77)
MIN. AMPLITUDE	60%	120%	20%
MAX. AMPLITUDE	120%	180%	30%
PRESTRAIN	30%	30%	10%
FREQUENCY	2Hz	2Hz	2Hz
DYN. LOADING	Sine Wave	Sine Wave	Sine Wave

Table 8: Specification of the different tests performed in order to evaluate crack propagation characteristics of rubber JD.

4.3 RESULTS AND DISCUSSION

Partial results from the fatigue tests are shown in Figure 32 and 33. There is some scattering in the obtained results, especially in terms of crack speed. However, a greater number of tests should lead to better results in terms of data consistence. As expected, there is agreement between the presented data, although there is partial discordance in the calculation of the power laws for the points fitting.
The whole set of data is then displayed in Figure 34, where also the global trend curves are shown. Here, it can be noticed that the results trend is in accordance with data presented in literature by Lake and Lindley [68], where it can be seen that, as also underlined by Mars and Fatemi [78], the addition of carbon black to

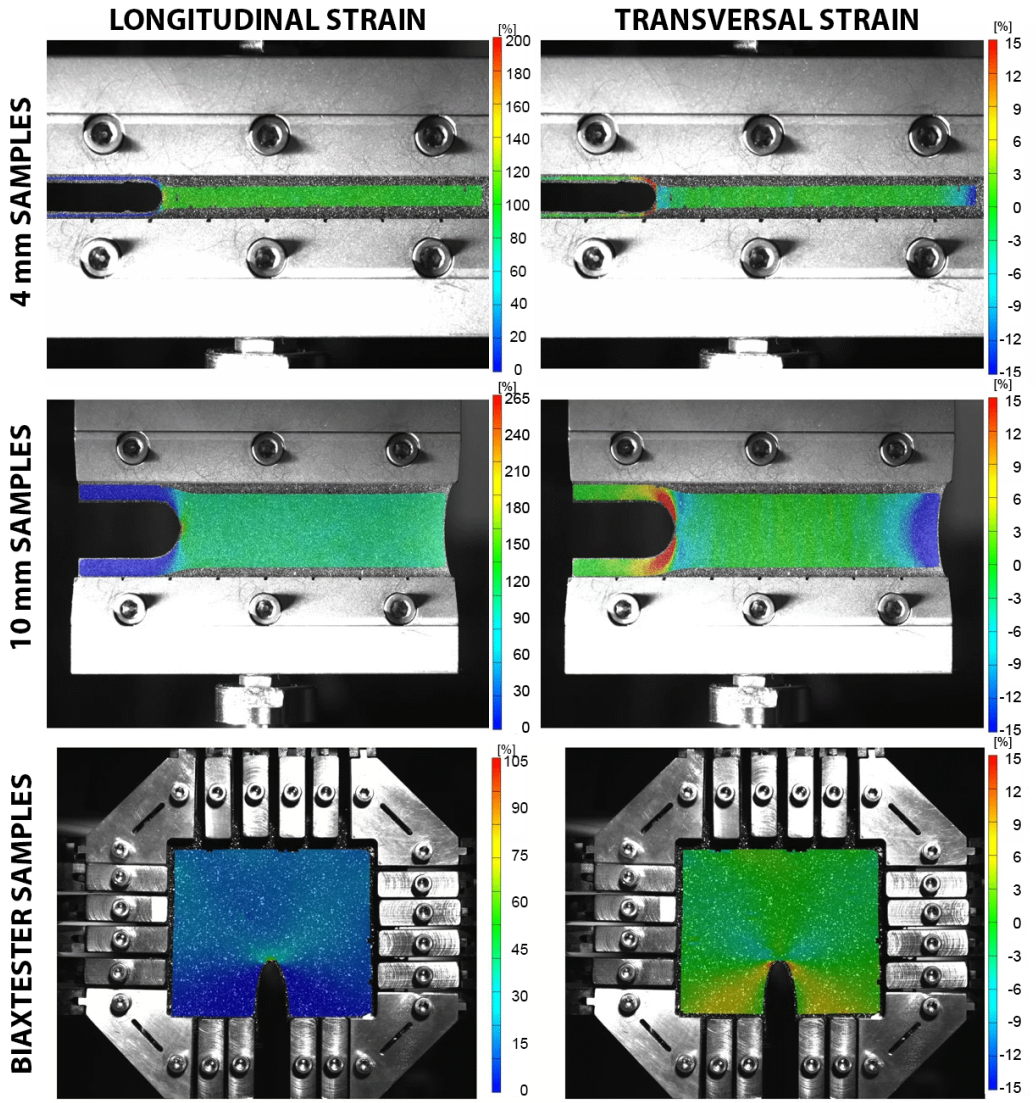

Figure 31: Transversal and longitudinal strain fields of the different types of samples tested. It is easy to notice that all the three types

	Rubber E		
TESTING MACHINE	**INSTRON**		**BIAXTESTER**
SAMPLE	10 mm SAMPLES (JE10)	4 mm SAMPLES (JE04)	SQUARED SAMPLES (JE77)
MIN. AMPLITUDE	70%	140%	20%
MAX. AMPLITUDE	140%	220%	40%
PRESTRAIN	30%	30%	10%
FREQUENCY	2Hz	2Hz	2Hz
DYN. LOADING	Sine Wave	Sine Wave	Sine Wave

Table 9: Specification of the different tests performed in order to evaluate crack propagation characteristics of rubber JE.

rubber compounds can have a pronounced strengthening effect.
In fact it seems that the effect of filler on fatigue properties produces effects such as pronounced changes on stiffness and hysteresis properties and crack tip blunting, deviation and branching induced by inhomogeneity of the rubber-filler composite. However, there are also some effects related to agglomeration of filler particles, which result in increased effective initial flaw sizes: these phenomena are in fact generally in competition, and the filled elastomers have a non-monotonic correspondence between increase in tearing energy and increase in filler concentration. Moreover, SBR typically reach the maximum tearing energy for an amount of carbon black particles between 30 and 60 phr, as reported by Auer et al. [7].

The presented results show a proof of concept regarding the extension of the classical pure shear (in the case of a single edge cut, planar tension specimen) specimen to different geometries, as in the case of the BiaxTester samples. The clamping system of this mechanical device, together with techniques such as Digital Image Correlation and different custom-made scripts to evaluate crack growth and elastically stored energy, show the feasibility of this approach, at least in the case of comparable loading conditions. An interesting approach, that

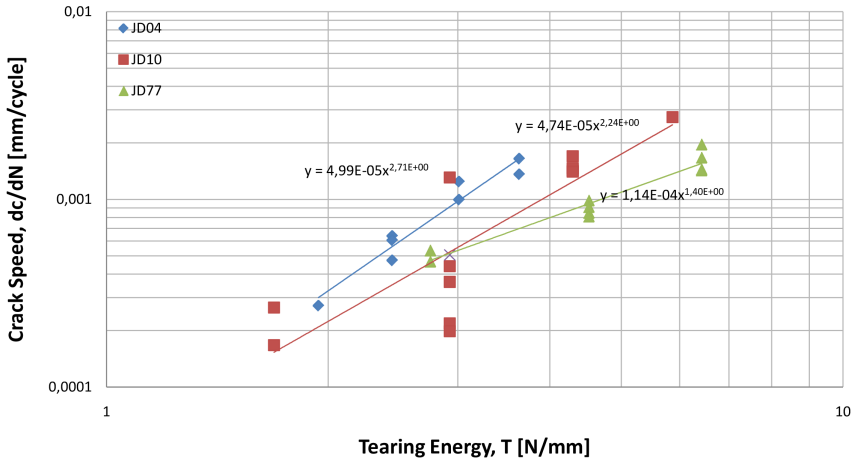

Figure 32: Results obtained through the application of the Rivlin-Thomas approach on the different rubber samples, using as material SBR with 25 phr of carbon black.

can be in general connected to this framework would be to try to apply different methods for the tearing energy evaluation, such as for example the J-Integral approach proposed by Rice [106] and Cherepanov [17], at first in standard loading conditions and then try to verify this approach in more general (and more consistent with real complex loadings) biaxial loadings.

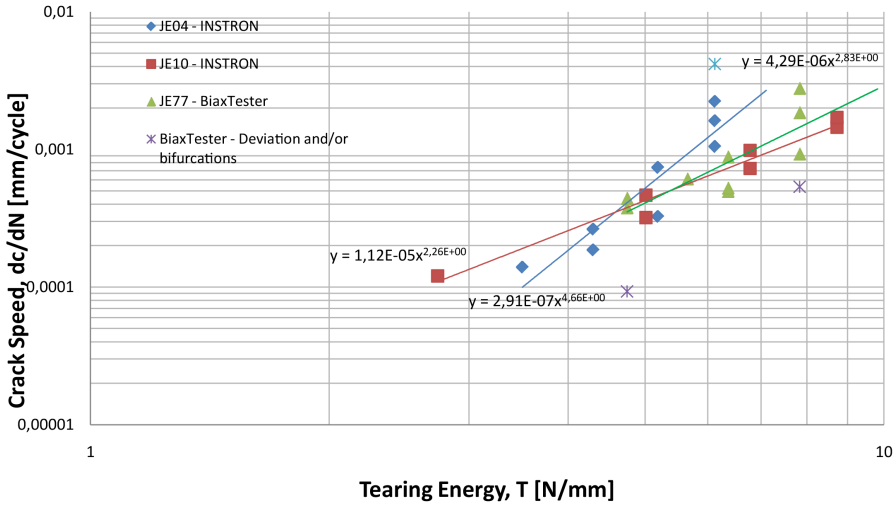

Figure 33: Results obtained through the application of the Rivlin-Thomas approach on the different rubber samples, using as material SBR with 50 phr of carbon black.

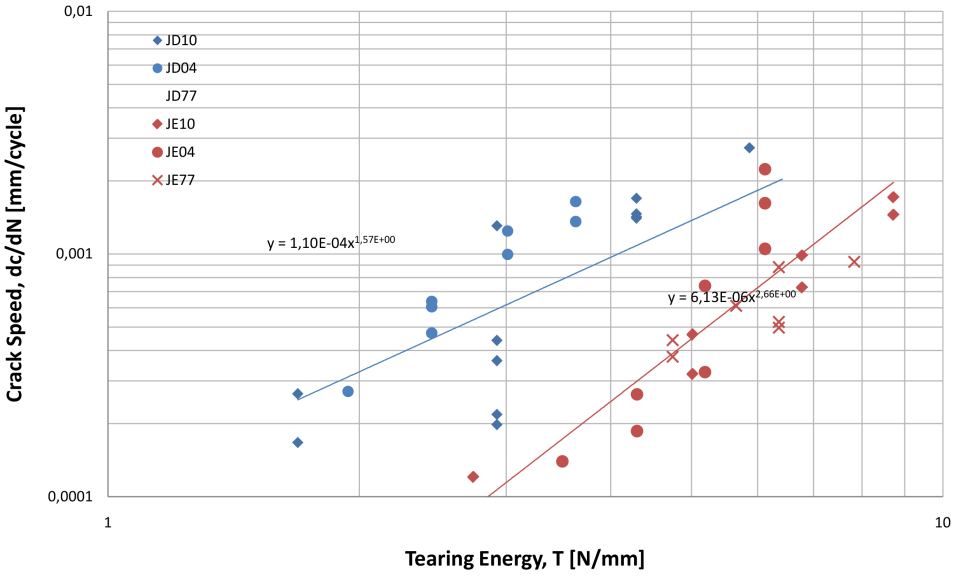

Figure 34: Combination of the results obtained with the two kinds of rubber. As seen also in the work of Lake and Lindley [68] (also reported in the review of Mars and Fatemi [78]), tearing energy tends to increase with the increase of reinforcing filler.

5

CONCLUSIONS

A novel investigation of mechanical behavior of filled rubber has been proposed, concerning biaxial non-standard characterization and modeling of different dissipative effects. The overall work has been developed following three different areas:

- biaxial non-standard mechanical characterization of filled elastomers, in order to highlight different phenomena such as anisotropic stress relaxation under complex loading conditions;
- an operative description of the stress softening and other related phenomena, such as permanent set and hysteresis;
- a constant comparison of the proposed techniques with standard ones, in order to highlight feasibility and possible development of novel approaches able to overcome different problems encountered in mechanical and fatigue characterization of elastomers.

This approach, together with the use of techniques such as Digital Image Correlation and novel mechanical testing machines, such as the BiaxTester, allowed to get interesting results relative to many of the studied aspects. For example, in Chapter 2 the insights about sample and clamping system optimization led towards different deductions about the importance of the surface strain field in biaxial testing of elastomers, as well as path dependence showed at the end of the same Chapter has been an impressive insight in mechanical description of filled elastomers.

Chapter 3, instead, led to many interesting observations about induced anisotropy in this kind of materials. In fact, although as a future prospect, the anisotropy aspect of rubber remains an interesting field that needs to be investigated. However, the developed model itself showed many flexibility and can in general be adapted to model also other aspects of rubber and, in general, of many soft materials. Similar models are, for example, of great interest also in the framework of biological tissues.

In Chapter 4, other aspects related to a different feature of filled elastomers have been investigated, together with the validation of an approach that could, in future, be generalized in order to efficiently improve fatigue characterization of this kind of materials. Investigation of crack propagation for filled SBR, in fact, can be further extended by using a multiaxial criterion for rubber fatigue life, together with the use of biaxial testing machines able to better simulate and describe real cyclic stress conditions, leading towards better characterization of the different phenomena related to crack propagation and strain intensification around the crack tip. Furthermore, Digital Image Correlation can be also employed in order to get more information about the correspondence between crack propagation and strain fields around the crack tip for elastomeric materials, leading towards a better description of many phenomena that are yet to be deeply investigated in this field.

Part III

APPENDIX

A

STRESS-SHIELDING, GROWTH AND REMODELING OF PULMONARY ARTERY REINFORCED WITH COPOLYMER SCAFFOLD AND TRANSPOSED INTO AORTIC POSITION

A version of this Appendix has been published in Biomechanics and Modeling in Mechanobiology:

> Nappi, F., Carotenuto, A. R., **Di Vito, D.**, Spadaccio, C., Acar, C., and Fraldi, M. (2016). *Stress-shielding, growth and remodeling of pulmonary artery reinforced with copolymer scaffold and transposed into aortic position.* Biomechanics and modeling in mechanobiology, 15(5), 1141-1157.

A.1 INTRODUCTION

The application of principles of tissue engineering through the use of bioresorbable materials is increasingly considered an attractive and valid alternative for cardiovascular structures replacement [118]. Specific studies have been also focused on the development of drug-releasing vascular bioresorbable prosthesis able to ameliorate and accelerate processes of endothelialization and vascular regeneration using manufacturing techniques which allow for both a permissive action on the biology of the vessel [119] and the realization of graft able to bear significant hemodynamic loads [16].

Recently, an innovative approach involving the use of fibrillar scaffold made

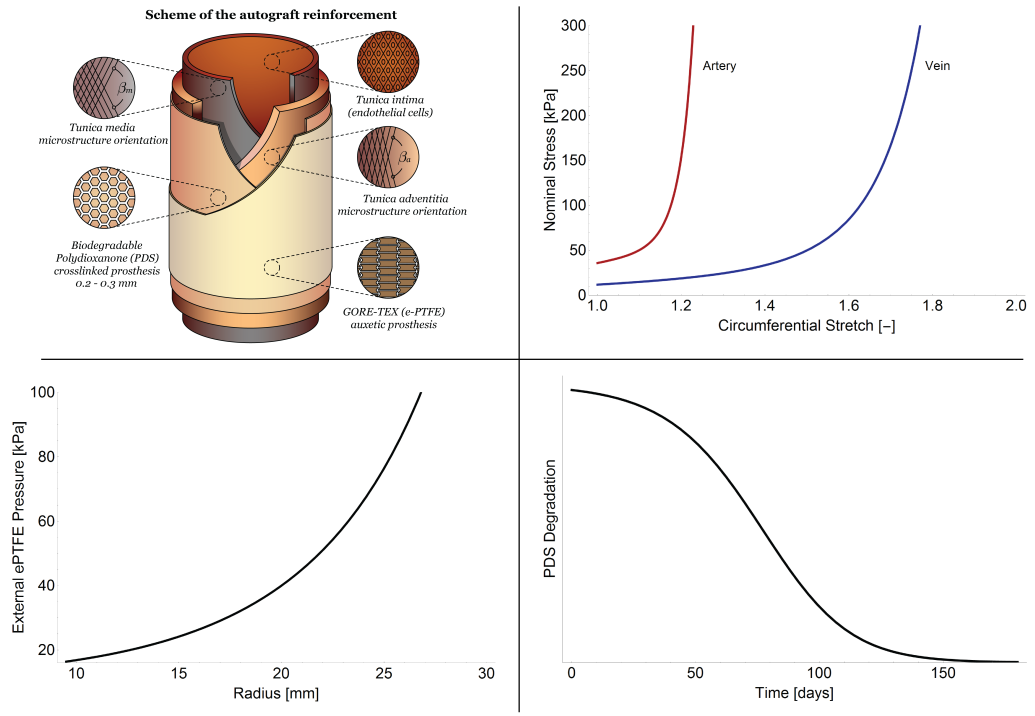

Figure 35: Left (top): Sketch of the main biomechanically relevant features of the pulmonary autograft and the reinforcement. Right (top): Nominal (first Piola-Kirchhoff) hoop stress versus circumferential stretch in artery and vein-like materials. Left (bottom): elastic reaction pressure against external vessel radius dilation exhibited by GORE-TEX auxetic reinforcement during pulmonary autograft growth and deformation. Right (bottom): in-time mass degradation of bioresorbable polydioxanone (PDS) structure.

with polydioxanone (PDS) for the reinforcement of the pulmonary artery in a model of Root Ross operation in the growing lamb has been employed [85–87]. In particular, it might reliably speculate that the temporary interaction between the bioresorbable reinforcement and the PA might have orchestrated a complex process of vascular remodelling based on a balance between inflammation and extracellular matrix production resulting, after biomaterial resorption, in an arterial-like vessel still biologically alive and capable of growth [121]. Indeed, the biomaterial on a side accompanied and accelerated the naturally occurring pressure-load adaptation phenomena attenuating the pressure load exerted on

the pulmonary artery and compensating the tendency to dilation preventing aneurysmal degeneration, but on the other, still permitted and respected somatic growth of vascular structure over time [88].

The observations discussed by Hörer et al. [56] concerning the differential potential of dilation at the various segments of the aorta, i.e. annulus, Valsalva sinuses (0.5 mm/year) and sinutubular junction (increase of 0.7-0.9 mm/year), outlined the need to study the biomechanical changes of pulmonary artery reinforcements in their different parts. This induced to reconsider their design with the aim to better adapt to the normal physiology of the aortic root improving the resistance of the zones, which are meant to majorly suffer from dilatative degeneration. The mechanical stress associated to progressive overstrain of the pulmonary artery under systemic pressure might in fact affect PA integrity and the endothelialization process [120]; therefore, in this context, prevention of the graft stretching is crucial.

To deeply understand the on animal experiments, support the *in vivo* results and overcome some unresolved surgical issues, the biomechanical response (in terms of growth and remodeling) of pulmonary arteries subjected to systemic pressure have been investigated through the use of a mathematical model, to thus analyze the effects of an innovative prosthesis system realized by combining resorbable and auxetic synthetic materials. In fact, as underlined in the last years by Holzapfel [51], soft tissues share many aspects of their mechanical behavior with rubber-like materials, which are the main subjects of this Thesis, including their behavior under finite strain, induced anisotropy, heterogeneity and different aspects related to inelasticity, e.g. viscoelasticity and residual stresses. In particular, the PA composite reinforcement enveloping the arterial walls (*intima*, *media* and *adventitia*) is constituted by a biodegradable scaffold made of polydioxanone (PDS), integrated with an external GORE-TEX weave (expanded polytetrafluoroethylene, e-PTFE) whose structure is characterized by a negative Poisson's ratio (see Figure 35). The proposed biomechanical model seems to provide the positive effects of the synergy of these two synthetic materials, that accommodate mechanical loads guaranteeing graft integrity, controlling the progressive graft dilation,

allowing regional somatic growth and preventing dilatative degeneration [75, 103].

A.2 MATHEMATICAL MODELING

A.2.1 *Preliminary remarks on mechanics and growth of blood vessels*

In the last decades, biomechanical behavior and mechanobiology of cells, tissues and organs have been intensively investigated, with the aim of discovering key feedback mechanisms governing the ways in which cascades of chemical signals are transmitted within the hierarchically organized living structures and interplay with physical events at different scale levels [34]. Continuum Mechanics has deeply contributed to develop this research area and to meet related challenges, by mainly creating the physically and mathematically consistent ground on which large deformation, stresses, evolving constitutive laws, growth, remodeling and morphogenesis do interact [4],[22],[48].
Within this framework, by essentially starting from an approach proposed by [49] and [52] in some recent milestone works on biomechanics of arterial walls, it is here constructed an *ad hoc* non-linear mathematical model for PA, by incorporating tissue growth, remodeling, large deformations and hyperelasticity.
Going *in medias res*, let us consider the body $\mathcal{B}^{(0,0)}$ in its reference stress-free configuration, with dV_0 indicating its volume elements and $\mathbf{X}$ the position of each material point. The evolution of the elastic body can be entirely described by the motion vector $\mathbf{x} = \mathbf{x}(\mathbf{X}, t)$ that maps the material points $\mathbf{X} \in \mathcal{B}^{(0,0)}$ onto spatial points $\mathbf{x}$ at any time t through the definition of the deformation gradient $\mathbf{F}$ defining an application between the two tangent spaces. This deformation gradient can be written by also accounting compatibility with the body particles displacement field $\mathbf{u}(\mathbf{X}, t) \in C^2(\mathcal{B}^{(0,0)})$ as:

$$\mathbf{F} = \nabla_{\mathbf{X}} \mathbf{x}(\mathbf{X}, t) = \mathbf{I} + \mathbf{u}(\mathbf{X}, t) \otimes \nabla_{\mathbf{X}} \tag{97}$$

where ∇ is the *nabla* operator (the subscript indicating the space to which it is referred), while $\otimes$ is the dyadic product. It is standard argument to consider the deformation gradient as composed by different aliquots, respectively responsible of growth, elastic load-induced deformations and residual stress-associated stretches. The most common structure adopted to describe these contributions is a multiplicative decomposition in a way that $\mathbf{F} = \mathbf{F}_e\mathbf{F}_g$ (see e.g. [110]): herein $\mathbf{F}_g$ represents a volumetric growth tensor and $\mathbf{F}_e$ the elastic tensor ensuring compatibility and taking into account both elastic load-induced deformation and residual stresses.
As a matter of fact, the presence of self-equilibrated stresses can be traced if, after cutting out a ring from a blood vessel tract, it contracts (or dilates) along the cylinder generator to release the elastic energy associated to axial stresses and/or if a nonzero opening angle α is measured after cutting the cylindrical ring along its generator to relax hoop stresses [39, 52]. Material points $\mathbf{X}$ are then mapped through the reference configuration towards first non-compatible grown intermediate configuration $\mathcal{B}_g^t$ in which they occupy position $\mathbf{x}_g(\mathbf{X}, t) \in \mathcal{B}_g^t$ and then onto the current loaded configuration $\mathcal{B}^{(t,s)}$, being here denoted by the position vectors $\mathbf{x}(\mathbf{X}, t)$ (see Figure 36). In this configuration, t denotes the ordinary long timescale that follows the growth process (which is of the order of days or months), whereas s indicates the short timescale at which typically mechanical equilibrium is reached. Also, volume elements in these configurations are $dV_g = J_g dV_0$ and $dv = J_e dV_g = J dV_0$, with $J_g = \det \mathbf{F}_g$, $J_e = \det \mathbf{F}_e$ and $J = \det \mathbf{F} = J_g J_e$, respectively. Coherently with experimental observations, the body is assumed to be elastically incompressible, so that $J_e = 1$ and $dv = dV^g$ or $J = J_g$; this also implies that density ρ does not change, growth being purely volumetric [76]. As a consequence, by introducing a source (or sink) term r_g and by neglecting mass fluxes, the mass balance equation can be expressed as:

$$\dot{J}_g = \frac{1}{\rho} J_g r_g, \quad \text{or} \quad \mathbf{F}_g^{-1} : \dot{\mathbf{F}}_g = \bar{r}_g \tag{98}$$

where dot denotes the material time derivative and $\bar{r}_g = \rho^{-1} r_g$ accounts for the mass supply/removal due to the growth process which describes how the body

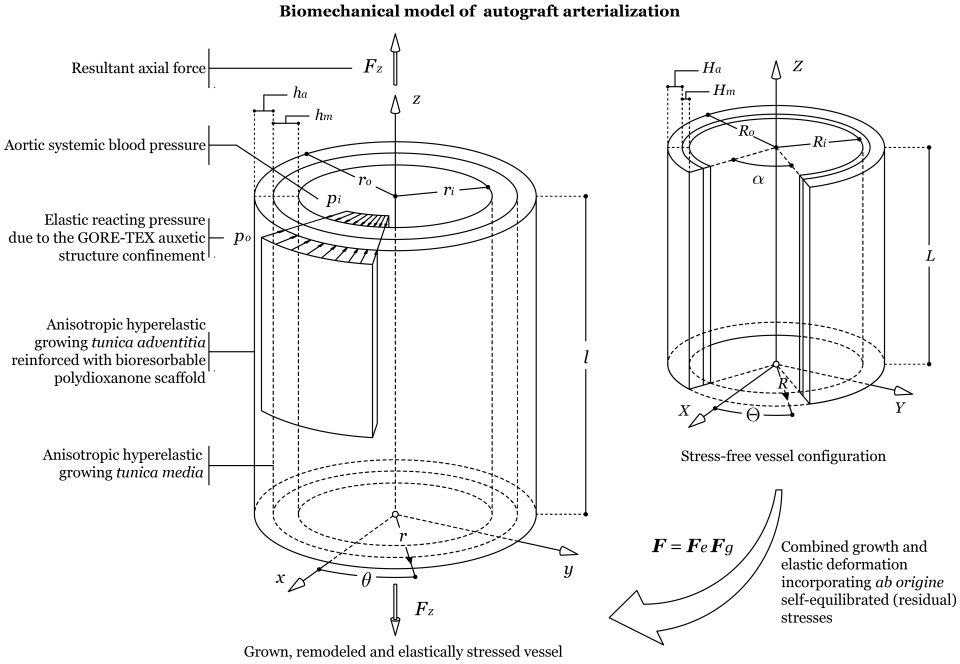

Figure 36: Sketch of the biomechanical model of reinforced pulmonary autograft under aortic systemic pressure including *ab origine* self-equilibrated (residual) stresses, growth, remodeling and elastic deformation.

evolves. In general, the growth may depend on different factors, such as the availability of metabolic energy needed for activating the biological process [39, 128] and other internal conditions, defining the type of interaction among biomaterial constituents and *in situ* stresses, that is known to inhibit (or eventually enhance) selected cellular processes at the basis of the growth mechanisms [3]. In addition, due to axis-symmetry of geometry and loads of the problem at hand, the growth is also expected to be symmetrical and the growth tensor can be thus taken in diagonal form:

$$\mathbf{F}_g = Diag\left\{J_g^{\frac{1-\zeta}{2}}, J_g^{\frac{1-\zeta}{2}}, J_g^{\zeta}\right\} \tag{99}$$

ζ being a coefficient deputed to catch possible tissue growth anisotropies along the longitudinal direction and in the vessel cross-section plane.

By neglecting inertia terms, balance of linear momentum can be written by making

reference to both unstressed and current (grown and elastically deformed) configurations as follows (see e.g. [22])

$$\nabla_{\mathbf{X}} \cdot \mathbf{P} = -\hat{\mathbf{b}}, \qquad \forall \mathbf{X} \in \mathcal{B}^{(0,0)} \tag{100}$$

$$\mathbf{P} \cdot \mathbf{N} = \hat{\mathbf{t}}, \qquad \forall \mathbf{X} \in \partial\mathcal{B}^{(0,0)} \tag{101}$$

or

$$\nabla_{\mathbf{x}} \cdot \boldsymbol{\sigma} = -\mathbf{b}, \qquad \forall \mathbf{x} \in \mathcal{B}^{(t,s)} \tag{102}$$

$$\boldsymbol{\sigma} \cdot \mathbf{n} = \mathbf{t}, \qquad \forall \mathbf{x} \in \partial\mathcal{B}^{(t,s)} \tag{103}$$

where $\mathbf{b}$ and $\hat{\mathbf{b}}$ respectively represent the body force vector in the current configuration and its *pulled-back* version, analogous arguments being applied, by recalling the Nanson's formula, for geometrically interpreting tractions $\mathbf{t}$ and $\hat{\mathbf{t}}$, as well as the outward normal vectors $\mathbf{N}$ and $\mathbf{n}$ to the body surfaces, in the reference and current configurations. In (102) $\boldsymbol{\sigma}(\mathbf{x}, t)$ represents the Cauchy stress, while $\mathbf{P}(\mathbf{X}, t)$ is the first Piola-Kirchhoff (or nominal) stress, these two second order tensors – which coincides under small deformations– being related to each other through the Piola transform:

$$\mathbf{P} = J\boldsymbol{\sigma}\mathbf{F}^{-T} \tag{104}$$

Furthermore, in order to faithfully reconstruct the biomechanical constitutive behavior of the vessel, the strain energy density ψ is here considered as a function of the elastic deformation tensor $\mathbf{F}_e$ and of a vector $\boldsymbol{\gamma}$ containing n_γ remodeling parameters describing the average microstructural changes occurring at the material particles as a consequence of growth and deformation processes. Hence, by following the approach proposed in [94], the total elastic energy referred to the initial configuration takes the form:

$$\Psi = \int_{\mathcal{V}_0} J_g \psi(\mathbf{F}_e, \boldsymbol{\gamma}) dV_0 \tag{105}$$

with $\mathcal{V}_0 = measure(\mathcal{B}^{(0,0)})$. In absence of thermal effects, the application of the second law of thermodynamics and the localization theorem lead to derive the dissipation inequality and, in turn –through the standard Coleman's method [21]– the Piola-Kirchhoff and Cauchy stress tensors as follows:

$$\mathbf{P} = J_g \frac{\partial \psi}{\partial \mathbf{F}_e} \mathbf{F}_g^{-T} \quad \text{and} \quad \boldsymbol{\sigma} = \frac{\partial \psi}{\partial \mathbf{F}_e} \mathbf{F}_e^T \tag{106}$$

Finally, once a total energy (105) directly dependent on the remodeling variables $\boldsymbol{\gamma}$ has been introduced, the reduced dissipation inequality allows to write the remodeling evolution equation in the following form:

$$\dot{\boldsymbol{\gamma}} = c_\gamma \left(\mathbf{K} - J_g \frac{\partial \psi}{\partial \boldsymbol{\gamma}} \right), \qquad c_\gamma \geq 0 \tag{107}$$

c_γ being a non-negative term (either constant or not) accounting for the characteristic remodeling time, and $\mathbf{K}$ representing a proper remodeling work conjugate vector which can be also interpreted as a sort of drag force (see Appendix B) associated to the remodeling process [94].

A.2.2 *Inflation and growth-associated stresses in vessel walls*

From a geometric viewpoint, a blood vessel can be seen as a thick-walled hollow (composite) cylinder, each layer exhibiting elastic anisotropy as a result of the tissue microstructure (see Figure 35). From the mechanical standpoint, several works can be found in literature where the problem of determining the elastic response of composite cylinders under different load conditions is approached and analytically solved [31], also in case of anisotropy [32] and for general inhomogeneous media [33]. However, pressure regimes and growth generally induce large deformations in the blood vessels and therefore non-linear models are required (see for instance [52] and [19]). Within the non-linear theory of elasticity, and by making reference

to the geometrical symmetries, the unstressed reference configuration $\mathcal{B}^{(0,0)}$ can be then described in terms of cylindrical coordinates by the region:

$$\begin{aligned} R_i \leq & R \leq R_o, \\ 0 \leq & \Theta \leq (2\pi - \alpha), \\ 0 \leq & Z \leq L \end{aligned} \tag{108}$$

where R_i and R_o indicate the inner and the outer radii of a relaxed and excised configurations, L is the vessel trunk length and α is the opening angle, a measure of the elastic energy imprisoned within the material before ideally cutting the vessel to go back to a virtual stress-free reference configuration and due to *ab origine* self-equilibrated (residual) stress (see Figure 36). Analogously to the pure inflation problem, under the hypotheses of axis-symmetry of both loads (i.e. the systemic aortic blood pressure) and growth, the deformed *in situ* configuration can be instead described by the region:

$$\begin{aligned} r_i \leq & r \leq r_o, \\ 0 \leq & \theta \leq 2\pi, \\ 0 \leq & z \leq l \end{aligned} \tag{109}$$

with $\theta = h\Theta$ and $h = 2\pi/(2\pi - \alpha)$. This also implies that the deformation gradient can be helpfully written in terms of principal stretches, i.e. $\mathbf{F} = \lambda_{rR}\mathbf{e}_r \otimes \mathbf{e}_R + \lambda_{\theta\Theta}\mathbf{e}_\theta \otimes \mathbf{e}_\Theta + \lambda_{zZ}\mathbf{e}_z \otimes \mathbf{e}_Z$. By taking into account the residual stress-induced opening angle, growth and elastic deformations, the total stretches

are univocally determined by starting from the relation $dv = J_g dV_0$ accounting the elastic incompressibility, thus obtaining:

$$\begin{aligned} \lambda_{rR} &= \frac{\partial r}{\partial R} = J_g^{1-\zeta} \frac{R}{r h \lambda_{ezZ}} \\ \lambda_{\theta\Theta} &= h \frac{r}{R} \\ \lambda_{zZ} &= \frac{l}{L} = J_g^{\zeta} \lambda_{ezZ} \end{aligned} \tag{110}$$

where the axial stretch time-history λ_{zZ} may be assumed to be prescribed, for example deriving it from experimental observations [85]. In particular, by considering that *in situ* vessels exhibit residual axial strains which allometrically increase as the overall body grows, a possible form of the stretch λ_{zZ} can be faithfully described by means of the following evolution function:

$$\begin{aligned} \lambda_{zZ}(t) = &\frac{\lambda_{zZ}^f + \lambda_{zZ}^i}{2} + \\ &+ \frac{\lambda_{zZ}^f - \lambda_{zZ}^i}{2} \tanh\left(\omega_z \left(t - t_z\right)\right) \end{aligned} \tag{111}$$

where λ_{zZ}^i and λ_{zZ}^f represent the initial and the final observed stretch ratios, while t_z and ω_z are a characteristic time and a suitable frequency constant, respectively. Furthermore, by virtue of the elastic incompressibility constraint, the following relation for the radius r at the current time can be derived:

$$\begin{aligned} r &= \sqrt{\frac{2}{h \lambda_{ezZ}} \int_{R_i}^{R} J_g^{1-\zeta}\left(\overline{R}\right) \overline{R} d\overline{R} + r_i^2} = \\ &= \sqrt{J_g^{1-\zeta} \frac{R^2 - R_i^2}{h \lambda_{ezZ}} + r_i^2} \end{aligned} \tag{112}$$

in which the assumption of uniform growth tensor has been introduced, according to recent literature works [104, 130].

By following the work by [52], arteries can be mechanically modeled by consid-

ering a two-layer hollow cylinder, the inner and the outer layers representing the *tunica media* and the *tunica adventitia*, respectively, the mechanical contribution of the *tunica intima* being negligible. Both of them can be constitutively characterized by a strain energy function made of an isotropic part and an anisotropic contribution which accounts for the fibers orientation. Hence, by also introducing a suitable Lagrange multiplier q^{ξ} to take into account the elastic incompressibility constraint, the strain energy functions reads as:

$$\begin{aligned}\psi^{\xi} =&\psi^{\xi}_{iso}\left(I_1\right)+\psi^{\xi}_{aniso}\left(I_4,I_6\right)= \\ =&\frac{k^{\xi}_0}{2}\left(I_1-3\right)+\frac{k^{\xi}_1}{2k^{\xi}_2}\sum_{i=4,6}\left(e^{k^{\xi}_2\left(I^{\xi}_i-1\right)^2}-1\right)+ \\ &-q^{\xi}\left(J_e-1\right)\end{aligned} \tag{113}$$

where ψ^{ξ}_{iso} and $\psi^{\xi}_{aniso}\left(I_4,I_6\right)$ respectively characterize the mechanical response of the volumetric part and the response of the vessel (elastic and collagen) fibers; the superscript $\xi=\{m,a\}$ denotes *media* and *adventitia*, while $k^{\xi}_{0,1,2}$ are suitable material constants, being k^{ξ}_0 related to the volumetric response. The above introduced energy densities are then written as a function of the invariants [52]:

$$\begin{aligned}I_1&=\operatorname{Tr}\mathbf{C}_e \\ I^{\xi}_4&=\mathbf{C}_e:\left(\mathbf{a}^{\xi}_+\otimes\mathbf{a}^{\xi}_+\right) \\ I^{\xi}_6&=\mathbf{C}_e:\left(\mathbf{a}^{\xi}_-\otimes\mathbf{a}^{\xi}_-\right)\end{aligned} \tag{114}$$

where $\mathbf{C}_e=\mathbf{F}^T_e\mathbf{F}_e$ is the left Cauchy-Green tensor and $\mathbf{a}^{\xi}_{+,-}=\cos\beta\mathbf{e}_{\Theta}\pm\sin\beta\mathbf{e}_Z$ represent the fibers directors lying within the *media* and the *adventitia*. The application of the Piola transform $(106)_2$ returns the expression for the Cauchy stress tensor, connected to (113) by the relationship:

$$\boldsymbol{\sigma}^{\xi}=J_g^{-1}\mathbf{P}^{\xi}\mathbf{F}^T=\frac{\partial\psi^{\xi}}{\partial\mathbf{F}_e}\mathbf{F}^T_e-q^{\xi}\mathbf{I} \tag{115}$$

Then, by rewriting $(102)_1$ in absence of body forces and in the current configuration as $\nabla_{\mathbf{x}} \cdot \boldsymbol{\sigma}^{\xi} = \mathbf{0}$, the sole non-trivial equilibrium equation to be satisfied is:

$$\frac{d\sigma_{rr}^{\xi}}{dr} + \frac{\sigma_{rr}^{\xi} - \sigma_{\theta\theta}^{\xi}}{r} = 0 \tag{116}$$

Direct integration of this equation –separately written for both *media* and *adventitia*– combined with the condition describing the inner deformed radius once the tractions on the walls are prescribed, gives:

$$\begin{aligned} &\sigma_{rr}^{a}(r_o) - \sigma_{rr}^{m}(r_i) = \Delta p = \\ &= \sum_{\xi} \int_{\mathfrak{I}^{\xi}} J_g^{\frac{\zeta-1}{2}} \left(h \frac{r}{R} \frac{\partial \psi^{\xi}}{\partial \lambda_{\theta\Theta}} - \frac{\partial r}{\partial R} \frac{\partial \psi^{\xi}}{\partial \lambda_{rR}} \right) \frac{\partial r}{\partial R} \frac{dR}{r} \end{aligned} \tag{117}$$

with $\mathfrak{I}^{m} = [R_i, R_i + H_m]$ and $\mathfrak{I}^{a} = [R_i + H_m, R_o]$, H_m representing the thickness of the *tunica media*. By prescribing continuity of radial stresses and of displacements at the vessel layers interface, the corresponding interface radius in the deformed configuration can be determined by employing the relation

$$r_H = \sqrt{r_i^2 + J_g^{1-\zeta} h^{-1} \lambda_{ezZ}^{-1} H_m (H_m + 2R_i)} \tag{118}$$

The pressures $\sigma_{rr}^{a}(r_o)$ and $\sigma_{rr}^{m}(r_i)$ are instead related to the external loading condition through the Cauchy's theorem $(102)_2$ or $\boldsymbol{\sigma}^{\xi} \cdot \mathbf{n}^{\xi} = \mathbf{t}^{\xi}, \ \forall \mathbf{x} \in \partial \mathcal{B}^{\xi}$.
From the computational standpoint, it is worth to highlight that, once the loading conditions have been assigned, the equilibrium relation (117) can be analytically solved for each finite time step during which growth can be assumed constant, in this way reducing to the sole unknown r_i and thus obtaining the deformed configuration through (112).

A.2.3 *Biomechanics of reinforced pulmonary artery transposed into aortic position*

As already said, by testing an *ad hoc* designed prosthesis system made of a combined bioresorbable scaffold and an auxetic reinforcement, some of the present authors have recently successfully pioneered a large animal model of transposition of pulmonary artery in systemic pressure load. This experimental *in vivo* study, aimed to replicate actual clinical scenarios, has enabled to observe a physiological arterialization of the reinforced pulmonary vessels transposed into aortic position [85, 88, 121], resulting in PA medial thickening and matrix rearrangement (see Figure 37).

To biomechanically support these *in vivo* experimental findings and gain insights into possible enhancements of PA reinforcements design criteria, a mathematical model is built up by incorporating vessel growth, remodeling and large elastic deformations of both biological and synthetic materials.

Three theoretical simulations of experimental interest have been then performed, that is the benchmark case of *reference* aorta, the not-reinforced pulmonary artery and the PA reinforced with both an e-PTFE (GORE-TEX) auxetic cladding and a PDS bioresorbable scaffold, these three models being all subjected to the action of systemic pressure.

With reference to the theory presented in the previous Sections, some additional key features have been introduced to faithfully describe the above mentioned cases.

First of all, the effect of the blood vessel structural remodeling on the tissues elasticity has been analyzed and thus mathematically described in terms of change of mechanical properties. To make this, suitable remodeling parameters γ^m and γ^a have been introduced to guide the evolution of bulk moduli k_0^m and k_0^a of *media* and *adventitia*, respectively. As a result, the tunics energy densities become explicitly dependent on them, i.e. $\psi_{iso}^{\xi} = \psi_{iso}^{\xi}\left(I_1, \gamma^{\xi}\right)$, so mimicking the temporal elastic properties changes also experimentally observed by [58]. Also, with reference to (107), the role of the remodeling enhancers $\mathbf{K}$ is assumed to be played by the average levels of energy densities occurring in the aortic layers in a physiological

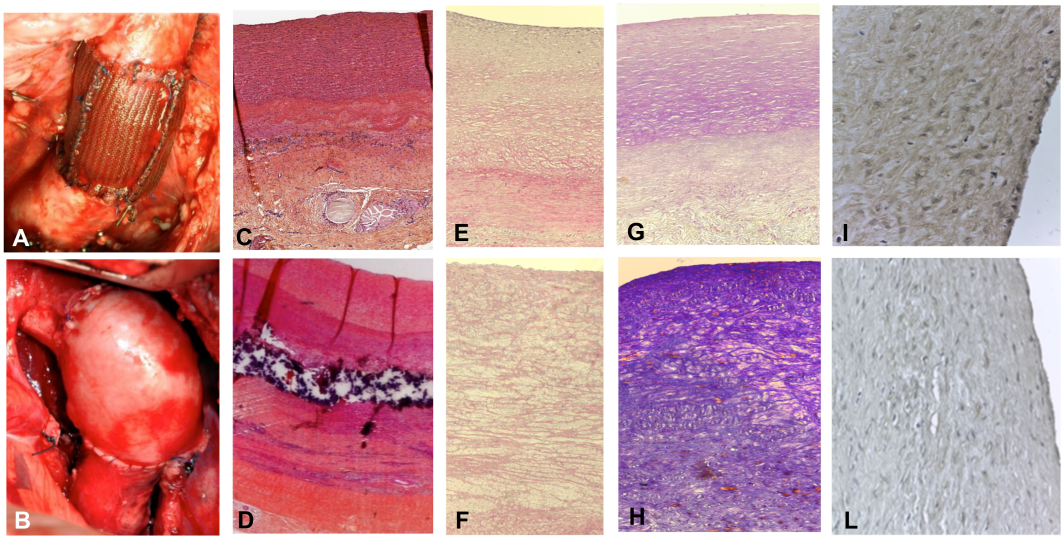

Figure 37: A-B) Surgical implant. A. Bioresorbable reinforcement; B. Control. C-D) Hematoxylineosin staining. C. Bioresorbable reinforcement. Note remnants of PDS. D. Control. Note medial disruption and inflammatory infilitrates; E-F) PicroSirius red staining. E. Bioresorbable reinforcement compact collagen organization: the "elastic zone" of the vessel and less pronounced cellular infiltrate. F. Control. Dispersed collagen fibers; G-H) Mallory staining; G. Bioresorbable reinforcement. Elastin deposition (pink). H. Control. Presence of collagen (blue); I-L) MMP-9 immunohistochemistry. I. Bioresorbable reinforcement. Note MMP-9 overexpression in the PDS group indicating active matrix remodeling phenomena. L. Control.

situation, in this manner interpreting the remodeling as an energy-driven process which dynamically responds to energy supplies with tissue structural changes – over selected timescales– to accommodate stress and strain and in turn minimize energy, a logic to which many biomaterials seem to obey if subjected to remodeling [22].

For the sake of simplicity, the parameters γ^{ξ} have been here considered as volume averaged values, so that the equation (107) can be written in the following scalar form:

$$\dot{\gamma}^{\xi} = c_{\gamma} J_g \left(\overline{\psi}^{\xi}_{A,iso} - \frac{\partial \overline{\psi}^{\xi}_{V}}{\partial \gamma^{\xi}} \right) \tag{119}$$

where $c_\gamma \geq 0$ is a dimensional constant which takes into account the characteristic long-term timescale of remodeling (ranging from about 4000 h to 40000 h, as reported by [132]), whereas ψ_A^ξ and ψ_V^ξ respectively denote the energy functions specialized for the aorta and the PA trunk subjected to a volume averaging process (see the synoptic Table 11 for the adopted material parameters):

$$\overline{\psi}_{A,V}^{\xi} = \frac{1}{\mathcal{V}_0} \int_{\mathcal{V}_0} \psi_{A,V}^{\xi} dV_0 \tag{120}$$

Furthermore, to accurately model the reinforced PA case, how degrading polydioxanone (PDS) mesh and e-PTFE external armor do cooperate and in-time support the vessel walls must be additionally mathematically described. With reference to the PDS structure, this is indirectly done by mechanically *enriching* the *adventitia* with an augmented time-dependent bulk modulus decreasing in time according to a selected experimentally based degradation law. In this way, the updated *adventitia* bulk modulus, say κ_0^a, takes the form:

$$\kappa_0^a = \gamma^a(t)\, k_0^a + (\phi(t))^\nu\, k_0^s \tag{121}$$

where k_0^s constitutes the PDS contribution to the overall (reinforced) *adventitia* bulk modulus, $\phi(t)$ is a degradation law which describes the scaffold volume fraction pauperization[1] (according to the actual PDS mass bioresorption program in a six-months period, see e.g. [89]), here chosen as (see Figure 35, right-bottom graphic):

$$\phi(t) = \frac{\phi_0}{1 + \omega_1 e^{\omega_2 (t - t_s)}} \tag{122}$$

where ϕ_0 is a constant representing the initial PDS volume fraction which accounts for the porosity of the scaffold [12] while ν is a dimensionless, strictly positive (typically between 1 and 3) penalization power, employed to have as a result the well-known less than proportional stiffness increase with the material

1 There is thus a direct effect of the PDS pauperization on the growth, remodeling and in turn on the overall elastic properties of the *adventitia*, but not vice versa, that is growth and remodeling do not affect (or perturb) the PDS degradation law.

volume fraction of a porous representative volume element [22, 66].
Also, in (122), t_s accounts for a characteristic inflection time and ω_1 and ω_2 represent constants to be set in order to fit the experimental PDS degradation curve [111], [12], [81]. In this way, the model accurately catches the role exerted by the PDS scaffold in terms of vessel wall stiffening, at the early stages of growth the PDS mesh supporting the pulmonary artery to resist to higher systemic blood pressures –so avoiding excessive strain in turn provoking high stress and finally aneurysms– then progressively degrading and slowly accompanying the autograft toward possible remodeling and arterialization-like processes.

On the other hand, the role played by the e-PTFE auxetic structure –that is somewhat complementary to that of PDS– has been modeled to reproduce an initial auxetic-induced relatively low contribution to vessel elastic resistance against load pressure, becoming the confinement effect increasing as tissue grows up, moving outward the external PA radius. From the mathematical point of view, this is translated into an elastic *reactive* pressure transmitted at the PA outer cylindrical surface as the external radius expands (see Figure 35, left-bottom graphic). Therefore, by imaging the e-PTFE net as an external layer simply described by an exponential strain energy potential whose structure is similar to that in (105), and assuming that no external pressure is applied on this layer, the following relationship can be established [49]:

$$\sigma_{rr}^{n}(r_o) = -\int_{\lambda_e}^{\lambda_o} \frac{1}{\lambda_T^2 \lambda_Z - 1} \frac{\partial \psi^n}{\partial \lambda_T} d\lambda_T, \tag{123}$$

$$\psi^n = \frac{k_1^n}{k_2^n}\left(e^{k_2^n\left(I_4^n - 1\right)} - 1\right) \tag{124}$$

given that $I_4^n = I_6^n = \lambda_T^2 \cos^2 \eta_n + \lambda_Z^2 \sin^2 \eta_n$, η_n being the mesh half-angle. In equation (123) λ_T and λ_Z denote the azimuthal and the longitudinal stretches

which completely describe the deformation of the auxetic net, whose associated deformation gradient is thus

$$\mathbf{F}^n = Diag\left\{\frac{RL_n}{r_n l_n}, \frac{r_n}{R}, \frac{l_n}{L_n}\right\} \tag{125}$$

By taking $\lambda_Z = l_n/L_n$ to be constant, the condition at the interface $r_o = r(R_o)$ immediately gives $\lambda_Z = J_g^{\zeta}\lambda_{ezZ}$ and the e-PTFE structure motion r_n can be described similarly to (112) and related to the vessel outer radius as written down:

$$r_n = \sqrt{\frac{R^2 - R_o^2}{\lambda_Z} + r_o^2} = \sqrt{J_g^{-\zeta}\frac{R^2 - R_o^2}{\lambda_{ezZ}} + r_o^2}, \tag{126}$$

where

$$r_o = \sqrt{J_g^{1-\zeta}\frac{R_o^2 - R_i^2}{h\lambda_{ezZ}} + r_i^2} \tag{127}$$

Hence, the equations (112) and (126) allow to derive the square stretches at the the boundary as a function of r_i:

$$\lambda_o^2 = \frac{r_o^2}{R_o^2} = \frac{1}{R_o^2}\left(J_g^{1-\zeta}\frac{R_o^2 - R_i^2}{h\lambda_{ezZ}} + r_i^2\right) \tag{128}$$

$$\begin{aligned}\lambda_e^2 &= \frac{r_e^2}{(R_o + H_n)^2} = \\ &= \frac{1}{(R_o + H_n)^2}\left(J_g^{-\zeta}\frac{H_n(2R_o + H_n)}{\lambda_{ezZ}} + r_o^2\right)\end{aligned} \tag{129}$$

where H_n is the initial auxetic armor thickness. The equilibrium equation $\sigma_{rr}^n(r_o) = \sigma_{rr}^a(r_o)$ to be satisfied at the interface r_o then gives the possibility of finding, by integrating (123), the actual pressure that the armor applies on the *adventitia* by elastically reacting to the vessel deformation and growth. In particular, by performing the substitution $x = k_2^n\left(I_4^n - 1\right)$, it is possible to

compactly write:

$$\sigma_{rr}^{a}(r_o) = -p_o = \frac{k_1^n e^{-Q}\cos^2\eta_n}{\lambda_Z}\int_{x_o}^{x_e}\frac{e^{x+Q}}{x+Q}dx = \\ = \frac{k_1^n e^{-Q}\cos^2\eta_n}{\lambda_Z}\left(\mathrm{Ei}\left(\mathrm{x_e}+\mathrm{Q}\right)-\mathrm{Ei}\left(\mathrm{x_o}+\mathrm{Q}\right)\right) \tag{130}$$

with $Q = 1 - k_2^n\lambda_Z^2\sin^2\eta_n - k_2^n\lambda_Z^{-1}\cos^2\eta_n$ and $\mathrm{Ei}(\mathrm{x})$ representing the exponential integral function, while $x_e = x\left(\lambda_e^2\right)$ and $x_o = x\left(\lambda_o^2\right)$ are both functions of the updated vessel outer radius r_o (or equivalently r_i) through $(128)_1$ and $(128)_2$, that is:

$$x_e + Q = k_2^n\cos^2\eta_n\left(\lambda_e^2 - \lambda_Z^{-1}\right) \\ x_o + Q = k_2^n\cos^2\eta_n\left(\lambda_o^2 - \lambda_Z^{-1}\right) \tag{131}$$

Lastly, all the *in silico* simulations (in detail discussed below) are conducted by assuming the growth to obey a typical logistic profile, a law largely encountered in the literature to describe many different growth dynamics of living systems, at different scale levels, and hence widely adopted among biologists to fit related experimental data [61]; as a consequence, in order to consider the direct effect of the experimentally observed growth of the lambs discussed in [85] on the mechanical analysis of the vessels alone and the reinforced PA system, it is here proposed to transpose the logistic growth assumption also to the tissue scale, as a first step also hypothesizing a stress-uncoupled growth as a simplifying rationale to mimic the physiological growth curve. Thus, the equation (98) can be explicitly given in the form:

$$\dot{J}_g = c_g J_g\left(1 - \frac{J_g}{J_g^{max}}\right) \tag{132}$$

where J_g^{max} represents a prescribed upper bound reference value, in the present case evaluated on the basis of the (allometrically scaled) body size achieved by the adult animal model with respect to the initial size [85–87], while $c_g \geq 0$ is a proper

growth rate (see e.g. [44]).
With respect to the case of reference artery, only physiological growth during a six-month period with no internal remodeling has been assumed: also, for both the cases of reference artery and not reinforced PA, the analyses have been conducted by considering the presence of the sole systemic aortic pressure, thus prescribing to the biomechanical models zero external loads at the outer radius and internal pressure p_i –typically of the order of 100-120 mmHg– assumed to be constant during the time step of the analyses. As a result, the equation (117) becomes:

$$p_i = \sum_{\xi\in\{m,a\}} \int_{\mathfrak{I}^\xi} J_g^{\frac{\zeta-1}{2}} \left(h\frac{r}{R}\frac{\partial \psi^\xi_{A,V}}{\partial \lambda_{\theta\Theta}} - \frac{\partial r}{\partial R}\frac{\partial \psi^\xi_{A,V}}{\partial \lambda_{rR}} \right) \frac{\partial r}{\partial R}\frac{dR}{r} \tag{133}$$

with which the two above mentioned cases can be distinguished and separately treated by specializing the strain energy functions through proper assignments of different intrinsic parameters, so that ψ^ξ_A and ψ^ξ_V can be recognized as representative of aorta and pulmonary artery (vein-like) materials, respectively.
On the other side, by making reference to the above proposed theoretical strategy for describing how the bioresorbable scaffold and the auxetic structure do cooperate to reinforce the pulmonary autograft, the balance equation (117) reads as:

$$p_i - p_o = \sum_{\xi\in\{m,a\}} \int_{\mathfrak{I}^\xi} J_g^{\frac{\zeta-1}{2}} \left(h\frac{r}{R}\frac{\partial \psi^\xi_{V}}{\partial \lambda_{\theta\Theta}} - \frac{\partial r}{\partial R}\frac{\partial \psi^\xi_{V}}{\partial \lambda_{rR}} \right) \frac{\partial r}{\partial R}\frac{dR}{r} \tag{134}$$

Finally, the equations (132) and (133) constitute the system to be solved for analyzing the reference aorta, in which the sole unknowns are the growth term J_g and the inner radius r_i; the same equations have to be coupled with (119) to model the not reinforced PA biomechanical response. Analogously, to simulate the biomechanical behavior of the reinforced PA, the equations (134), (132) and (119), which incorporate the remodeling parameters γ^a and γ^m responsible for arterialization

phenomena, have to be instead used.
From the numerical standpoint, the simulations to be conducted for reference artery, pulmonary artery and reinforced autograft, require suitable material and geometric parameters, in detail reported in Table 11. For the sake of clarity, the parameters have been divided in different sections regarding the different model constituents: both aortic and pulmonary artery constitutive parameters have been deduced from [15, 52, 94, 131], the opening angle value being instead referred to the range proposed by [1]. The geometric parameters have been extrapolated by the *ex vivo* data obtained throughout the experimental observations (see the Appendix A). Lastly, the material parameters concerning both the PDS and the e-PTFE volumetric response have been determined from the inflation compliance data reported in literature [12, 63, 113, 116, 117, 123].

A.3 RESULTS AND DISCUSSION

The analyses have been performed by implementing the above detailed biomechanical models in the computational software program MATHEMATICA®. Here, the partial differential equations governing the problems have been solved analytically in space, for each time step, and hence the complete solution found by numerically integrating over the whole six-month observation period related to the animal model [85].
The obtained results highlight that, although the PA tracts were initially the same from a physiological and a constitutive point of view, under the systemic blood pressure their behavior significantly diverges in the two cases, i.e. reinforced and not reinforced vessels. In fact, results show that the cooperation between bioresorbable PDS scaffold and permanent e-PTFE auxetic structure plays a crucial role in preventing a fateful yielding of the vessel, wall intrinsic mechanical properties in absence of reinforcement being absolutely inadequate to both respond to the new imposed aortic pressure regimes and limit large deformations prodromal to aneurismal complications. In particular, theoretical outcomes, illustrated in Figure 38, clearly show a marked difference among reference aorta, PA alone and PA with

prosthesis, in terms of pressure-induced initial burst dilatation and final associated vessels diameters, a fact also quantitatively confirmed by experimental observations [85] and summarized in Table 10. Theoretical predictions are indeed in very good agreement if compared with experimental data, except for a slight underestimation of not reinforced PA sizes, mainly related to the fact that, in absence of prosthesis, actual strains are not purely due to combined elastic deformation and growth, additional inelastic strains being kindled by locally occurring irreversible (i.e. visco-elastic-plastic and damaging) phenomena, as can be seen by direct observations (Figure 40). The analytical curves also underline a specific non-linear trend, in terms of vessel diameters time-history, which shows a sort of asymptotic behavior that furnishes an upper bound to vessel growth in proximity of body adulthood, a phenomenon otherwise unforeseeable on the basis of the sole initial (at one day) and final (at six months) observations and qualitatively crucial to envisage a successful prognosis of the PA reinforcement also when this surgical protocol is applied to young human patients.

As a matter of fact, the not reinforced PA excessively dilates during the time window considered, passing from an initial diameter of about 29.5 mm –measured in the first days– to a diameter of about 38.1 mm, after six months. Moreover, the actual deformation profiles of the not reinforced PA go off the vessel from the tube-like shape, by losing the axis-symmetry of the response assumed in the present theoretical model, as can be observed from the angiographic measures (Figure 39), as well as from *in situ* (Figure 37) and explanted *ex vivo* vessel trunks (Figure 40).

On the contrary, in the doubly reinforced PA, the mathematical model demonstrates that the prosthesis system overall works as a sort of "relay race", by guaranteeing the handover of the bearing structure functions from the PDS scaffold (at the early stages of tissue growth and remodeling) to the e-PTFE armor, initially "dormant" as a consequence of the typically low stiffness exhibited by stress-free auxetic structures at small strains. In this way, the mechanical shielding of the lapse vessel confines the radial expansion and simultaneously allows to the pulmonary artery to remodel its tunics for attaining an adequate level of mechanical properties (e.g. elastic bulk moduli, see Figure 42). Finally, once the bioresorbable

scaffold has completed its degradation program and the strengthened vessel walls can actively respond to the systolic pressure, the e-PTFE structure accompanies PA *media* and *adventitia* toward their progressive aortic somatic growth, by stretching its weave to gain stiffness and effectively confine further vessel expansion, so avoiding tissue prolapse and aneurismal degenerative phenomena.

Furthermore, Figure 38 also shows that the mathematical model predicts a "gain"

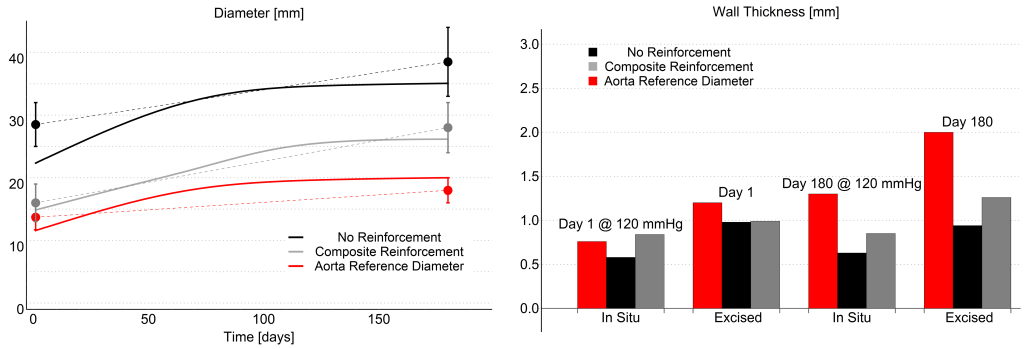

Figure 38: Left: Evolution of the outer diameters (continuous lines represent theroetical outcomes while markers are experimental measures). Right: Vessels thicknesses provided by the simulations at day 1 and at day 180 when the vessels are either in position or excised.

	Day 1		**Day 180**	
	Experimental	**Analytical**	**Experimental**	**Analytical**
Reference Aorta	13.0–16.4	13.1	17.0–21.0	21.0
Composite Reinforcement	14.0–20.0	16.3	25.0–33.0	27.2
No Reinforcement	25.0–33.0	24.2	34.3–42.0	36.1

Table 10: Comparison of the external diameters (expressed in mm) - experimental observations vs analytical predictions

of the reinforced grown PA to be measured in terms of wall thickness occurring when the PA tracts are ideally excised and relaxed, as well as when the vessels are subjected to the *in situ* inflation pressure, so highlighting an effective thickening of the reinforced graft after the observation period that can be directly related to

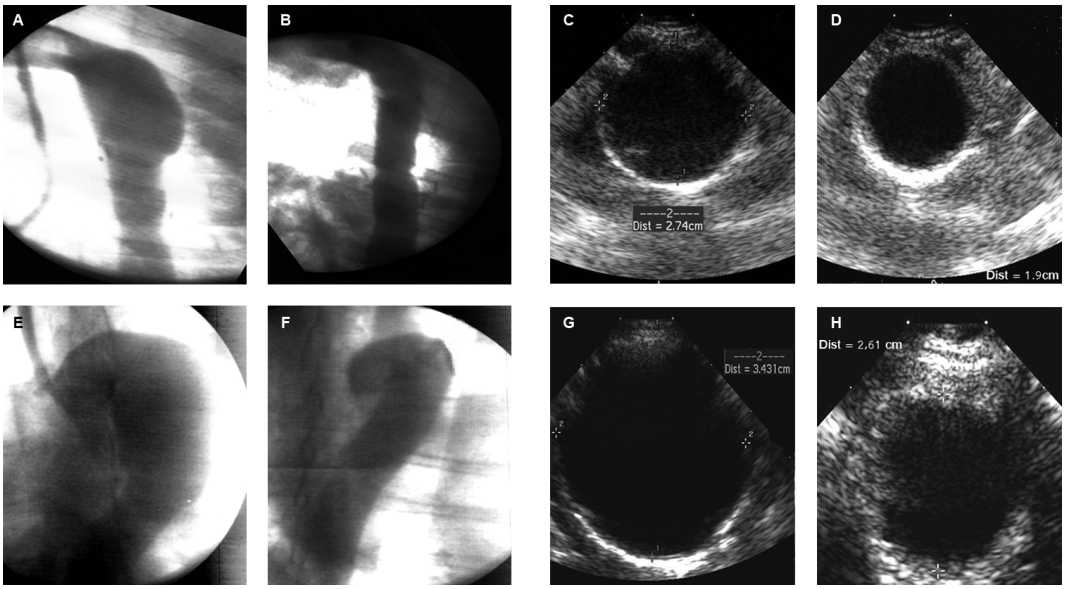

Figure 39: A,B,E,F) Angiographic images. A. Not reinforced PA at day 1; E. Not reinforced PA at day 180; B. Reinforced PA at day 1; F. Reinforced PA at day 180. Note the uniformity of the vessel profile in case of reinforcement (B,F) and loss of physiological shape, prone to aneurismal complication (A,E). C,D,G,H) Ecographic images (vessel cross sections). C. Not reinforced PA at day 1; G. Not reinforced PA at day 180; D. Reinforced PA at day 1; H. Reinforced PA at day 180. Note the severe diameter dilation in the not reinforced case (C,G).

actual PA arterialization.

It is worth to notice that the estimated Cauchy (actual) stresses, predicted by the mathematical model at 180 days and illustrated in Figure 41, bring to light further aspects that may help to better understand the actual effects of both PDS scaffold and e-PTFE armor in reinforced PA on growth and elastic response of the vessel to systemic pressure. In fact, from the stress profiles illustrated in Figure 41, it can be inferred (and somewhat quantified) the mechanical role of the prosthesis system and, in particular, of the GORE-TEX structure. The effective pressure difference between the internal systolic push and the external armor confinement *de facto* determines a "stress shielding" phenomenon which maintains the stress distribution over the PA thickness sufficiently uniform, by also forcing the stress level in the *tunica media* to be moderate with respect to the physiological one in

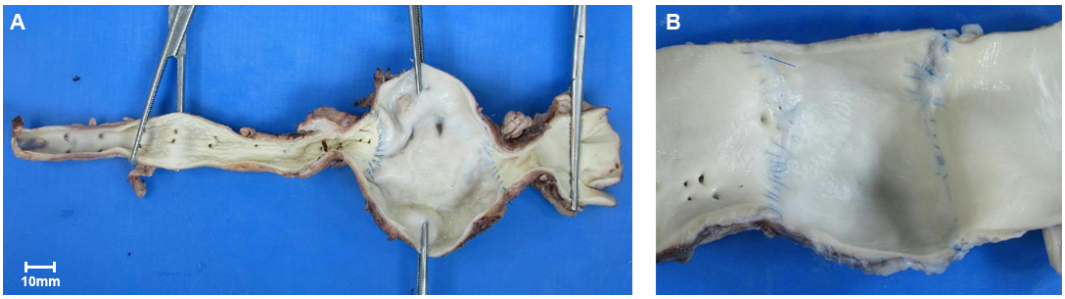

Figure 40: A. Not reinforced PA trunk with aneurismal formation (analysis after the break at 3 months); B. PA reinforced with knitted polydioxanone resorbable copolymer scaffold (explanted at 6 months): note the homogeneous vessel profile denoting the success of the implant.

the (ticker and stiffer) reference aorta, in this way creating a safe state of stress settling at about 100 kPa. On the contrary, from theoretical outcomes, the not reinforced PA exhibits equivalent (von Mises) and circumferential (hoop) stresses in the *tunica media* with peaks of about 800 kPa, a value sufficiently high and close to tissue stress threshold to determine mechanically critical states and invite yielding processes potentially undergoing aneurismal degeneration.

Also, Figure 41 shows the non-linear pressure-diameter curves one would virtually measure in the three cases examined (reference aorta, reinforced and not-reinforced PA) at 180 days, if an *ex vivo* inflation test were performed. It can be there noticed how the not reinforced PA experiences strong dilatation in a low range of inflation pressures –below 50 mmHg– with the external diameter achieving pathological dimensions before the curve exhibits a theoretical hardening. The behaviors of reference and reinforced pulmonary arteries are instead different, and, in both the cases, the diameters dilation at systemic pressure is in good agreement with the experimental observations in the animal model [85].

In particular, by comparing pressure-diameter curves for reinforced and not reinforced PA, it emerges from the results a significantly and qualitatively different mechanical response in the two cases, the former exhibiting much smaller variations of the outer diameter than the latter, within the same pressure interval, say in the order of tens kPa. In the reinforced PA, this initial stiff behavior can be attributed

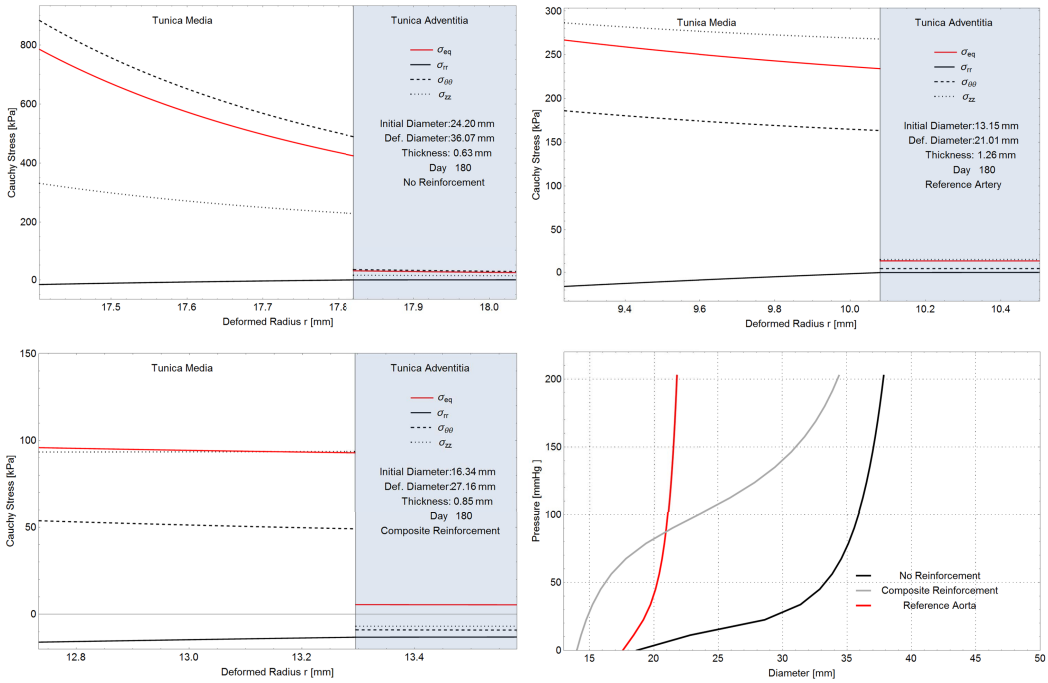

Figure 41: Cauchy stress profiles along the wall thicknesses in reference aorta (top-right), reinforced (bottom-left) and not reinforced (top-left) Pulmonary Autografts, with related pressure-diameter curves at 180 days for the grown vessels (bottom-right).

to the balancing between the internal push and the e-PTFE external pressure due to the GORE-TEX elastic reaction to the vessel expansion. After that, a region of approximately proportional dilatation is observed, followed by an elastic hardening at higher pressures due to the combined effect of the intrinsic hardening of the vessel walls related to stress levels and reorientation of elastic fibers and the increasing stiffness of the auxetic material induced by severely dilated armor elements.

It is finally worth to notice that, albeit the stiffer behavior of reinforced PA exhibited in Figure 41 in terms of pressure-diameter is theoretical derived at 180 days –thus in absence of PDS– the effect of the bioresorbable scaffold is implicitly taken into account by the model through the (at six months registered) PA arterializa-

tion, a result biomechanically due to the stress shielding, initially ensured by the biodegradable PDS and finally stabilized by the confining action of the GORE-TEX structure. The concrete consequence of this interplay can be explicitly traced in the proposed mathematical model by analyzing the results in terms of in-time remodeling of average wall bulk moduli k_0. In Figure 42 the comparison between reinforced and not reinforced PA intrinsic stiffness variation during the six-month is for this purpose shown.

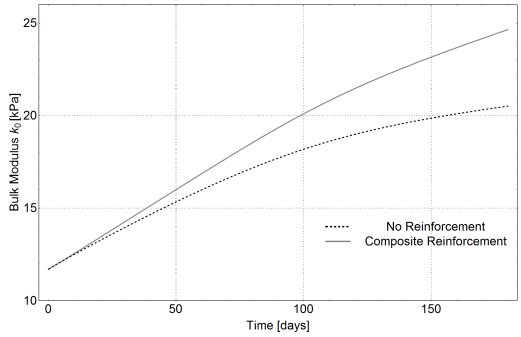

Figure 42: Evaluation of the bulk moduli remodeling in reinforced and not reinforced PA.

A.4 CONCLUSIONS

In the framework of Tissue Mechanics and by making reference to arterial walls where growth, remodeling, large deformations and stresses do interact through feedback mechanisms, an *ad hoc* mathematical model has been presented to support the *in vivo* results on animals subjected to the Ross operation, i.e. the use of autologous pulmonary artery to replace diseased aortic valve.
The theoretical outcomes, related to the modeling of the structural changes of reinforced pulmonary artery grafts under systemic pressure regimes, have shown that a virtuous biomechanical cooperation between biological and synthetic materials takes place, "stress-shielding" guiding the physiological arterialization of the vessel walls, consequently determining the overall success of the autograft

system. The modeling has in fact theoretically demonstrated that in doubly reinforced PA, the prosthesis system *de facto* works as a sort of "relay race", by guaranteeing the handover of the bearing structure functions from the PDS scaffold (at the early stages of tissue growth and remodeling) to the e-PTFE armor, initially "dormant" as a consequence of the typically low stiffness exhibited by stress-free auxetic structures at small strains. In this way, the mechanical shielding of the lapse vessel contains the radial expansion and simultaneously allows to the pulmonary artery to remodel its tunics for attaining an adequate level of mechanical properties. Once the bioresorbable scaffold has completed its degradation program and the strengthened vessel walls can actively respond to the systolic pressure, the e-PTFE structure accompanies PA *media* and *adventitia* toward their progressive aortic somatic growth, by stretching its weave to gain stiffness and to effectively confine further vessel expansion, so avoiding tissue prolapse and aneurismal degenerative phenomena. From the engineering point of view, all the results have essentially shown a very good agreement when compared with experimental data, also quantitatively, thus encouraging the use of the mathematical model for better understanding the specific biomechanical dynamics and designing possible new criteria and strategies for optimizing PA prostheses and successfully applying the surgical protocols to human patients.

Symbol	Unit	Value				References
		Aorta		PA		
		Media	Adventitia	Media	Adventitia	
Material Parameters						
k_0	[kPa]	51.1	5.1	16.7	1.67	[1, 2, 3]
k_1	[kPa]	18.6	1.86	4.9	0.49	[1, 2, 3]
k_2	[-]	17.4	1.74	0.839	0.711	[1, 4]
β	[deg]	29	62	29	62	[4]
Geometrical Parameters						
H	[mm]	0.8	0.4	0.667	0.333	E. O.
R_i	[mm]	7.8		9.5		E. O.
α	[deg]	91		120		[5]
λ^i_{zZ}	[-]	1.7		1		[4, E. O.]
λ^f_{zZ}	[-]	2		2		[6, E. O.]
PDS Parameters						
k^s_0	[kPa]	267				[7]
ν	[-]	1.34				[8]
ϕ_0	[-]	0.25				[9]
ω_1	[-]	0.07				F./A. P.
ω_2	[-]	0.05				F./A. P.
t_s	[day]	30				[10]
ePTFE Parameters						
k^n_1	[kPa]	1000				[7, 11, 12, 13, 14]
k^n_2	[-]	0.4				F./A. P.
H_n	[mm]	0.2				[15]
η_n	[deg]	26				F./A. P.
Growth-Remodeling data						
J^{max}_g	[-]	3.375				[16, 17, 18]
ζ	[-]	0.133				F./A. P.
c_g	[day^{-1}]	0.025				[19, 20]
c_γ	[kPa^{-1} day^{-1}]	8.64×10^{-5}				[21]
ω_z	[day^{-1}]	0.02				F./A. P.
t_z	[day]	90				F./A. P.

Table 11: Synoptic table of data and employed parameters
References: 1. [94] ; 2. [131] ; 3. [15] ; 4. [52] ; 5. [1] ; 6. [2] ; 7. [116] ; 8. [66] ; 9. [12] ; 10. [111] ; 11. [63] ; 12. [123] ; 13. [113] ; 14. [117] ; 15. [134] ; 16. [86] ; 17. [87] ; 18. [85] ; 19. [55] ; 20. [44] ; 21. [132]. E. O. - Experimentally Observed Parameters. F./A. P. - Fitting/Assumed Parameters

BIBLIOGRAPHY

[1] Victor Alastrué, Estefanía Peña, Miguel Ángel Martínez, and Manuel Doblaré. "Assessing the Use of the "Opening Angle Method" to Enforce Residual Stresses in Patient-Specific Arteries." In: *Annals of Biomedical Engineering* 35.10 (2007), pp. 1821–1837. DOI: 10.1007/s10439-007-9352-4.

[2] Victor Alastrué, Estefanía Peña, Miguel Ángel Martínez, and Manuel Doblaré. "Experimental study and constitutive modelling of the passive mechanical properties of the ovine infrarenal vena cava tissue." In: *Journal of Biomechanics* 41.14 (2008), pp. 3038 –3045. ISSN: 0021-9290. DOI: 10.1016/j.jbiomech.2008.07.008.

[3] D. Ambrosi and F. Guana. "Stress-Modulated Growth." In: *Mathematics and Mechanics of Solids* 12.3 (2005), pp. 319–342. DOI: 10.1177/1081286505059739.

[4] D Ambrosi et al. "Perspectives on biological growth and remodeling." In: *Journal of the Mechanics and Physics of Solids* 59.4 (2011), pp. 863–883. ISSN: 0022-5096. DOI: 10.1016/j.jmps.2010.12.011.

[5] L Andrusca, V Goanta, P D Barsanescu, and R Steigmann. "Numerical and experimental study of cruciform specimens subjected to biaxial tensile test." In: *IOP Conference Series: Materials Science and Engineering* 147 (2016), p. 012091. DOI: 10.1088/1757-899x/147/1/012091.

[6] Ellen M Arruda and Mary C Boyce. "A three-dimensional constitutive model for the large stretch behavior of rubber elastic materials." In: *Journal of the Mechanics and Physics of Solids* 41.2 (1993), pp. 389–412.

[7] E. E. Auer, K. W. Doak, and I. J. Schaffner. "Factors Affecting Laboratory Cut-Growth Resistance of Cold SBR Tread Stocks." In: *Rubber Chemistry and Technology* 31.1 (1958), pp. 185–201. DOI: 10.5254/1.3542257.

[8] P. Bažant and B. H. Oh. "Efficient Numerical Integration on the Surface of a Sphere." In: *ZAMM - Journal of Applied Mathematics and Mechanics / Zeitschrift für Angewandte Mathematik und Mechanik* 66.1 (1986), pp. 37–49. DOI: 10.1002/zamm.19860660108.

[9] J Bergstrom. "Constitutive modeling of the large strain time-dependent behavior of elastomers." In: *Journal of the Mechanics and Physics of Solids* 46.5 (1998), pp. 931–954. DOI: 10.1016/s0022-5096(97)00075-6.

[10] J. Blaber, B. Adair, and A. Antoniou. "Ncorr: Open-Source 2D Digital Image Correlation Matlab Software." In: *Experimental Mechanics* 55.6 (2015), pp. 1105–1122. DOI: 10.1007/s11340-015-0009-1.

[11] A. F. Blanchard and D. Parkinson. "Breakage of Carbon-Rubber Networks by Applied Stress." In: *Industrial & Engineering Chemistry* 44.4 (1952), pp. 799–812. DOI: 10.1021/ie50508a034.

[12] Eugene D Boland, Branch D Coleman, Catherine P Barnes, David G Simpson, Gary E Wnek, and Gary L Bowlin. "Electrospinning polydioxanone for biomedical applications." In: *Acta Biomaterialia* 1.1 (2005), pp. 115–123. ISSN: 1742-7061. DOI: 10.1016/j.actbio.2004.09.003.

[13] H. Bouasse and Z. Carrière. "Sur les courbes de traction du caoutchouc vulcanisé." In: *Annales de la faculté des sciences de Toulouse Mathématiques* 5.3 (1903), pp. 257–283. DOI: 10.5802/afst.205.

[14] F. Bueche. "Molecular basis for the mullins effect." In: *Journal of Applied Polymer Science* 4.10 (1960), pp. 107–114. DOI: 10.1002/app.1960.070041017.

[15] M.S. Cabrera, C.W.J. Oomens, C.V.C. Bouten, A.J.J.C. Bogers, S.P. Hoerstrup, and F.P.T. Baaijens. "Mechanical analysis of ovine and pediatric pulmonary artery for heart valve stent design." In: *Journal of Biomechanics* 46.12 (2013), pp. 2075 –2081. ISSN: 0021-9290. DOI: 10.1016/j.jbiomech.2013.04.020.

[16] M Centola, A Rainer, C Spadaccio, S De Porcellinis, J A Genovese, and M Trombetta. "Combining electrospinning and fused deposition modeling for the fabrication of a hybrid vascular graft." eng. In: *Biofabrication* 2.1 (Mar. 2010), p. 14102. ISSN: 1758-5090 (Electronic). DOI: 10.1088/1758-5082/2/1/014102.

[17] G.P. Cherepanov. "Crack propagation in continuous media." In: *Journal of Applied Mathematics and Mechanics* 31.3 (1967), pp. 503–512. DOI: 10.1016/0021-8928(67)90034-2.

[18] Luc Chevalier, Sylvain Calloch, François Hild, and Yann Marco. "Digital image correlation used to analyze the multiaxial behavior of rubber-like materials." In: *European Journal of Mechanics - A/Solids* 20.2 (2001), pp. 169–187. DOI: 10.1016/s0997-7538(00)01135-9.

[19] C. J. Chuong and Y. C. Fung. "Three-Dimensional Stress Distribution in Arteries." In: *Journal of Biomechanical Engineering* 105.3 (1983), p. 268. DOI: 10.1115/1.3138417.

[20] F. Clément, L. Bokobza, and L. Monnerie. "On the Mullins Effect in Silica-Filled Polydimethylsiloxane Networks." In: *Rubber Chemistry and Technology* 74.5 (2001), pp. 847–870. DOI: 10.5254/1.3547657.

[21] Bernard D. Coleman and Morton E. Gurtin. "Thermodynamics with Internal State Variables." In: *The Journal of Chemical Physics* 47.2 (1967), pp. 597–613. DOI: 10.1063/1.1711937.

[22] S C Cowin and S B Doty. *Tissue Mechanics*. Springer, 2007. ISBN: 9780387368252.

[23] E. M. Dannenberg and J. J. Brennan. "Strain Energy as a Criterion for Stress Softening in Carbon-Black-Filled Vulcanizates." In: *Rubber Chemistry and Technology* 39.3 (1966), pp. 597–608. DOI: 10.5254/1.3544867.

[24] Julie Diani, Bruno Fayolle, and Pierre Gilormini. "A review on the Mullins effect." In: *European Polymer Journal* 45.3 (2009), pp. 601–612. DOI: 10.1016/j.eurpolymj.2008.11.017.

[25] J.B. Donnet and E. Custodero. "Ordered structures observed by scanning tunnelling microscopy at atomic scale on carbon black surfaces." In: *Carbon* 30.5 (1992), pp. 813–815. DOI: 10.1016/0008-6223(92)90165-s.

[26] Jean-Baptiste Donnet. "Black and White Fillers and Tire Compound." In: *Rubber Chemistry and Technology* 71.3 (1998), pp. 323–341. DOI: 10.5254/1.3538488.

[27] A. Dorfmann and R.W. Ogden. "A constitutive model for the Mullins effect with permanent set in particle-reinforced rubber." In: *International Journal of Solids and Structures* 41.7 (2004), pp. 1855–1878. DOI: 10.1016/j.ijsolstr.2003.11.014.

[28] A. Einstein. "Berichtigung zu meiner Arbeit: „Eine neue Bestimmung der Moleküldimensionen"." In: *Annalen der Physik* 339.3 (1911), pp. 591–592. ISSN: 1521-3889. DOI: 10.1002/andp.19113390313.

[29] F. Ellyin, R. Vaziri, and L. Bigot. "Predictions of two nonlinear viscoelastic constitutive relations for polymers under multiaxial loadings." In: *Polymer Engineering & Science* 47.5 (2007), pp. 593–607. DOI: 10.1002/pen.20731.

[30] W. P. Fletcher and A. N. Gent. "Nonlinearity in the Dynamic Properties of Vulcanized Rubber Compounds." In: *Rubber Chemistry and Technology* 27.1 (1954), pp. 209–222. DOI: 10.5254/1.3543472.

[31] M. Fraldi, F. Carannante, and L. Nunziante. "Analytical solutions for n-phase functionally graded material cylinders under de saint venant load conditions: Homogenization and effects of poisson ratios on the overall stiffness." In: *Composites Part B: Engineering* 45.1 (2013), pp. 1310–1324. ISSN: 13598368. DOI: 10.1016/j.compositesb.2012.09.016.

[32] M. Fraldi and F. Guarracino. "An improved formulation for the assessment of the capacity load of circular rings and cylindrical shells under external pressure. Part 1. Analytical derivation." In: *Thin-Walled Structures* 49.9 (2011), pp. 1054 –1061. ISSN: 0263-8231. DOI: 10.1016/j.tws.2011.03.014.

[33] M. Fraldi, L. Nunziante, a. Gesualdo, and F. Guarracino. "On the bounding of limit multipliers for combined loading." In: *Proceedings of the Royal Society A: Mathematical, Physical and Engineering Sciences* 466.2114 (2010), pp. 493–514. ISSN: 1364-5021. DOI: 10.1098/rspa.2009.0240.

[34] Peter Fratzl and Richard Weinkamer. "Nature's hierarchical materials." In: *Progress in Materials Science* 52.8 (2007), pp. 1263–1334. ISSN: 0079-6425. DOI: 10.1016/j.pmatsci.2007.06.001.

[35] L. B. Freund. *Dynamic Fracture Mechanics*. Cambridge University Press, 1990. DOI: 10.1017/cbo9780511546761.

[36] M. Fujikawa, N. Maeda, J. Yamabe, Y. Kodama, and M. Koishi. "Determining Stress-Strain in Rubber with In-Plane Biaxial Tensile Tester." In: *Experimental Mechanics* 54.9 (2014), pp. 1639–1649. DOI: 10.1007/s11340-014-9942-7.

[37] Masaki Fujikawa, Takumu Kamimura, and Chobin Makabe. "Simple Calculation Technique of Nominal Stress / Strain in Biaxial Tensile Testing of Rubber Materials." In: *Journal of the Japanese Society for Experimental Mechanics* 10.1 (2010), pp. 104–109. DOI: 10.11395/jjsem.10.104.

[38] Yoshihide Fukahori. "New progress in the theory and model of carbon black reinforcement of elastomers." In: *Journal of Applied Polymer Science* 95.1 (2004), pp. 60–67. DOI: 10.1002/app.20802.

[39] Y Fung. *Biomechanics: mechanical properties of living tissues*. Biomechanics / Y. C. Fung. Springer-Verlag, 1981. ISBN: 9783540904724.

[40] A. N. Gent. "A New Constitutive Relation for Rubber." In: *Rubber Chemistry and Technology* 69.1 (1996), pp. 59–61. DOI: 10.5254/1.3538357.

[41] A. A. Griffith. "The Phenomena of Rupture and Flow in Solids." In: *Philosophical Transactions of the Royal Society A: Mathematical, Physical and Engineering Sciences* 221.582-593 (1921), pp. 163–198. DOI: 10.1098/rsta.1921.0006.

[42] Eugene Guth. "Theory of Filler Reinforcement." In: *Journal of Applied Physics* 16.1 (1945), pp. 20–25. DOI: 10.1063/1.1707495.

[43] Serdar Göktepe and Christian Miehe. "A micro-macro approach to rubber-like materials. Part III: The micro-sphere model of anisotropic Mullins-type damage." In: *Journal of the Mechanics and Physics of Solids* 53.10 (2005), pp. 2259–2283. DOI: 10.1016/j.jmps.2005.04.010.

[44] Mohamed Ben Hamouda and Naziha Atti. "Comparison of growth curves of lamb fat tail measurements and their relationship with body weight in Babarine sheep." In: *Small Ruminant Research* 95.2-3 (2011), pp. 120–127. DOI: 10.1016/j.smallrumres.2010.10.001.

[45] J. A. C. Harwood and A. R. Payne. "Stress Softening in Natural Rubber Vulcanizates. IV. Unfilled Vulcanizates." In: *Rubber Chemistry and Technology* 40.3 (1967), pp. 840–848. DOI: 10.5254/1.3539099.

[46] G. Heinrich and M. Kaliske. "Theoretical and numerical formulation of a molecular based constitutive tube-model of rubber elasticity." In: *Computational and Theoretical Polymer Science* 7.3-4 (1997), pp. 227–241. DOI: 10.1016/s1089-3156(98)00010-5.

[47] R. Hill. "On constitutive inequalities for simple materials - I." In: *Journal of the Mechanics and Physics of Solids* 16.4 (1968), pp. 229–242. DOI: 10.1016/0022-5096(68)90031-8.

[48] G A Holzapfel and R W Ogden. *Mechanics of Biological Tissue*. Springer, 2006. ISBN: 9783540251941.

[49] G. A. Holzapfel and R. W. Ogden. "Constitutive modelling of arteries." In: *Proceedings of the Royal Society A: Mathematical, Physical and Engineering Sciences* 466.2118 (2010), pp. 1551–1597. DOI: 10.1098/rspa.2010.0058.

[50] Gerhard A. Holzapfel. *Nonlinear Solid Mechanics: A Continuum Approach for Engineering*. Wiley, 2000. ISBN: 978-0471823198.

[51] Gerhard A Holzapfel. "Similarities between soft biological tissues and rubberlike materials." In: *Constitutive models for rubber*. Vol. 4. Balkema. 2005, p. 607.

[52] Gerhard A. Holzapfel, Thomas C. Gasser, and Raymond W. Ogden. "A New Constitutive Framework for Arterial Wall Mechanics and a Comparative Study of Material Models." English. In: *Journal of elasticity and the physical science of solids* 61.1-3 (2000), pp. 1–48. ISSN: 0374-3535. DOI: 10.1023/A:1010835316564.

[53] R. Houwink. "Slipping of Molecules during the Deformation of Reinforced Rubber." In: *Rubber Chemistry and Technology* 29.3 (1956), pp. 888–893. DOI: 10.5254/1.3542602.

[54] J.-J. Hu, G.-W. Chen, Y.-C. Liu, and S.-S. Hsu. "Influence of Specimen Geometry on the Estimation of the Planar Biaxial Mechanical Properties of Cruciform Specimens." In: *Experimental Mechanics* 54.4 (2013), pp. 615–631. DOI: 10.1007/s11340-013-9826-2.

[55] J D Humphrey. *Cardiovascular Solid Mechanics*. Springer-Verlag New York, 2002. DOI: 10.1007/978-0-387-21576-1.

[56] Jürgen Hörer et al. "Neoaortic Root Diameters and Aortic Regurgitation in Children After the Ross Operation." In: *The Annals of Thoracic Surgery* 88.2 (2009), pp. 594–600. DOI: 10.1016/j.athoracsur.2009.04.077.

[57] George R Irwin. "Analysis of stresses and strains near the end of a crack traversing a plate." In: *Spie Milestone series MS* 137.167-170 (1997), p. 16.

[58] Jeffrey G Jacot, Ibrahim Abdullah, Michael Belkin, Marie Gerhard-Herman, Peter Gaccione, Joseph F Polak, Magruder C Donaldson, Anthony D Whittemore, and Michael S Conte. "Early adaptation of human lower extremity vein grafts: wall stiffness changes accompany geometric remodeling." eng. In: *Journal of vascular surgery* 39.3 (Mar. 2004), pp. 547–555. ISSN: 0741-5214 (Print). DOI: 10.1016/j.jvs.2003.09.045.

[59] A. G. James, A. Green, and G. M. Simpson. "Strain energy functions of rubber. I. Characterization of gum vulcanizates." In: *Journal of Applied Polymer Science* 19.7 (1975), pp. 2033–2058. DOI: 10.1002/app.1975.070190723.

[60] M. Kaliske and G. Heinrich. "An Extended Tube-Model for Rubber Elasticity: Statistical-Mechanical Theory and Finite Element Implementation." In: *Rubber Chemistry and Technology* 72.4 (1999), pp. 602–632. DOI: 10.5254/1.3538822.

[61] Arseniy Karkach. "Trajectories and models of individual growth." In: *Demographic Research* 15 (2006), pp. 347–400. DOI: 10.4054/demres.2006.15.12.

[62] S. Kawabata, M. Matsuda, K. Tei, and H. Kawai. "Experimental survey of the strain energy density function of isoprene rubber vulcanizate." In: *Macromolecules* 14.1 (1981), pp. 154–162. DOI: 10.1021/ma50002a032.

[63] Sang-Hoon Kim, ChoHay Mun, Youngmee Jung, Sang-Heon Kim, Dong-Ik Kim, and SooHyun Kim. "Mechanical properties of compliant double layered poly(L-lactide-co-ϵ-caprolactone) vascular graft." English. In: *Macromolecular Research* 21.8 (2013), pp. 886–891. ISSN: 1598-5032. DOI: 10.1007/s13233-013-1095-5.

[64] Manfred Klüppel and Joachim Schramm. "A generalized tube model of rubber elasticity and stress softening of filler reinforced elastomer systems." In: *Macromolecular Theory and Simulations* 9.9 (2000), pp. 742–754. ISSN: 1521-3919. DOI: 10.1002/1521-3919(20001201)9:9<742::AID-MATS742>3.0.CO;2-4.

[65] Yuuki Kondo, Kenji Urayama, Masatoshi Kidowaki, Koichi Mayumi, Toshikazu Takigawa, and Kohzo Ito. "Applicability of a particularly simple model to nonlinear elasticity of slide-ring gels with movable cross-links as revealed by unequal biaxial deformation." In: *The Journal of Chemical Physics* 141.13 (2014), p. 134906. DOI: 10.1063/1.4897134.

[66] J. Kováčik. "Correlation between Young's modulus and porosity in porous materials." English. In: *Journal of Materials Science Letters* 18.13 (1999), pp. 1007–1010. ISSN: 0261-8028. DOI: 10.1023/A:1006669914946.

[67] G. Kraus, C. W. Childers, and K. W. Rollmann. "Stress softening in carbon black-reinforced vulcanizates. Strain rate and temperature effects." In: *Journal of Applied Polymer Science* 10.2 (1966), pp. 229–244. DOI: 10.1002/app.1966.070100205.

[68] G. J. Lake and P. B. Lindley. "Cut growth and fatigue of rubbers. II. Experiments on a noncrystallizing rubber." In: *Journal of Applied Polymer Science* 8.2 (1964), pp. 707–721. DOI: 10.1002/app.1964.070080212.

[69] G. J. Lake and O. H. Yeoh. "Effect of crack tip sharpness on the strength of vulcanized rubbers." In: *Journal of Polymer Science Part B: Polymer Physics* 25.6 (1987), pp. 1157–1190. DOI: 10.1002/polb.1987.090250601.

[70] K. A. Lazopoulos and R. W. Ogden. "Nonlinear Elasticity Theory with Discontinuous Internal Variables." In: *Mathematics and Mechanics of Solids* 3.1 (1998), pp. 29–51. DOI: 10.1177/108128659800300103.

[71] Jean L. Leblanc. "Rubber-filler interactions and rheological properties in filled compounds." In: *Progress in Polymer Science* 27.4 (2002), pp. 627 –687. ISSN: 0079-6700. DOI: 10.1016/S0079-6700(01)00040-5.

[72] Alexander Lion. "A constitutive model for carbon black filled rubber: Experimental investigations and mathematical representation." In: *Continuum Mechanics and Thermodynamics* 8.3 (1996), pp. 153–169. DOI: 10.1007/bf01181853.

[73] H. Lorenz, M. Klüppel, and G. Heinrich. "Microstructure-based modelling and FE implementation of filler-induced stress softening and hysteresis of reinforced rubbers." In: *ZAMM - Journal of Applied Mathematics and Mechanics / Zeitschrift für Angewandte Mathematik und Mechanik* 92.8 (2012), pp. 608–631. DOI: 10.1002/zamm.201100172.

[74] H. Lu and P. D. Cary. "Deformation measurements by digital image correlation: Implementation of a second-order displacement gradient." In: *Experimental Mechanics* 40.4 (2000), pp. 393–400. DOI: 10.1007/bf02326485.

[75] Shuyang Lu, Peng Zhang, Xiaoning Sun, Feirong Gong, Shouguo Yang, Li Shen, Zheyong Huang, and Chunsheng Wang. "Synthetic ePTFE Grafts Coated with an Anti-CD133 Antibody-Functionalized Heparin/Collagen Multilayer with Rapid in vivo Endothelialization Properties." In: *ACS Applied Materials & Interfaces* 5.15 (2013), pp. 7360–7369. DOI: 10.1021/am401706w.

[76] V A Lubarda and A Hoger. "On the mechanics of solids with a growing mass." In: *International Journal of Solids and Structures* 39.18 (2002), pp. 4627–4664. ISSN: 0020-7683. DOI: 10.1016/S0020-7683(02)00352-9.

[77] G. Marckmann and E. Verron. "Comparison of Hyperelastic Models for Rubber-Like Materials." In: *Rubber Chemistry and Technology* 79.5 (2006), pp. 835–858. DOI: 10.5254/1.3547969.

[78] W. V. Mars and A. Fatemi. "Factors that Affect the Fatigue Life of Rubber: A Literature Survey." In: *Rubber Chemistry and Technology* 77.3 (2004), pp. 391–412. DOI: 10.5254/1.3547831.

[79] W. V. Mars and A. Fatemi. "Multiaxial fatigue of rubber: Part II: experimental observations and life predictions." In: *Fatigue and Fracture of Engineering Materials and Structures* 28.6 (2005), pp. 523–538. DOI: 10.1111/j.1460-2695.2005.00895.x.

[80] W Mars, M Isasi, and A Arriaga. "Loss of stiffness during fatigue and the development of crack precursors." In: *Constitutive Models for Rubber VIII*. Informa UK Limited, 2013, pp. 355–360. DOI: 10.1201/b14964-64.

[81] G. Molea, F. Schonauer, G. Bifulco, and D. D'Angelo. "Comparative study on biocompatibility and absorption times of three absorbable monofilament suture materials (Polydioxanone, Poliglecaprone 25, Glycomer 631)." In: *British Journal of Plastic Surgery* 53.2 (2000), pp. 137–141. DOI: 10.1054/bjps.1999.3247.

[82] M. Mooney. "A Theory of Large Elastic Deformation." In: *Journal of Applied Physics* 11.9 (1940), pp. 582–592. DOI: 10.1063/1.1712836.

[83] L. Mullins. "Effect of Stretching on the Properties of Rubber." In: *Rubber Chemistry and Technology* 21.2 (1948), pp. 281–300. DOI: 10.5254/1.3546914.

[84] L. Mullins. "Softening of Rubber by Deformation." In: *Rubber Chemistry and Technology* 42.1 (1969), pp. 339–362. DOI: 10.5254/1.3539210.

[85] Francesco Nappi, Cristiano Spadaccio, Clotilde Castaldo, Franca Di Meglio, Daria Nurzynska, Stefania Montagnani, Massimo Chello, and Christophe Acar. "Reinforcement of the pulmonary artery autograft with a polyglactin and polydioxanone mesh in the Ross operation: experimental study in growing lamb." In: *J Heart Valve Dis* 23.2 (2014), pp. 145–8.

[86] Francesco Nappi, Cristiano Spadaccio, Pierre Fouret, Nadjib Hammoudi, Juan Carlos Chachques, Massimo Chello, and Christophe Acar. "An experimental model of the Ross operation: Development of resorbable reinforcements for pulmonary autografts." In: *The Journal of Thoracic and Cardiovascular Surgery* 149.4 (July 2015), pp. 1134–1142. DOI: 10.1016/j.jtcvs.2014.12.056.

[87] Francesco Nappi, Cristiano Spadaccio, Massimo Chello, and Christophe Acar. "The Ross procedure: Underuse or under-comprehension?" In: *The Journal of Thoracic and Cardiovascular Surgery* 149.5 (July 2015), pp. 1463–1464. DOI: 10.1016/j.jtcvs.2015.01.021.

[88] Francesco Nappi, Cristiano Spadaccio, Nawwar Al-Attar, and Christophe Acar. "The Ross procedure at the crossroads: Lessons from biology." In: *International Journal of Cardiology* 178 (2015), pp. 37–39. DOI: 10.1016/j.ijcard.2014.10.134.

[89] Juha-Pekka Nuutinen, Claude Clerc, Raija Reinikainen, and Pertti Törmälä. "Mechanical properties and in vitro degradation of bioabsorbable self-expanding braided stents." In: *Journal of Biomaterials Science, Polymer Edition* 14.3 (2003), pp. 255–266. DOI: 10.1163/156856203763572707.

[90] R. W. Ogden. "Large Deformation Isotropic Elasticity - On the Correlation of Theory and Experiment for Incompressible Rubberlike Solids." In: *Rubber Chemistry and Technology* 46.2 (1973), pp. 398–416. DOI: 10.5254/1.3542910.

[91] R. W. Ogden. *Non-Linear Elastic Deformations (Dover Civil and Mechanical Engineering)*. Dover Publications, 2013. ISBN: 978-0486696485.

[92] R. W. Ogden and D. G. Roxburgh. "A pseudo-elastic model for the Mullins effect in filled rubber." In: *Proceedings of the Royal Society A: Mathematical, Physical and Engineering Sciences* 455.1988 (1999), pp. 2861–2877. DOI: 10.1098/rspa.1999.0431.

[93] R. W. Ogden, G. Saccomandi, and I. Sgura. "Fitting hyperelastic models to experimental data." In: *Computational Mechanics* 34.6 (2004), pp. 484–502. DOI: 10.1007/s00466-004-0593-y.

[94] Tobias Olsson and Anders Klarbring. "Residual stresses in soft tissue as a consequence of growth and remodeling: application to an arterial geometry." In: *European Journal of Mechanics - A/Solids* 27.6 (2008), pp. 959–974. ISSN: 0997-7538. DOI: 10.1016/j.euromechsol.2007.12.006.

[95] Lindley P.B. "Energy for crack growth in model rubber components." In: *The Journal of Strain Analysis for Engineering Design* 7.2 (1972), pp. 132–140. DOI: 10.1243/03093247v072132.

[96] A. R. Payne. "The Dynamic Properties of Carbon Black-Loaded Natural Rubber Vulcanizates. Part I." In: *Rubber Chemistry and Technology* 36.2 (1963), pp. 432–443. DOI: 10.5254/1.3539570.

[97] A. R. Payne and R. E. Whittaker. "Low Strain Dynamic Properties of Filled Rubbers." In: *Rubber Chemistry and Technology* 44.2 (1971), pp. 440–478. DOI: 10.5254/1.3547375.

[98] J. L. Poisson, S. Méo, F. Lacroix, G. Berton, and N. Ranganathan. "Multiaxial fatigue criteria applied to polychloroprene rubber." In: *Rubber Chemistry and Technology* 85.1 (2012), pp. 80–91. DOI: 10.5254/1.3672431.

[99] Ogden R.W. and Fu Y.B. *Nonlinear Elasticity: Theory and Applications (London Mathematical Society Lecture Note Series)*. Cambridge University Press, 2001.

[100] M. Rachik, F. Schmidtt, N. Reuge, Y. Le Maoult, and F. Abbeé. "Elastomer biaxial characterization using bubble inflation technique. II: Numerical investigation of some constitutive models." In: *Polymer Engineering & Science* 41.3 (2001), pp. 532–541. DOI: 10.1002/pen.10750.

[101] M. Rebouah and G. Chagnon. "Extension of classical viscoelastic models in large deformation to anisotropy and stress softening." In: *International Journal of Non-Linear Mechanics* 61 (2014), pp. 54–64. DOI: 10.1016/j.ijnonlinmec.2014.01.009.

[102] M Rebouah, G Chagnon, and D Favier. "Anisotropic modeling of the Mullins effect and the residual strain of filled silicone rubber." In: *Constitutive Models for Rubber VIII*. Informa UK Limited, 2013, pp. 431–435. DOI: 10.1201/b14964-78.

[103] Mikael C Rechtsman, Frank H Stillinger, and Salvatore Torquato. "Negative Poisson's Ratio Materials via Isotropic Interactions." In: *Phys. Rev. Lett.* 101.8 (2008), p. 85501. DOI: 10.1103/PhysRevLett.101.085501.

[104] Jiu-Sheng Ren. "Growth and residual stresses of arterial walls." In: *Journal of Theoretical Biology* 337 (2013), pp. 80–88. DOI: 10.1016/j.jtbi.2013.08.008.

[105] N. Reuge, F. M. Schmidt, Y. Le Maoult, M. Rachik, and F. Abbé. "Elastomer biaxial characterization using bubble inflation technique. I: Experimental investigations." In: *Polymer Engineering & Science* 41.3 (2001), pp. 522–531. DOI: 10.1002/pen.10749.

[106] J. R. Rice. "A Path Independent Integral and the Approximate Analysis of Strain Concentration by Notches and Cracks." In: *Journal of Applied Mechanics* 35.2 (1968), p. 379. DOI: 10.1115/1.3601206.

[107] R. S. Rivlin. "Large Elastic Deformations of Isotropic Materials. I. Fundamental Concepts." In: *Philosophical Transactions of the Royal Society of London A: Mathematical, Physical and Engineering Sciences* 240.822 (1948), pp. 459–490. ISSN: 0080-4614. DOI: 10.1098/rsta.1948.0002. eprint: http://rsta.royalsocietypublishing.org/content/240/822/459.full.pdf.

[108] R. S. Rivlin. "Large Elastic Deformations of Isotropic Materials. IV. Further Developments of the General Theory." In: *Philosophical Transactions of the Royal Society of London A: Mathematical, Physical and Engineering Sciences* 241.835 (1948), pp. 379–397. ISSN: 0080-4614. DOI: 10.1098/rsta.1948.0024. eprint: http://rsta.royalsocietypublishing.org/content/241/835/379.full.pdf.

[109] R. S. Rivlin and A. G. Thomas. "Rupture of rubber. I. Characteristic energy for tearing." In: *Journal of Polymer Science* 10.3 (1953), pp. 291–318. DOI: 10.1002/pol.1953.120100303.

[110] Edward K Rodriguez, Anne Hoger, and Andrew D McCulloch. "Stress-dependent finite growth in soft elastic tissues." In: *Journal of Biomechanics* 27.4 (1994), pp. 455–467. ISSN: 0021-9290. DOI: 10.1016/0021-9290(94)90021-3.

[111] Marcos A Sabino, Susana González, Leni Márquez, and José L Feijoo. "Study of the hydrolytic degradation of polydioxanone PPDX." In: *Polymer Degradation and Stability* 69.2 (2000), pp. 209–216. ISSN: 0141-3910. DOI: 10.1016/S0141-3910(00)00062-8.

[112] Guiseppe Saccomandi and Ray W. Ogden, eds. *Mechanics and Thermomechanics of Rubberlike Solids*. Springer, 2014.

[113] Henryk J. Salacinski, Sean Goldner, Alberto Giudiceandrea, George Hamilton, Alexander M. Seifalian, Alan Edwards, and Robert J. Carson. "The Mechanical Behavior of Vascular Grafts: A Review." In: *Journal of Biomaterials Applications* 15.3 (2001), pp. 241–278. DOI: 10.1106/NA5T-J57A-JTDD-FD04. eprint: http://jba.sagepub.com/content/15/3/241.full.pdf+html.

[114] M. Sasso, G. Palmieri, G. Chiappini, and D. Amodio. "Characterization of hyperelastic rubber-like materials by biaxial and uniaxial stretching tests based on optical methods." In: *Polymer Testing* 27.8 (2008), pp. 995–1004. DOI: 10.1016/j.polymertesting.2008.09.001.

[115] M. Sasso, G. Chiappini, M. Rossi, L. Cortese, and E. Mancini. "Visco-Hyper-Pseudo-Elastic Characterization of a Fluoro-Silicone Rubber." In: *Experimental Mechanics* 54.3 (2013), pp. 315–328. DOI: 10.1007/s11340-013-9807-5.

[116] S.A. Sell, M.J. McClure, D.C. Knapp, B.H. Walpoth, D. G. Simpson, and G. L. Bowlin. "Electrospun polydioxanone-elastin blends: potential for bioresorbable vascular grafts." In: *Biomed Mater* 1 (2006), pp. 72–80. DOI: 10.1088/1748-6041/1/2/004.

[117] Hiromichi Sonoda, Shin-Ichi Urayama, Keiichi Takamizawa, Yasuhide Nakayama, Chikao Uyama, Hisataka Yasui, and Takehisa Matsuda. "Compliant design of artificial graft: Compliance determination by new digital X-ray imaging system-based method." In: *Journal of Biomedical Materials Research* 60.1 (2002), pp. 191–195. ISSN: 1097-4636. DOI: 10.1002/jbm.10055.

[118] Cristiano Spadaccio, Massimo Chello, Marcella Trombetta, Alberto Rainer, Yoshiya Toyoda, and Jorge A Genovese. "Drug releasing systems in cardiovascular tissue engineering." eng. In: *Journal of cellular and molecular medicine* 13.3 (Mar. 2009), pp. 422–439. ISSN: 1582-4934 (Electronic). DOI: 10.1111/j.1582-4934.2008.00532.x.

[119] Cristiano Spadaccio, Alberto Rainer, Matteo Centola, Marcella Trombetta, Massimo Chello, Mario Lusini, Elvio Covino, Yoshiya Toyoda, and Jorge A Genovese. "Heparin-releasing scaffold for stem cells: a differentiating device for vascular aims." eng. In: *Regenerative medicine* 5.4 (July 2010), pp. 645–657. ISSN: 1746-076X (Electronic). DOI: 10.2217/rme.10.25.

[120] Cristiano Spadaccio, Alberto Rainer, Raffaele Barbato, Massimo Chello, and Bart Meyns. "The fate of large-diameter Dacron® vascular grafts in surgical practice: Are we really satisfied?" In: *International Journal of Cardiology* 168.5 (2013), pp. 5028–5029. DOI: 10.1016/j.ijcard.2013.07.165.

[121] Cristiano Spadaccio, Stefania Montagnani, Christophe Acar, and Francesco Nappi. "Introducing bioresorbable scaffolds into the show. A potential adjunct to resuscitate Ross procedure." In: *International Journal of Cardiology* 190 (July 2015), pp. 50–52. DOI: 10.1016/j.ijcard.2015.04.098.

[122] Paul Steinmann, Mokarram Hossain, and Gunnar Possart. "Hyperelastic models for rubber-like materials: consistent tangent operators and suitability for Treloar's data." In: *Archive of Applied Mechanics* 82.9 (2012), pp. 1183–1217. DOI: 10.1007/s00419-012-0610-z.

[123] N. R. Tai, H. J. Salacinski, A. Edwards, G. Hamilton, and A.M. Seifalian. "Compliance properties of conduits used in vascular reconstruction." In: *British Journal of Surgery* 87.11 (2000), pp. 1516–1524. ISSN: 1365-2168. DOI: 10.1046/j.1365-2168.2000.01566.x.

[124] A. G. Thomas. "Rupture of rubber. V. Cut growth in natural rubber vulcanizates." In: *Journal of Polymer Science* 31.123 (1958), pp. 467–480. DOI: 10.1002/pol.1958.1203112324.

[125] L. R. G. Treloar. "The elasticity of a network of long-chain molecules. I." In: *Transactions of the Faraday Society* 39 (1943), p. 36. DOI: 10.1039/tf9433900036.

[126] L. R. G. Treloar. "Stress-strain data for vulcanised rubber under various types of deformation." In: *Transactions of the Faraday Society* 40 (1944), p. 59. DOI: 10.1039/tf9444000059.

[127] L. R. G. Treloar. *The Physics of Rubber Elasticity*. Oxford University Press, Dec. 11, 2005. 310 pp. ISBN: 0198570279.

[128] A. M. Turing. "The Chemical Basis of Morphogenesis." In: *Philosophical Transactions of the Royal Society of London B: Biological Sciences* 237.641 (1952), pp. 37–72. ISSN: 0080-4622. DOI: 10.1098/rstb.1952.0012.

[129] Mars W. V. and Fatemi A. "Multiaxial fatigue of rubber: Part I: equivalence criteria and theoretical aspects." In: *Fatigue and Fracture of Engineering Materials and Structures* 28.6 (2005), pp. 515–522. DOI: 10.1111/j.1460-2695.2005.00891.x.

[130] R. Vandiver and A. Goriely. "Differential growth and residual stress in cylindrical elastic structures." In: *Philosophical Transactions of the Royal Society A: Mathematical, Physical and Engineering Sciences* 367.1902 (2009), pp. 3607–3630. DOI: 10.1098/rsta.2009.0114.

[131] J. Veselý, L. Horný, H. Chlup, T. Adámek, M. Krajíček, and R. Žitný. "Constitutive modeling of human saphenous veins at overloading pressures." In: *Journal of the Mechanical Behavior of Biomedical Materials* 45 (2015), pp. 101 –108. ISSN: 1751-6161. DOI: 10.1016/j.jmbbm.2015.01.023.

[132] Shijia Zhao and Linxia Gu. "Implementation and validation of aortic remodeling in hypertensive rats." eng. In: *Journal of biomechanical engineering* 136.9 (Sept. 2014), p. 91007. ISSN: 1528-8951 (Electronic). DOI: 10.1115/1.4027939.

[133] X. Zhao, Z. C. Berwick, J. F. Krieger, H. Chen, S. Chambers, and G. S. Kassab. "Novel Design of Cruciform Specimens for Planar Biaxial Testing of Soft Materials." In: *Experimental Mechanics* 54.3 (2013), pp. 343–356. DOI: 10.1007/s11340-013-9808-4.

[134] Meital Zilberman and Robert C. Eberhart. "Drug-eluting bioresorbable stents for various applications." In: *Annual Review of Biomedical Engineering* 8.1 (2006), pp. 153–180. DOI: 10.1146/annurev.bioeng.8.013106.151418.